The evolution of oceanic nonlinear internal waves over variable topography

by

Chunxin Yuan

A thesis submitted in conformity with the requirements for the degree of Doctor of Philosophy

Department of Mathematics

Faculty of Mathematical & Physical Sciences

University College London

April, 2018

Disclaimer

I, Chunxin Yuan, confirm that the work presented in this thesis is my own. Where information has been derived from other sources, I confirm that this has been indicated in the thesis.

Signature _____

Date _____

This thesis was completed under the supervision of Professor Roger Grimshaw and Professor Edward Johnson.

Publications:

1. R. Grimshaw and **C. Yuan.** The propagation of internal undular bores over variable topography. *Physica D: Nonlinear Phenomena,* 333:200-207, 2016.
2. R. Grimshaw and **C. Yuan.** Depression and elevation tsunami waves in the framework of the Korteweg-de Vries equation. *Natural Hazards,* 84:493-511, 2016.
3. **Chunxin Yuan**, Roger Grimshaw, Edward Johnson, and Xueen Chen. The propagation of internal solitary waves over variable topography in a horizontally two-dimensional framework. *Journal of Physical Oceanography,* 48:283-300, 2018.
4. **C. Yuan**, R. Grimshaw, and E. Johnson. The evolution of second mode internal solitary waves over variable topography. *Journal of Fluid Mechanics*, 836:238-259, 2018.
5. **Chunxin Yuan**, Roger Grimshaw, and Edward Johnson. The evolution of internal undular bores over a slope in the presence of rotation. *Studies in Applied Mathematics* (Publish Online), 2018.
6. **C. Yuan**, R. Grimshaw, E. Johnson, and Z. Wang. Topographic effect on oblique internal wave-wave interactions. *Journal of Fluid Mechanics (Under review)*, 2018.
7. Roger Grimshaw, and **Chunxin Yuan**. Internal undular bores in the coastal ocean. In *The Ocean in Motion*, pp. 23-39. Springer, Cham, 2018.

Abstract

This thesis is concerned with the evolution of oceanic nonlinear internal waves over variable one-dimensional and two-dimensional topography. The methodology is based on a variable-coefficient Korteweg-de Vries (vKdV) equation and its variants, including the Ostrovsky equation which takes rotation into account and a Kadomtsev-Petviashvili (KP) equation which extends these one-dimensional models to two space dimensions. In addition, a fully nonlinear and non-hydrostatic three-dimensional primitive equation model, MIT general circulation model (MITgcm), is invoked to provide supplementary analyses. First, the long-time combined effect of rotation and variable topography on the evolution of internal undular bore is studied; then an initial mode-2 internal solitary wave propagating onto the continental shelf-slope in a three-layer fluid is investigated. After that, the research is extended to two-dimensional space in which submarine canyon and plateau topography are implemented to examine a mode-1 internal solitary wave propagating over these topographic features. Finally, the topographic effect on internal wave-wave interactions is examined using an initial 'V-shape' wave representing two interacting waves in the framework of the KP equation.

Impact Statement

The present investigation on oceanic nonlinear internal waves over variable topography has both economic and academic value. Internal waves can pose potential hazards on offshore drilling platform and cause loss of money, which indicates that a prediction system for the intensity and arrival time of internal waves around the platform will be beneficial. In addition, the induced mixing by the breaking of internal waves in the coast can boost biological productivity, hence the knowledge of wave propagations will guide us to determine those areas. Nowadays, global climate change has been drawing much attention, and recent research has demonstrated that internal waves are important in redistributing heat and momentum in the ocean.

Acknowledgements

I am grateful to my two supervisors, Professor Roger Grimshaw and Professor Edward Johnson. They impressed me greatly with their superb knowledge and persistent enthusiasm in research, which I consider an invaluable treasure for my academic career.

I thank Prof. Xueen Chen, who guided me when I was at Ocean University of China. He was very kind and generous to me and it was his encouragement and help that made me settled my mind to pursue my PhD.

I would like to thank all my friends, colleagues and the supporting staff at the Department of Mathematics, UCL.

I am most indebted to my parents. Their infinite support and deep love are the biggest motivations of my life.

My PhD project is funded by the China Scholarship Council (CSC) and UCL Dean's Prize. Their sponsorship is greatly acknowledged.

Chunxin Yuan, *University College London*, July 2018

Contents

List of Tables

List of Figures

Chapter 1

Introduction

1.1 Oceanic internal waves

Interest in the internal waves commonly observed in the coastal oceans, straits and fjords has been particularly strong during the last several decades owing to their important role on the marine ecosystem, marine geology and on coastal engineering. These internal waves occur in the interior of the ocean, but have a surface signature, manifested as a small modulation on the surface roughness, which can be recorded by satellite images. The restoring force of internal waves is buoyancy, measured by the buoyancy frequency N, where N^2 is a measure of the vertical gradient of the background density. It is much weaker (usually of order $\mathcal{O}(10^{-2} - 10^{-3})$) than gravity exerted on the same water parcel, which implies that even induced by a small disturbance, internal waves can have large amplitudes and strong currents. This can be explained dynamically when considering a simple model. Assuming a perturbation is acted on a fluid parcel, which amounts to an amount of kinetic energy is input to the system, then when the density gradient is small, this parcel has to move a large distance to convert that kinetic energy to potential energy. One of the strongest internal solitary waves on record has an amplitude of 240 m, and a peak current velocity of 2.55 m/s, captured at a mooring site deployed in the northern

South China Sea at the bottom depth of 3847 m, see Huang et al. [55]. The scale of these waves implies that they can pose potential hazards for underwater drilling, see Osborne et al. [86].

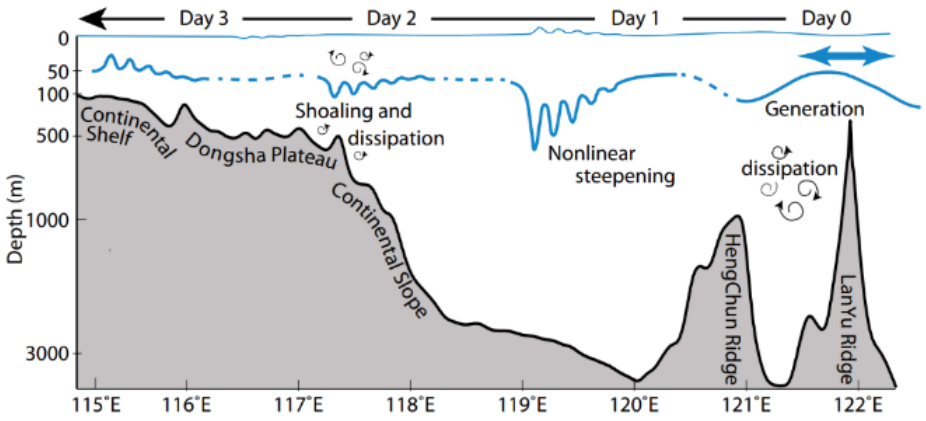

Figure 1.1: Schematic illustrating a three-day life cycle of the internal waves originating from the Luzon Straight in the South China Sea (Figure adopted from Simmons et al. [98]).

In general, internal waves can be further categorised into linear internal waves and nonlinear internal waves, depending on their dynamical characteristics. The frequencies ω of linear internal waves are always larger than the local inertial frequency $f = 2\,\Omega \sin \varphi$, where Ω is the rotation rate of the earth and φ is the latitude, and smaller than the buoyancy frequency N, that is $f < \omega < N$. By far, the most energetic linear internal waves are the near-inertia waves with frequencies $\omega \approx f$ and internal tides at the astronomical frequencies (dominantly the semidiurnal (two cycles per day) M2 tides). The former is usually generated due to the energy input from wind, while the latter is mainly due to the interaction between barotropic tidal currents and abrupt topographic features, see Alford [5, 6], as well as nonlinear waves forming due to nonlinear steepening, and they can be generated at the topographic site by critical flow (Froude number $\mathrm{Fr} = u/c = 1$, where u is a characteristic flow velocity and c is the wave propagation speed), or by tidal beams at the critical slope. Internal waves can propagate several thousand kilometers away from the genera-

tion sites before their eventual breaking and dissipation, see Ray and Mitchum [92]. After radiating from the generation sites, due to complicated oceanic background circumstances, internal waves may undergo nonlinear steepening and transform into nonlinear internal waves, often characterised as internal solitary waves. Figure 1.1 exhibits a typical life cycle of oceanic internal waves. In this thesis we only consider the evolution and propagation of internal solitary waves.

A large number of observations demonstrate the existence of internal solitary waves (ISWs) in numerous locations around the world's oceans, both from field measurements, see Ramp et al. [91], Shroyer and Nash [97], Huang et al. [55] and remote sensing images, see Zhao et al. [122], Da Silva et al. [21], Liu et al. [73]. Nevertheless, due to the complicated oceanic background, in addition to an isolated ISWs, nonlinear wave trains in a form of unsteady undular bores were also recorded and ISWs are often seen as the leading waves in internal undular bores. Unlike surface waves, ISWs can have an infinite set of modes. Here the terminology of "mode" indicates the vertical structure of the particle displacement, and hence the corresponding temperature, pressure, horizontal and vertical particle velocity fields, which are linked through the underlying Euler equations. Indeed, the emergence of multi-modes has been affirmed by plenty of observations, see figure 1.2 for instance. In general, mode-1 waves have been most commonly observed, although mode-2 and even mode-3 waves are also recorded, see Guo et al. [49], Yang et al. [113, 112], Shroyer and Nash [97], Liu et al. [73]. It was found that the energy transfer between different modes can emerge, for example, Vlasenko et al. [105] pointed out that interaction between mode-1 nonlinear internal waves and topography can result in a generation of mode-2 waves; Guo and Chen [47] examined the propagation of mode-2 waves over a shoaling topography, in which the conversion from the second to first mode was noticed.

Figure 1.3 illustrates the schematic of mode-1 and mode-2 internal solitary waves, which are the main interest in the ocean. Mode-1 wave can be either depression

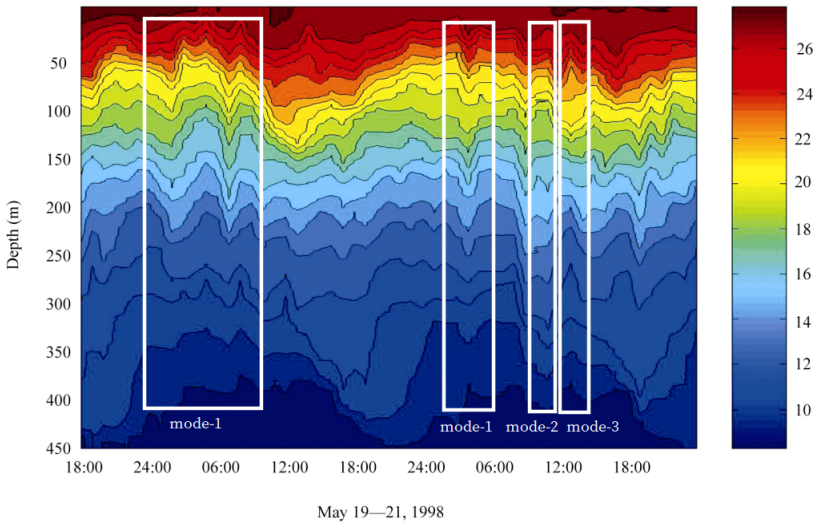

Figure 1.2: Time series of the temperature field in the South China Sea, reported by Guo et al. [49]

(negative) or elevation (positive) wave, so do mode-2 waves, but with a more complex structure. For mode-2 waves, an elevation wave is often called a "convex wave" as the upper (lower) pycnocline interface is displaced upwards (downwards). In contrast, a mode-2 depression wave is a "concave" wave, with an hourglass-shaped structure, as the upper (lower) pycnocline interface is displaced downwards (upwards). Although mode-2 internal waves are usually not as energetic as mode-1 waves, they can be significant for mixing shelf waters especially as their location is usually in the middle of the pycnocline, and hence they can be effective in eroding the barrier between the upper mixed layer and the deep water below.

Since internal waves can propagate for long distances over several inertial periods, the effect of the earth's background rotation will become significant. Farmer et al. [27] examined this problem with *in-situ* measurements and theoretical models and found that the rotational effect can suppress the emergence and evolution of internal solitary waves to some extent. This is understandable in the framework of the KdV-type equation, as the rotational effect is manifested as a low wavenumber dispersive term, in addition to the usual high wavenumber dispersion. Helfrich [51], Grimshaw and Helfrich [39] showed that due to the rotation, an initial large-amplitude solitary

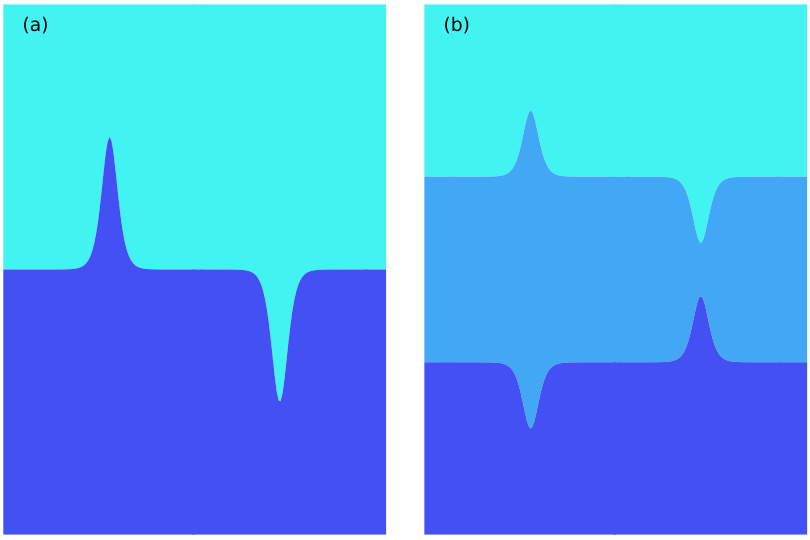

Figure 1.3: Schematic map shows the vertical displacement of mode-1 (a) and mode-2 (b) internal waves. In both panels, the left wave is the elevation wave, whereas the right is the depression wave.

wave decays into inertia-gravity waves, and eventually the leading disturbance forms into a coherent envelope wave packet. Later, Grimshaw et al. [46] corroborated this by laboratory experiments and furthermore they also found that even for more general inertia-gravity waves which are not originated from the radiation of ISWs, the involvement of the rotational effect can also lead to the emergence of nonlinear wave packets, albeit the time scale for this process has a possibility to be unrealistically long depending on the specific circumstances, also see Stastna et al. [100]. Then Grimshaw et al. [44] showed that the combined effect of shoaling and rotation is to induce a secondary trailing wave packet following the leading internal solitary waves in a realistic transect in the SCS.

The oceanic topography is essentially variable, especially at the coastal area. Indeed, the topographic effect on the propagation of internal solitary waves has been heavily studied and is now well understood, see the reviews by Grimshaw [37], Grimshaw et al. [42, 43]. Nonetheless, a large portion of the previous work was based on one-dimensional topography, whereas it is two-dimensional in reality. Although a few investigations considered the two-dimensional bathymetry, such as

Vlasenko and Stashchuk [104], Zhang et al. [121], they based their analyses on the numerical results of the Navier-Stokes equations, whose abilities to accurately simulate the phenomena, particularly for small-scale features, are highly dependent on the spatial and temporal grid steps and the parameterisation schemes implemented in the model. Furthermore, it is usually not easy to analytically explain and understand the results of the primitive equations, as they could include lots of dynamical processes of different scales and the interactions between them and can even render the features of main interest as distorted or hidden.

Due to complicated bathymetry, there can be more than one potential generation site for internal waves in the coastal ocean. For instance, in the South China Sea, three parts of the Luzon Straight are indicated as the major generation sites, as shown in figure 1.4, and also see Jan et al. [57], Alford et al. [7], Guo and Chen [48]. Further, after radiating from their generation sites, due to the variable oceanic background, ISWs can undergo refraction and reflection, see Liu and Hsu [72], Ramp et al. [91], Cai and Xie [15]. These factors jointly create the possibility that interactions between two or more internal solitary waves can occur. Indeed, in the world's ocean, a large number of wave interactions have been recorded using satellite Synthetic Aperture Radar (SAR) images; for instance, in the South China Sea, see Hsu et al. [54], Chen et al. [19]; in the Mid-Atlantic Bight, see Xue et al. [111]; off the cost of South-west Africa, see Zheng et al. [123]; a complete coverage is available in the internal wave atlas, see Jackson [56]. Satellite images themselves are usually unable to provide the interior wave structure and the associated motions, but nevertheless, Wang and Pawlowicz [107] investigated four cases of internal wave interactions in the Strait of Georgia using sequential photogrammetrical images acquired from an aircraft, and importantly, supplementary simultaneous collections of water column properties measured by a surface vessel.

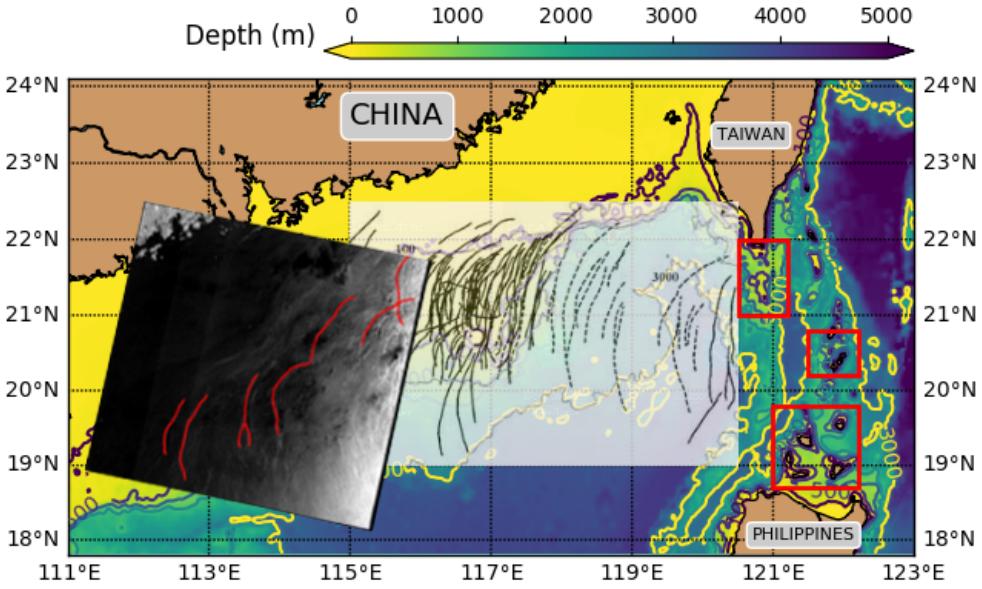

Figure 1.4: The bathymetry of the South China Sea. Three red rectangles indicate the potential generation sites, see Guo and Chen [48]. The transparent inset, adopted from Zhao et al. [122], shows the existence of the multiple-wave ISW packets (solid line) and single-wave ISW packets (dashed line), which is a collection of the satellite images acquired from 1995 to 2001. An Envisat-1 Advanced SAR satellite image on 02:20 UTC, 31-07-2010 is also imposed, where some wave crestlines are accentuated in red lines.

1.2 Theoretical background

Solitary waves were first observed by John Scott Russell on the Union Canal in 1834, see Russell [94]. Russell also conducted some laboratory experiments, in which elevation surface solitary waves were reproduced by dropping a weight at one end of a water tank, and the waves travelled with speed c where

$$c^2 = g(h + a)\,, \tag{1.1}$$

where a is the amplitude of the wave, h is the depth of the water at rest and g is the acceleration of gravity. Then both Boussinesq [14] and Rayleigh [93] achieved the formula (1.1) in an inviscid incompressible fluid with a long-wave assumption and also found the sech^2 wave profile, although a simple equation describing this wave profile was not given until the work by Korteweg & de Vries in 1895, see Korteweg and de Vries [67], who presented the well-known Korteweg-de Vries (KdV) equation,

$$U_t + UU_x + U_{xxx} = 0\,, \tag{1.2}$$

which embodies the cumulative and competing nonlinear and dispersive effects. Note that here subscripts x and t denote derivatives and for convenience, any desired coefficients have been absorbed into the variables x, t and U. It turned out the KdV equation was actually already available in the footnote on page 360 of Boussinesq's book in 1877, see Boussinesq [13]. However, Boussinesq's expression for the wave velocity is only valid when the wave vanishes at infinity, while this is not necessary in the theory of Korteweg and de Vries, see de Jager [22] for more details. Nevertheless, solitary waves did not get much attention until Zabusky and Kruskal [119] numerically integrated the KdV equation to investigate nonlinear wave interactions in a simple model. They found that the solitary waves held a prominent property

of retaining their wave profiles and speeds when they propagate and even after collisions with other solitary waves. This persistence of the waves inspired them to name these waves as 'solitons' after particles, such as photon, proton, etc. to accentuate that these waves can retain their identities in a collision. There is, however, an exception: they interact at a small incident angle, as found by Miles [79, 80] who pointed out that depending on the amplitudes and angles, a Mach stem (that is a resonant phase shift) can arise in the interaction zone. Importantly, Gardner et al. [29] pointed out that the KdV equation was integrable through the inverse scattering transform. Then Zakharov and Shabat [120] found that this method also could be used for the nonlinear Schrödinger equation which is another physically significant equation for wave dynamics. Using these ideas, Ablowitz et al. [2, 3] further developed this method to apply to a wide class of nonlinear evolution equations, see the book by Ablowitz and Segur [1]. Moreover, large-amplitude solitary waves and their breaking were investigated by Longuet-Higgins, see Longuet-Higgins and Fenton [76], Longuet-Higgins [75]. Nowadays it is recognised that a KdV-type equation can be used to describe a large number of physical problems. Thus both the KdV equation and the corresponding soliton theory are now an active research field, see the book by Drazin and Johnson [24].

In 1893, the Norwegian oceanographer Fridtjof Nansen first revealed the existence of oceanic internal waves in the Arctic Ocean when he sailed a ship which, occasionally, experienced strong resistance to forward motion in apparently calm conditions at the surface. Nevertheless, a quantitative measurement for internal waves was not available until the 1960s. By virtue of the development of modern instruments for *in-situ* observation, Perry and Schimke [90] recorded groups of internal waves with a maximum amplitude 80 m and a wavelength 2000 m on the main thermocline at 500 m in water which is 1500 m deep in the Andaman Sea, which is among the earliest quantitative measurements of oceanic internal waves. Then Ziegenbein

[125, 126] illustrated clear observational evidence of internal solitary waves in the Strait of Gibraltar. These waves were also observed with associated surface waves in the Andaman Sea by Osborne and Burch [85]. They exhibited a paradigm for the implementation of the KdV equation to internal solitary waves. These early observers were aware that these internal solitary waves could be described by the KdV equation and especially an exact (asymptotic) solution of rank-ordered internal solitary waves exists, as found by Gardner et al. [29]. Subsequently, several theories on nonlinear internal waves have been proposed and have been scrutinised and validated by their implementations to the analyses of data from both *in-situ* observations and laboratory experiments, see the recent review by Helfrich and Melville [52].

In the context of nonlinear internal waves, Benney [12], Benjamin [10] first derived the KdV equation for the description of uni-directional weakly nonlinear long waves. Based on this classic KdV equation, several variants emerged, including the extended KdV equation incorporating an additional cubic nonlinear term U^2U_x c.f. expression (1.2), see references of Lee and Beardsley [70], Djordjevic and Redekopp [23], Grimshaw et al. [40]; the rotation-modified KdV equation including the earth's rotation $-\int_x f^2/(2c)U\,dx$ where f is the Coriolis frequency (or called local inertial frequency as before) and c is the linear phase speed, see Ostrovsky [87], Grimshaw [35]; the KdV equation with bottom friction, see the book by Grimshaw [36]. Other forms of dissipation can be used, see Grimshaw et al. [41]; the KdV equation including the effect of background shear and continuous stratification, see Grimshaw [34], Zhou and Grimshaw [124], in which they also showed that the effects of slowly varying depth can be accounted for by including a weak additional term, see also Holloway et al. [53]; a two-dimensional version of the KdV equation is the Kadomtsev-Petviashvili (KP) equation, see Kadomtsev and Petviashvili [59], Grimshaw [34]. Note that theoretically a KdV-type equation is only applied to the case that the wavelength is large with respect to the depth, that is in the shallow water, whereas

the weakly nonlinear Benjamin-Ono (BO) equation was derived for infinitely deep fluids, see Benjamin [10], Ono [84] and for intermediate depth, the Intermediate Long Wave (ILW) equation proposed by Joseph [58], Kubota et al. [68] can be considered. However, several investigations concluded that KdV-type theories still have a good performance even for large-amplitude waves which are formally beyond the scope of the weakly nonlinear assumption, see for instance Koop and Butler [66], Small et al. [99], Ostrovsky and Stepanyants [88]. Through comparisons with laboratory experimental data, Ostrovsky and Stepanyants [88] pointed out that KdV-type model provides satisfactory results, sometimes even outside its formal validity, while the BO and ILW equations have narrower ranges of validity and fail to make good predictions beyond these ranges. They also cautioned that the interpretation of observational data using the BO and ILW equations should be given much care, although Wang and Pawlowicz [106] achieved a better result with the BO equation than the KdV equation when they considered large-amplitude nonlinear internal waves in deep water.

Although the KdV equation has been successfully and widely used to study the properties of solitary wave solutions as well as to interpret data from *in-situ* measurements and laboratory experiments, the weakly nonlinear assumption (the BO and ILW equations are also based on this) limits their applications especially when large-amplitude waves are involved. As a useful extension of the weakly nonlinear two-layer extended KdV equation (with cubic nonlinear term), the Miyata-Choi-Camassa (MCC) equations with full nonlinearity and weak dispersion were derived by Miyata [82, 83], Choi and Camassa [20]. Despite that MCC equations are only for a two-layer fluid, these equations are bi-directional (c.f. the uni-directional feature of the KdV equation), and Choi and Camassa [20] illustrated very good agreement with both results from laboratory experiments and numerical solutions of the Euler equations. Then later Ostrovsky and Grue [89] obtained uni-directional evolution

equations which take nonlinear dispersive effects into account. These equations generally agree very well with the MCC equations and further preclude the intrinsic Kelvin-Helmholtz instability at high wavenumbers in the MCC equations. Nevertheless, a more accurate way to investigate solitary waves is in the framework of the Euler equations without assumptions of weak nonlinearity or/and weak dispersion. The Dubreil-Jacotin-Long (DJL) equation describes the streamline displacement in the form of a strongly nonlinear elliptic partial differential equation, which amounts to the full set of stratified Euler equations, see the early references by Long [74] and later Benjamin [10], Tung et al. [103].

One of the distinctions between surface waves and internal waves is that the latter can have different vertical modes, whereas there is only one for the former, as mentioned in section 1.1, see also figure 1.3. However the aforementioned KdV-type theories are only able to accommodate a single mode, therefore to examine the energy flow between different modes, Gear and Grimshaw [30] developed coupled KdV equations, each is the KdV equation with an additional linear coupled term, to study the interactions between internal waves of different modes, also see Grimshaw [38]. Recently, Alias et al. [8, 9] further developed this to also take the effect of rotation and background shear into consideration.

Nowadays by virtue of the rapid development of the techniques of computational fluid dynamics together with the availability of powerful supercomputers, a comprehensive oceanic model possessing the ability of resolving a large number of dynamical processes simultaneously, such as ice melting, solar radiation input, wave propagation, meso-scale eddies generation, is available for the eventual purpose of prediction, although at this stage the results are far from satisfactory. These models are based on the primitive Navier-Stokes equations and usually it is impractical to simulate in a large domain with a sufficiently fine resolution to resolve very small-scale dynamics such as turbulence, which means several parameterisation schemes are necessary to

represent the contributions of these unresolved phenomena. In addition to the validation of sufficient observational data, a deep insight on the dynamical processes is also indispensable for the design of parameterisation schemes. However, the Navier-Stokes equations themselves are generally not convenient to explore properties of a specific phenomenon and so that reduced theories are needed. Because theoretical investigations of internal solitary waves are still very important, in this thesis we use a set of KdV-type equations to examine internal solitary waves over variable topography, supplemented by the simulations using the MIT general circulation model (MITgcm), which numerically solves the full Navier-Stokes equations.

1.3 Outline

The structure of this thesis is arranged as follows:

- Chapter 2 presents the KdV-type theory both in a constant and a variable environment, which forms the theoretical basis of this thesis.

- Chapter 3 focuses on the evolution of nonlinear internal waves over variable topography in the presence of rotation. The relevant paper is Yuan et al. [117]. The large-amplitude internal waves commonly observed in the coastal ocean often take the form of unsteady undular bores. Hence, here we examine the long-time combined effect of variable topography and background rotation on the propagation of internal undular bores, using the framework of a variable-coefficient Ostrovsky equation, that is the KdV equation with a rotational term.

- Chapter 4 examines the evolution of mode-2 internal solitary waves over a shoaling topography jointly using the variable-coefficient KdV equation and the MITgcm. The relevant paper is Yuan et al. [116]. Two configurations are

considered. One is a mode-2 internal solitary wave propagating up a slope, from one three-layer system to another three-layer system. The other configuration is when the lower layer in the three-layer system goes to zero at a transition point on the slope, and beyond that point, there is a two-layer fluid system. A mode-2 internal solitary wave propagating up the slope cannot exist past this transition point. Instead it is extinguished and replaced by a mode-1 bore and trailing wave packet which moves onto the shelf.

- Chapter 5 investigates two-dimensional topographic effects on the propagation of mode-1 internal solitary waves in the framework of the variable- coefficient KP equation and the relevant paper is Yuan et al. [118]. To illustrate the theory, we use a typical monthly averaged density stratification, for the propagation of an internal solitary wave over either a submarine canyon or a submarine plateau. The evolution is essentially determined by two components, nonlinear effects in the main propagation direction, and diffraction modulation effects in the transverse direction.

- Chapter 6 is devoted to topographic effects on wave interactions between two oblique internal solitary waves using a variable-coefficient KP equation. This work is submitted to the *Journal of Fluid Mechanics* and under review. In the absence of rotation and background shear, the model set-up featuring idealised shoaling topography and continuous stratification is motivated by the large expanse of continental shelf in the South China Sea. When the bottom is flat, the evolution of an initial wave consisting of two branches of internal solitary waves can be categorised into six patterns depending on the respective amplitudes and the oblique angles measured counterclockwise from the transverse axis. Using theoretical multi-soliton solutions of the constant-coefficient KP equation, we select three observed patterns and examine each of them in detail both analytically and numerically. The effect of shoaling topography leads to

a complicated structure of the leading waves and the emergence of two types of trailing wave trains. Further, the case when the along-crest width is short compared with the transverse domain is of interest and is examined and it is found that although the topographic effect can still modulate the wave field, the spreading effect in the transverse direction is dominant.

- Chapter 7 presents some future possible work.

Chapter 2

Formulation

2.1 KdV-type equation

As introduced in Chapter 1, a number of variants of KdV-type theory, derived from the Euler equations based on the assumption of weakly nonlinear long waves, can be used to model internal waves in the ocean when different dynamical factors (such as rotation, variable topography etc.) are taken into account. In the absence of dissipation, following Grimshaw [34, 35], oceanic internal waves can be described by the KdV-type equation,

$$\{A_t + cA_x + \alpha AA_x + \beta A_{xxx}\}_x + \frac{\gamma}{2}A_{yy} = \delta A\,, \tag{2.1}$$

where $A(x, y, t)$ is the amplitude of the wave, x, y and t are space and time variables respectively, and subscripts denote derivatives. Here x is chosen to be along the primary wave propagation direction, where the waves have a linear long-wave phase speed c, while y is the transverse direction where there are weak diffraction effects. The nonlinear coefficient α, dispersive coefficients β, γ and rotational coefficient δ are determined by the waveguide properties, and for the specific oceanic application, are defined below.

To leading order in an asymptotic expansion, the vertical particle displacement relative to the basic state is

$$\varsigma(x, y, z, t) = A(x, y, t)\phi(z), \tag{2.2}$$

where $\phi(z)$ is the modal function, defined by the solution of

$$\left\{\rho_0 \left(c - u_0\right)^2 \phi_z\right\}_z + \rho_0 N^2 \phi = 0 \,, \quad \text{for} \quad -h < z < 0 \,, \tag{2.3}$$

$$\phi = 0 \quad \text{at} \quad z = -h \,, \quad \left(c - u_0\right)^2 \phi_z = g\phi \quad \text{at} \quad z = 0 \,. \tag{2.4}$$

Here $\rho_0(z)$ is the background density distribution of a stable stratified fluid, which is mostly characterised by the buoyancy frequency N, represented by $\rho_0 N^2 = -g\rho_{0z}$, and $u_0(z)$ is a background horizontal shear flow. Note that if the rigid lid approximation is assumed, then the free surface boundary condition is replaced by $\phi = 0$ at $z = 0$. The coefficients α, β and γ in equation (2.1) are given by

$$I\alpha = 3 \int_{-h}^{0} \rho_0 \left(c - u_0\right)^2 \phi_z^3 \, dz \,, \tag{2.5}$$

$$I\beta = \int_{-h}^{0} \rho_0 \left(c - u_0\right)^2 \phi^2 \, dz \,, \tag{2.6}$$

$$I\gamma = 2 \int_{-h}^{0} \rho_0 (c - u_0)^2 \phi_z^2 \, dz \,. \tag{2.7}$$

$$I = 2 \int_{-h}^{0} \rho_0 \left(c - u_0\right) \phi_z^2 \, dz \,, \tag{2.8}$$

whereas the coefficient δ is given by

$$I\delta = f^2 \int_{-h}^{0} \rho_0 \Phi \phi_z \, dz \,, \quad \rho_0 (c - u_0)\Phi = \rho_0 (c - u_0)\phi_z - (\rho_0 u_0)_z \phi \,. \tag{2.9}$$

Note that when there is no shear flow, $u_0(z) \equiv 0$, the coefficients γ and δ are simplified

as

$$\gamma = c\,, \tag{2.10}$$

$$\delta = \frac{f^2}{2c}\,, \tag{2.11}$$

where f is the Coriolis frequency. Note that in this case, since $\beta > 0$, then the normal situation $\beta\delta > 0$ holds. In contrast, when there is a shear flow, for sufficiently strong shear it is possible to have the anomalous case when $\beta\delta < 0$. This is unlikely in oceanic conditions, although that case has been looked at in Grimshaw et al. [45], Whitfield and Johnson [108].

2.2 Variable background

In the presence of a slowly varying background, specifically when the fluid depth h varies slowly with x and y, the KdV-type equation (2.1) is replaced by

$$\left\{A_t + cA_x + \frac{cQ_x}{2Q}A + \alpha AA_x + \beta A_{xxx}\right\}_x + \frac{\gamma}{2}A_{yy} = \delta A\,, \tag{2.12}$$

where $Q = c^2 I$ (see (2.8) for the definition of I) is the linear magnification factor so that QA^2 is the linear long-wave wave-action flux. For simplicity here we assume that the background density $\rho_0(z)$ and shear flow $u_0(z)$ do not vary with $x\,, y$. If they did then an extra term is needed in the KdV part of the equation (the terms inside the bracket in (2.12)), see Zhou and Grimshaw [124]. The modal equation now also depends parametrically on x and y, that is $\phi = \phi(z; x, y)$, $c = c(x, y)$, and hence the coefficients $\alpha, \beta, \gamma, \delta, Q$ also depend (slowly) on x and y. Since the modal equations (2.3, 2.4) are homogeneous, ϕ can be non-dimensionalised with the maximum value 1, and the linear magnification factor Q can be normalised to be unity at the initial location. It is useful to express equation (2.12) in non-dimensional variables based on a length scale h_0 (a typical depth), and a velocity scale c_0 (a typical linear long

wave speed), so that the time scale is $t_0 = h_0/c_0$. For instance in an ocean setting, $h_0 = 500\,\mathrm{m}$ and $c_0 = 1\,\mathrm{m/s}$ can be chosen as a typical scaling. If needed, the density ρ_0 can also be scaled with $\rho_{00} = 1000\ \mathrm{kg/m^3}$. Then we have

$$\begin{aligned} &A = h_0\widetilde{A}\,, \quad x = h_0\widetilde{x}\,, \quad t = \frac{h_0\widetilde{t}}{c_0}\,, \quad (c,u) = c_0(\widetilde{c},\widetilde{u})\,, \\ &\alpha = \frac{c_0}{h_0}\widetilde{\alpha}\,, \quad \beta = c_0h_0^2\widetilde{\beta}\,, \quad \gamma = c_0\widetilde{\gamma}\,, \quad \delta = \frac{c_0}{h_0^2}\widetilde{\delta}\,. \end{aligned} \tag{2.13}$$

As a consequence, equation (2.12) is recovered in the $\widetilde{\ }$ variables, and also all expressions (2.5 - 2.11) hold in the $\widetilde{\ }$ variables. Note that with $f = 10^{-4}\,s^{-1}$ (approximately located at latitude 43° N) and in the absence of a background shear flow, $\widetilde{\delta} \sim f^2h_0^2/2c_0^2 \sim 10^{-3} \ll 1$, while $\widetilde{c}$, $\widetilde{\alpha}$, $\widetilde{\beta}, \widetilde{\gamma}$ are relatively order unity. As expected, in this oceanic application the rotational term can be regarded as a small perturbation to the usual KdV-type equation.

Formally, in terms of a small parameter ϵ, the square of the ratio of horizontal to vertical scale, used in the asymptotic derivation of equation (2.12), the coefficients depend on slow variables $\widehat{x} = \epsilon^3 x$ and $\widehat{y} = \epsilon^3 y$, and the corresponding amplitude is $\epsilon^2 A(\epsilon x, \epsilon^2 y, \epsilon t)$. As a consequence, to keep equation (2.12) in a valid asymptotic regime, in essence, the y-variations should be suppressed vis-à-vis the x-variations, since x is the dominant direction. Although this property might seem to impose another limitation on any application, in practice this is often the situation in the real ocean, that is, if the wave propagation direction is selected to be x, then the variations along the transverse y direction are much smaller. Also note that the derivation of equation (2.12) by Grimshaw [34] was along the ray path determined by the linear long wave speed c, and then taking account of diffraction relative to this ray. But here we choose the x-direction as the ray, consistent with our choice of topography being symmetric about that axis.

It is clear that the first two terms of equation (2.12) are dominant terms, and

hence we can transform it to an asymptotically equivalent "spatial" evolution form for $A(X,T)$,

$$X = \int_{x_0}^{x} \frac{dx}{c} - t\,, \quad T = \int_{x_0}^{x} \frac{dx}{c}\,, \tag{2.14}$$

$$\left\{ A_T + \frac{Q_T}{2Q}A + \mu A A_X + \lambda A_{XXX} \right\}_X + \frac{\sigma}{2}A_{yy} = \eta A\,, \tag{2.15}$$

$$\mu = \frac{\alpha}{c}\,, \quad \lambda = \frac{\beta}{c^3}\,, \quad \sigma = c\gamma\,, \quad \eta = c\delta\,. \tag{2.16}$$

All terms are now of the same order, that is, $A \sim \epsilon^2$, $\partial/\partial X \sim \epsilon$, $\partial/\partial T \sim \epsilon^3$, $\partial/\partial y \sim \epsilon^2$ and $\eta \sim \epsilon^4$. Here the coefficients $\mu, \lambda, Q, \sigma, \eta$ depend on T and y, but note that in the absence of a background shear flow, $\eta = f^2/2$ is independent of T and y. But note that the y-dependence in these coefficients is order $\mathcal{O}(\epsilon^3)$, much slower than the y-variation of A, which is order $\mathcal{O}(\epsilon^2)$ formally. Further simplifications are

$$U = A\sqrt{Q}\,, \quad \left\{ U_T + \frac{\mu}{\sqrt{Q}} U U_X + \lambda U_{XXX} \right\}_X + \frac{\sigma}{2}U_{yy} = \eta U\,, \tag{2.17}$$

Without loss of generality, we can assume that the wave propagate in the positive x-direction, so that $\lambda > 0$. Then (2.17) can be further transformed exactly to

$$\{U_s + \nu U U_X + U_{XXX}\}_X + \tau U_{yy} = \zeta U\,, \tag{2.18}$$

$$\text{where} \quad s = \int_0^T \lambda(T')\,dT'\,, \quad \nu = \frac{\mu}{\lambda\sqrt{Q}}\,, \quad \tau = \frac{\sigma}{2\lambda}\,, \quad \zeta = \frac{\eta}{\lambda}\,. \tag{2.19}$$

Equation (2.18) can be written in an alternative form,

$$U_s + \nu U U_X + U_{XXX} + \tau V_{yy} = \zeta V\,, \quad V_X = U\,, \quad V = -\int_X^{+\infty} U(s, X', y)\,dX'\,, \tag{2.20}$$

where we assume that both $U, V \to 0$ as $X \to +\infty$, since linear waves have negative

group velocity. This equation has two important conservation laws,

$$\int_{-\infty}^{+\infty} U\,dx = [V]_{-\infty}^{\infty} = 0\,, \tag{2.21}$$

$$\frac{\partial}{\partial s}\int_{-\infty}^{+\infty} \frac{U^2}{2}\,dX + \tau\frac{\partial}{\partial y}\int_{-\infty}^{+\infty} UV_y\,dX = 0\,, \tag{2.22}$$

for solutions $U(s, X, y)$ localised (or periodic) in X, which represent conservation of mass and wave action flux respectively.

It is useful to clarify here the relationship between the wave amplitude in the transformed space and the wave amplitude in the physical space. For a solitary wave in the transformed space (X, y, s), along a fixed y section line ($y = 0$ for instance), the maximum amplitude at "time" s can be expressed as

$$U_m = U(s, X_m(s))\,, \quad \text{where} \quad U_X = 0 \text{ at } X = X_m(s)\,, \tag{2.23}$$

where $|U_m|$ is a local maximum, and the y-dependence is suppressed. Analogously in physical space, the maximum amplitude at the location x is written as

$$A_m = A(t_m(x), x)\,, \quad \text{where} \quad A_t = 0 \text{ at } t = t_m(x)\,, \tag{2.24}$$

where $|A_m|$ is a local maximum. Then since $U = A\sqrt{Q}$ (2.17), and using the transforms (2.14),

$$\lambda U_s = (A\sqrt{Q})_t + c(A\sqrt{Q})_x\,, \quad U_X = -(A\sqrt{Q})_t\,. \tag{2.25}$$

Since here it transpires that the variation of Q is quite small usually, we see that the maximum in the transformed and physical spaces approximately coincide. Importantly, note that the maximum in the transformed space is a maximum over X at a fixed "time" s, and this coincides, modulo any small variation in Q, with a maximum over time t in the physical space at a fixed location x, such as would be observed at

a fixed mooring site.

2.3 Numerical method

In this thesis, our analyses are largely based on equation (2.18), which is numerically solved in the transformed space and depending on the specific situations, some of the results will be recast to the physical space through the transformation (2.14). A pseudo-spectral method based on a Fourier interpolant is used in the primary wave propagation (that is X here) direction, and the dispersion along the y direction is simulated by a fourth order central finite difference scheme, while a classical Runge-Kutta fourth-order method, together with a very small time step, provides an accurate outcome in the time domain.

Instead of being written in the obvious manner, the code is constructed in a modified form, based on the method of integrating factors, which allows relatively large time steps to be taken, see Trefethen [101] for more details. To circumvent the problem of stiffness, one way to proceed is to write (2.18) as

$$\left\{U_s + \frac{1}{2}\nu(U^2)_X + U_{XXX}\right\}_X + \tau U_{yy} = \zeta U\,. \tag{2.26}$$

Applying Fourier transforms in the X direction gives

$$ik\left(\widehat{U}_s + \frac{1}{2}ik\nu\widehat{U^2} - ik^3\widehat{U}\right) + \tau\widehat{U_{yy}} = \zeta\widehat{U}\,. \tag{2.27}$$

Note that here the coefficients ν, τ, ζ depend on s, y, but not X. Now multiply (2.27) by $e^{-ik^3 s}$, this is the integrating factor, to get

$$ik\left(e^{-ik^3 s}\widehat{U}_s + \frac{1}{2}ike^{-ik^3 s}\nu\widehat{U^2} - ik^3 e^{-ik^3 s}\widehat{U}\right) + \tau e^{-ik^3 s}\widehat{U_{yy}} = \zeta e^{-ik^3 s}\widehat{U}\,, \tag{2.28}$$

then define $\widehat{M} = e^{-ik^3 s}\widehat{U}$, with $\widehat{M}_s = -ik^3 e^{-ik^3 s}\widehat{U} + e^{-ik^3 s}\widehat{U}_s$, this becomes,

$$ik\left(\widehat{M}_s + \frac{1}{2}ike^{-ik^3 s}\nu\widehat{U^2}\right) + \tau e^{-ik^3 s}\widehat{U_{yy}} = \zeta\widehat{M}\,. \tag{2.29}$$

Working in Fourier space, the problem can be discretized as

$$ik\left\{\widehat{M}_s + \frac{1}{2}ike^{-ik^3 s}\nu\mathscr{F}\left[\left(\mathscr{F}^{-1}(e^{ik^3 s}\widehat{M})\right)^2\right]\right\} + \tau e^{-ik^3 s}\left\{\mathscr{F}\left[\left(\mathscr{F}^{-1}(e^{ik^3 s}\widehat{M})\right)_{yy}\right]\right\} = \zeta\widehat{M}\,, \tag{2.30}$$

where $\mathscr{F}$ is the Fourier transform operator. Here the term ∂_y^2 is approximated by a fourth-order central finite difference method. Note that the mass conservation law (2.21) has to be satisfied, thus a pedestal (expressions will be given below) is imposed on the initial condition to ensure the initial mass is zero, which also means that in Fourier space, initially when $k = 0$, the corresponding component of $\widehat{M}$ (or $\widehat{U}$) equals zero.

2.4 Massachusetts Institute of Technology general circulation model

The Massachusetts Institute of Technology general circulation model (MITgcm) is a numerical model designed for the study of both atmospheric and oceanic phenomena with various scales, see Marshall et al. [77, 78] for more details. This model uses a finite-volume method and it is based on the spatially three-dimensional incompressible Navier Stokes equations, which has been successfully used to study internal waves in the ocean, see Vlasenko et al. [105], Guo and Chen [47]. Note that although the MITgcm is a comprehensive model that can be implemented

to investigate problems in different coordinates (such as spherical and Cartesian coordinates) using different parameterisations, only contents related to the specific use in this thesis are described in this section, see the manual online (`http://mitgcm.org/public/r2_manual/latest/online_documents/manual.pdf`) for a full description.

In a traditional Cartesian coordinate in which z axis points upwards, given that the rotational effect is neglected, the governing equations are

$$\frac{\partial u}{\partial t} + \frac{\partial p}{\partial x} = G_u \,, \tag{2.31}$$

$$\frac{\partial v}{\partial t} + \frac{\partial p}{\partial y} = G_v \,, \tag{2.32}$$

$$\frac{\partial w}{\partial t} + \frac{\partial p}{\partial z} = G_w \,, \tag{2.33}$$

$$\frac{\partial u}{\partial x} + \frac{\partial v}{\partial y} + \frac{\partial w}{\partial z} = 0 \,, \tag{2.34}$$

$$\frac{\partial T}{\partial t} = G_T \,, \tag{2.35}$$

$$\frac{\partial S}{\partial t} = G_S \,, \tag{2.36}$$

$$\rho = \rho(T, S, p) \,, \tag{2.37}$$

where u, v and w are horizontal and vertical velocities; t is time. Potential temperature T, salinity S, pressure p and density ρ characterize the basic state of the ocean. Equations (2.31)-(2.33) are the momentum equations; Equation (2.34) represents mass conservation; Equations (2.35) and (2.36) are the thermodynamic equations, while equation (2.37) is the Equation of State which is a nonlinear equation and in practice it is usually calculated using some empirical expressions. Terms G_u, G_v, G_w are compact forms representing advection and forcing/dissipation terms in horizontal

and vertical directions, defined by

$$G_u = -\mathbf{v} \cdot \nabla u + F_u \,, \tag{2.38}$$

$$G_v = -\mathbf{v} \cdot \nabla v + F_v \,, \tag{2.39}$$

$$G_w = -\mathbf{v} \cdot \nabla w + F_w - g\frac{\delta\rho}{\rho_{ref}} \,, \tag{2.40}$$

where $\mathbf{v} = (u, v, w)$ is the velocity vector, ∇ is the gradient operator, while the last term in equation (2.40) represents the buoyancy term in which g is the gravitational acceleration, $\delta\rho$ is the deviation of pressure from the rest state, and ρ_{ref} is the constant reference density. Note that Marshall et al. [78] gave full expressions of these terms in spherical coordinate. Then in the thermodynamic equations,

$$G_T = -\nabla \cdot (\mathbf{v}T) + F_T \,, \tag{2.41}$$

$$G_S = -\nabla \cdot (\mathbf{v}S) + F_S \,. \tag{2.42}$$

The above equations (2.31)-(2.42) are hence discretised and solved with a supplement of appropriate boundary conditions and initial conditions, and numerical schemes. For the initial conditions we use in this thesis will be given in the following chapters when the model is invoked, while the algorithms and boundary conditions will be briefed below.

Depending on the scales and features of fluid motion and the trade-off between the numerical resources consumed and accuracy achieved, most of numerical models are based on the 'hydrostatic primitive equations', in which the vertical momentum equation (2.33) is reduced to the state of hydrostatic balance, that is,

$$\frac{\partial p_{HY}}{\partial z} + \widetilde{g} = 0 \,, \tag{2.43}$$

where $\widetilde{g} = g\,\delta\rho/\rho_{ref}$ is the reduced gravity. p_{HY}, denoting the hydrostatic pressure, is one of the three components of the pressure p, while the other two are surface pressure p_S and nonhydrostatic pressure p_{NH}, i.e. $p = p_S + p_{HY} + p_{NH}$, see Marshall et al. [78] for more details. In some cases, the hydrostatic model is not a good approximation, thus the strict hydrostatic balance is relaxed to involve the metric and Coriolis terms (not applicable in this thesis) and omit the advection and forcing/dissipation terms as in the hydrostatic model. This is called quasi-hydrostatic model, see Marshall et al. [77, 78]. When the incompressible Navier Stokes equations are employed, then it is called nonhydrostatic model, which undoubtedly needs much more massive computational power than the former two reduced equation sets. A parameter that indicates the validity of the hydrostatic model is defined as, see Marshall et al. [78],

$$\Im = \frac{\eth^{\,2}}{R_i}\,, \tag{2.44}$$

where $\eth = h/L$ is an aspect ratio of the motion and $R_i = N^2h^2/u_0^2$ is the Richardson number. Here h and L are the vertical and horizontal scales of the system, respectively. u_0 is the horizontal velocity scale and N is the buoyancy frequency. When $\Im \ll 1$, the motion usually can be delineated by hydrostatic model with satisfactory accuracy. Nevertheless, in terms of internal solitary waves which we investigate in this thesis, the hydrostatic approximation is insufficient, thus the nonhydrostatic terms must be involved.

The discretized form of the nonhydrostatic equations (2.31)-(2.36) in time domain with a time step Δt is given by

$$\frac{u^{n+1} - u^n}{\Delta t} = G_u^{n+1/2} - \frac{\partial}{\partial x}\left\{p_S + p_{HY} + p_{NH}\right\}^{n+1/2}\,, \tag{2.45}$$

$$\frac{v^{n+1} - v^n}{\Delta t} = G_v^{n+1/2} - \frac{\partial}{\partial y}\left\{p_S + p_{HY} + p_{NH}\right\}^{n+1/2}\,, \tag{2.46}$$

$$\frac{w^{n+1}-w^n}{\Delta t} = \widetilde{G}_w^{n+1/2} - \frac{\partial}{\partial z} p_{NH}^{n+1/2}\,, \tag{2.47}$$

$$\frac{\partial u^{n+1}}{\partial x} + \frac{\partial v^{n+1}}{\partial y} + \frac{\partial w^{n+1}}{\partial z} = 0\,, \tag{2.48}$$

$$\frac{T^{n+1}-T^n}{\Delta t} = G_T^{n+1/2}\,, \tag{2.49}$$

$$\frac{S^{n+1}-S^n}{\Delta t} = G_S^{n+1/2}\,, \tag{2.50}$$

where n indicates the nth time step and $\widetilde{G}_w = G_w + \widetilde{g}$. The intermediate terms $G^{n+1/2}$ are evaluated explicitly using the quasi-second order Adams-Bashforth method, see Marshall et al. [77] for more details.

The core of the algorithms used by the MITgcm is the so-called 'pressure correction' method where the pressure field is obtained by solving a Poisson equation with Neumann boundary conditions in a complicated geometry as that of the ocean basins. Details were given in Marshall et al. [77, 78], and will only be summarised here. As shown in figure 2.1, at first, a 2D elliptic equation is inverted in order to obtain the surface pressure p_S through a repeated iteration until the prescribed residual limit reaches, and the hydrostatic pressure p_{HY} at a certain depth can be acquired by an integration of the fluid from the surface to this depth, in which the value of the potential temperature T and salinity S must be solved. Then if the model were hydrostatic or quasi-hydrostatic, the horizontal velocities u and v could step forward readily, while the vertical velocity w could be solved through the continuity equation. Nonetheless, for nonhydrostatic equations, before forwarding the velocities, a further 3D elliptic equation must be inverted to achieve the nonhydrostatic pressure p_{NH}. After p_{NH} is solved, the vertical velocity w is then stepped forward using the vertical momentum equation (2.47).

In spatial domain, the MITgcm is conducted using the finite volume method, which divides the simulated ocean into a number of 'volumes' and the variable fluxes are defined normal to the surfaces of the volumes. In addition, to represent the

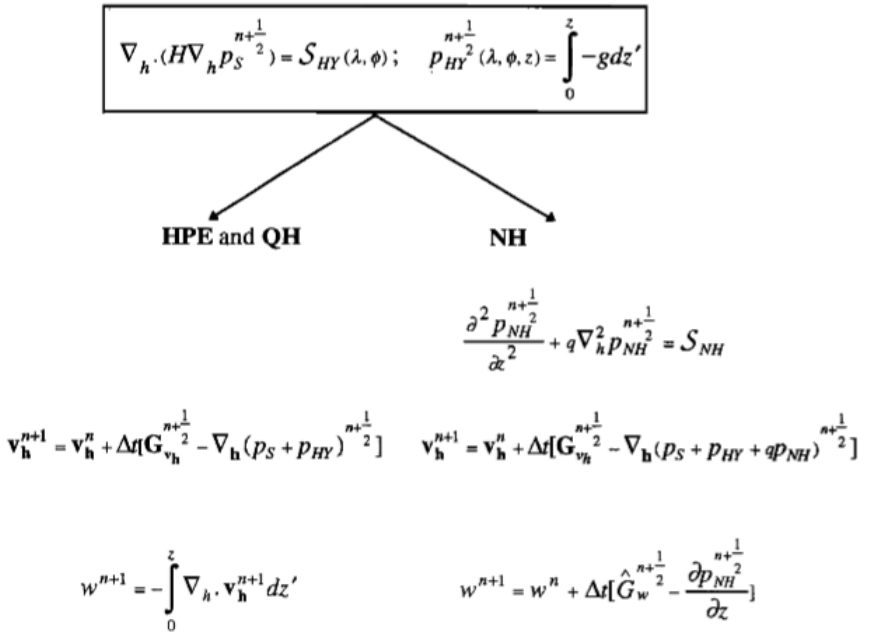

Figure 2.1: Algorithms used by the MITgcm model. HPE and QH indicate the hydrostatic and quasi-hydrostatic equations, respectively, while NH denotes the non-hydrostatic equations (Figure adopted from Marshall et al. [77]).

bottom topography accurately, an 'intersecting boundary method' is invoked, see the manual online.

Since in this thesis, the MITgcm is only used to carry out process model study, there are not parametersiation schemes being involved except that second-order viscosities are added to stabilize the model. The horizontal viscosity (A_h as in the model) is calculated using the scheme due to Leith, see Leith [71], in which viscosity is proportional to the magnitude of the relative vorticity ($|\nabla \bar{w}_3|$) and grid step ΔL, where the overbar indicates a filter over the subgrid scale ΔL, that is

$$A_{hLeith} = \left(\frac{viscC2Leith}{\pi}\right)^3 (\Delta L)^3 |\nabla \bar{w}_3| \,, \tag{2.51}$$

where $viscC2Leith$ is a tunable coefficient in the model, and it equals 2.0 here.

To prevent wave reflections at computational boundaries, a grid telescoping technique is employed in the model, that is, in the boundary layer the spatial grid step

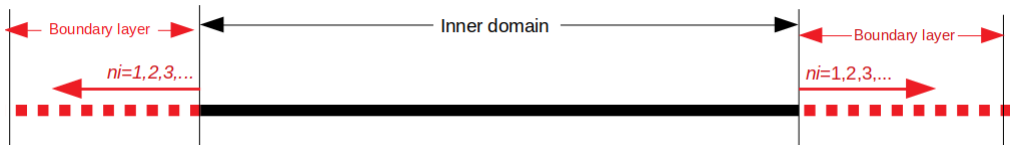

Figure 2.2: Schema of the computational domain in the MITgcm.

increases exponentially. The expression is given by

$$\Delta L_b = \Delta L_i (1 + fa)^{(ni-1)/fb}, \tag{2.52}$$

where ni is the index of the grid numbers in the boundary layer and it starts from 1 at the first point outside the inner domain, then increases outwards, see figure 2.2; ΔL_i and ΔL_b are grid steps in the inner domain and boundary layer, respectively; fa and fb are two tunable coefficients. A similar scheme was also employed in Guo and Chen [47], Vlasenko et al. [105].

Chapter 3

The combined effect of topography and Earth's rotation on the evolution of internal undular bore

The large-amplitude internal waves commonly observed in the coastal ocean often take the form of unsteady undular bores. Hence, in this chapter we examine the long-time combined effect of variable topography and background rotation on the propagation of internal undular bores, using the framework of the variable-coefficient Ostrovsky equation which, following equation (2.18) in Chapter 2, is written in the transformed space as

$$\{U_s + \nu U U_X + U_{XXX}\}_X = \zeta U \,. \tag{3.1}$$

3.1 Solitary wave extinction

The linear dispersion relation of the constant-coefficient Ostrovsky equation (3.1) for sinusoidal waves $\sin(kX - \omega s)$ is,

$$\omega = \frac{\zeta}{k} - k^3 \,, \tag{3.2}$$

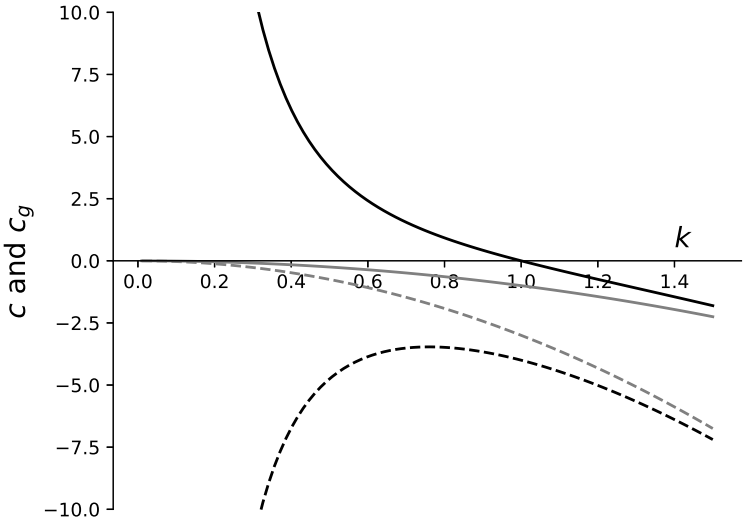

Figure 3.1: The phase speed c and group velocity c_g in (3.3, 3.4) are shown by solid and dashed lines respectively. The Ostrovksy equation ($\zeta = 1$ in equation (3.1)) is in dark, whereas the KdV equation ($\zeta = 0$ in (3.1)) is in grey.

and hence the phase speed and the group velocity are given by

$$\text{phase speed}: \quad c = \frac{\omega}{k} = \frac{\zeta}{k^2} - k^2\,; \tag{3.3}$$

$$\text{group velocity}: \quad c_g = \frac{d\omega}{dk} = -\frac{\zeta}{k^2} - 3k^2\,. \tag{3.4}$$

This dispersion relation plotted in figure 3.1 shows that the Ostrovsky equation is not able to support a steady solitary wave solution, as there is no gap in the linear spectrum for the phase speed c. This is in stark contrast to the KdV equation (that is, $\zeta = 0$) when there is a spectral gap in $c > 0$ and steady solitary waves can bifurcate from $k = 0$. This heuristic argument was confirmed with rigorous proofs, see Galkin and Stepanyants [28], Grimshaw and Helfrich [31].

A KdV solitary wave with initial amplitude a is extinguished in a finite time due to the radiation of inertia-gravity waves, Grimshaw et al. [33], and the extinction

time is given by

$$s_e = \frac{1}{\zeta}(\frac{a\nu}{12})^{1/2}\,, \tag{3.5}$$

Later Grimshaw and Helfrich [39] showed that this initial KdV solitary wave is replaced by an envelope wave packet steadily propagating with a speed close to the maximum group velocity, and with the associated carrier wave number. This was confirmed experimentally, see Grimshaw and Helfrich [31], and in further numerical simulations, see for instance Grimshaw et al. [45]. These results are all for the constant-coefficient Ostrovsky equation, but recently Grimshaw et al. [44] examined the combined effect of topography and rotation using a variable-coefficient Ostrovsky equation. They showed that again there is an extinction time similar to (3.5), but their simulations of a South China Sea transect, using both a variable-coefficient Ostrovsky equation and an ocean circulation model, were not long enough to see total extinction. Helfrich [51] examined the effects of rotation in numerical simulations of a two-layer fluid using a fully nonlinear, weakly nonhydrostatic model, and found that due to the rotation, an initial KdV-type solitary wave decays into inertia-gravity waves, which then steepens due to nonlinearity, leading to a secondary solitary wave at the expense of the parent wave, and this new solitary wave then experiences a similar decay. The decay and re-emergence process repeats and eventually a nearly localised wave packet emerges. A similar cycle of decay and recurrence was seen in the numerical simulations of the Ostrovsky equation (Grimshaw et al. [33]), but these early simulations were not carried out for a long enough time to see the emerging wave packet.

3.2 Undular bore asymptotic theory

In this section, the well-known theory for a KdV undular bore is re-examined. In the absence of rotation (that is $\zeta = 0$), the Ostrovsky equation (3.1) reduces to the

KdV equation, and for a constant nonlinear coefficient ν, this has the well-known periodic travelling wave solution, the cnoidal wave,

$$U = a\left\{b(m) + \mathrm{cn}^2(\varkappa\theta; m)\right\} + d\,, \quad \theta = k(X - vs)\,, \tag{3.6}$$

$$\text{where} \quad \nu a = 12m\varkappa^2k^2\,, \quad b(m) = \frac{1-m}{m} - \frac{E(m)}{mF(m)}\,, \tag{3.7}$$

$$v - \nu d = \frac{\nu a}{3}\left\{\frac{2-m}{m} - \frac{3E(m)}{mF(m)}\right\} = 4\varkappa^2k^2\left\{2 - m - \frac{3E(m)}{F(m)}\right\}\,. \tag{3.8}$$

Here cn is the Jacobi cosine elliptic function of modulus m $(0 < m < 1)$, v is the wave speed in the transformed space and $F(m), E(m)$ are the elliptic integrals of the first and second kind respectively, defined by

$$\mathrm{cn}(\vartheta; m) = \cos(\chi)\,, \quad \vartheta = \int_0^\chi \frac{d\chi'}{(1 - m\sin^2\chi')^{1/2}}\,, \quad 0 \le \chi \le \frac{\pi}{2}\,, \tag{3.9}$$

$$F(m) = \int_0^{\pi/2} \frac{d\chi}{(1 - m\sin^2\chi)^{1/2}}\,, \quad E(m) = \int_0^{\pi/2} (1 - m\sin^2\chi)^{1/2}\, d\chi\,. \tag{3.10}$$

The cnoidal wave $U(\theta)$ (3.6) is periodic both spatially and temporally, manifested by requiring that it be periodic in θ with a period of 2π. Then the wavenumber $\varkappa = F(m)/\pi$, while the spatial period is $2\pi/k$. The (trough-to-crest) amplitude is a and the mean value of U over one period is d. This solution family has three independent parameters, say k, m, d. There are two important limiting cases. One is when the modulus $m \to 1$, and then this becomes a solitary wave train, since then $b \to 0$ and $\mathrm{cn}(\vartheta) \to \mathrm{sech}(\vartheta)$, while $\varkappa \to \infty$, $k \to 0$ with $\varkappa k = \varpi$ fixed. The other case is when $m \to 0$, $b \to -1/2$, $\varkappa \to 1/2$, $\mathrm{cn}(\vartheta) \to \cos(\vartheta)$, and it reduces to a sinusoidal wave $(a/2)\cos(\theta)$ of small amplitude $a \sim m$ and wavenumber k.

Whitham modulation theory can now be used to construct an undular bore by allowing this cnoidal wave to vary slowly with s, X, that is the wavenumber k, modulus m and mean level d vary slowly with s, X. The Whitham modulation

equations describing this variation can be obtained by averaging conservation laws, see Whitham [109, 110], or by exploiting the integrability of the constant-coefficient KdV equation, see Kamchatnov [60] for example. When the nonlinear coefficient ν in (3.1) is a constant, we note especially a similarity solution of the Whitham modulation equations which describes an undular bore evolving from an initial step of height U_0 where $\nu U_0 > 0$, see Whitham [109], Gurevich and Pitayevsky [50],

$$\frac{X}{s} = \frac{\nu U_0}{3}\left\{1 + m - \frac{2m(1-m)F(m)}{E(m) - (1-m)F(m)}\right\}, \quad -\nu U_0 < \frac{X}{s} < \frac{2\nu U_0}{3}, \tag{3.11}$$

$$a = 2U_0 m\,, \quad d = U_0\left\{m - 1 + \frac{2E(m)}{F(m)}\right\}, \quad \nu U_0 = 6\varkappa^2 k^2\,, \quad v = \frac{\nu U_0}{3}\{1+m\}\,. \tag{3.12}$$

Note that

$$X - vs = \frac{\nu U_0 s}{3}\left\{-\frac{2m(1-m)F(m)}{E(m) - (1-m)F(m)}\right\} \tag{3.13}$$

is negative for all X, s. This describes a wave train connecting a zero level at the front where $m \to 1$ to a mean level U_0 at the rear where $m \to 0$. At the front the leading wave is a solitary wave of amplitude $2U_0$, while at the rear the waves are linear sinusoidal waves with a very small amplitude, and some intermediate waves whose nonlinearity (indicated by m) is decreasing from the front to rear exist between these two edges. Note that with the evolution, the whole undular bore is expanding with "time" s, but nevertheless it is always confined in a range $-\nu U_0 s < X < 2\nu U_0 s/3$.

Following El et al. [25], Grimshaw and Yuan [32] it is now useful to examine the solitary wave train at the leading edge of the undular bore, formally obtained by taking the limit $m \to 1$. In this limit, the three Whitham modulation equations uncouple and can be explicitly solved. Then it is found that the deformation of a solitary wave train in a non-rotating variable medium $\nu = \nu(s), \zeta = 0$ can be classified into two scenarios, depending on whether there is a polarity change, that is ν changes sign, or not. Each of these are now well understood, see the reviews in Grimshaw

[37], Grimshaw et al. [43]. The outcome for a solitary wave train is that the amplitude a of the leading wave in the solitary wave train varies according to the law $a^3 \propto \nu$, while the amplitudes in the solitary wave train, relative to this adiabatic deformation, have a similarity structure proportional to X/s. This scenario holds provided $\nu \neq 0$. Nevertheless in the case with a change of polarity, that is there is a critical point where ν passes through zero and changes sign, after passing through the critical point a rarefaction wave with a similar structure and of opposite polarity to the solitary waves emerges, terminated by an undular bore. For an undular bore, these descriptions can be applied to the leading solitary wave train in an undular bore, but a full description using Whitham modulation theory in a variable medium cannot be obtained, due to the development of non-adiabatic behaviour in the region between the quasi-periodic undular bore wave train, and the solitary wave train emitted ahead of this structure, see El et al. [25]. Taking rotation into account as well would seem to be beyond current theoretical capacity, but we note that Whitfield and Johnson [108] derived the Whitham modulation equations for the Ostrovsky equation, albeit for constant coefficients and in the weak rotation limit (two orders smaller).

3.3 Initial conditions

As the goal of this chapter is to detect the underlying dynamics of internal undular bores propagating over a variable bottom topography under the influence of rotation, it is sufficient to use an idealised process model. Hence, we choose the nonlinear coefficient $\nu = \nu(s)$ as a function of s only varying monotonically from $\nu = 1$ at $s = 0$ to some constant value $\nu = \nu_a$ for $s \geq s_a$. Specifically,

$$\nu = 1 + (\nu_a - 1) \tanh(Ks), \tag{3.14}$$

where $K, s_a, Ks_a \gg 1$ are chosen so that ν varies smoothly and slowly from 1 at $s = 0$ to ν_a at $s = s_a$. There are two main scenarios, either $\nu_a > 0$ for propagation up a slope, or $\nu_a < 0$ for propagation up a slope and through a point of polarity change. Likewise, the rotation coefficient $\zeta = \zeta(s)$ should be chosen to be initially quite small, $\zeta = 0.5$ here, corresponding to strong dispersion in deep water, and then increase to a constant value $\zeta_a > 0.5$, corresponding to propagation up a slope. A suitable choice is

$$\zeta = 0.5 + (\zeta_a - 0.5)\tanh(Ks)\,, \tag{3.15}$$

so that ζ increases from 0.5 to a constant value ζ_a for $s \geq s_a$.

The initial condition is $U(X, s = 0) = U_{ic}(X) + D(X)$ where $D(X)$ (expression below) is a pedestal needed to ensure that the mass constraint, see equation (2.21) in Chapter 2, is satisfied at the initial value $s = 0$ and $U_{ic}(X)$ is either (1) a KdV solitary wave, or (2) a box of height $U_0 > 0$ which in the absence of rotation and variable topography would generate an undular bore followed by a rarefaction wave, or (3) a modulated cnoidal wave representation of an undular bore in the constant coefficient KdV equation evolving from a step of height $U_0 > 0$ at time $s = -s_1$, given by (3.11 - 3.13) with s replaced by $(s + s_1)$ and then evaluated at $s = 0$ when $\nu = 1$,

$$(1) : U_{ic}(X) = a\,\mathrm{sech}^2(\varkappa X)\,, \quad a = 12\varkappa^2\,, \tag{3.16}$$

$$\begin{aligned}
&(2) : U_{ic}(X) = U_0\,\mathrm{ENV}(X)\,,\\
&\mathrm{ENV}(X) = \frac{1}{2}\{\tanh\Gamma(X + L) - \tanh\Gamma(X - L)\}\,,
\end{aligned} \tag{3.17}$$

$$\begin{aligned}
&(3) : U_{ic}(X) = U_0\,\mathrm{ENV}(X)\{2m\mathrm{cn}^2(\varkappa(X - vs_1); m) + 1 - m\}\,,\\
&-U_0 s_1 < X < \frac{2U_0 s_1}{3}\,, \quad U_0 = 6\varkappa^2 k^2\,, \quad v = \frac{U_0}{3}\{1 + m\}\,,\\
&X = \frac{U_0 s_1}{3}\left\{1 + m - \frac{2m(1-m)K(m)}{E(m) - (1-m)K(m)}\right\}\,.
\end{aligned} \tag{3.18}$$

In case (1) the evolving solitary wave has a time scale of $(\varkappa V)^{-1}$ where the speed $V = 4\varkappa^2$, and so to be slowly varying we choose $K \ll \varkappa V = 4\varkappa^3$ in expression (3.14) and (3.15). In case (2) the envelope ENV(X) is chosen to be very close to a box of height 1, and of very long length $2L$, that is to say $K^{-1} \ll 1 \ll 2L$. With a constant $\nu = 1$ and $U_0 > 0$ in the KdV regime, the front end of the box is then expected to generate an undular bore in the subsequent evolution. Since the leading wave in the undular bore is a solitary wave of amplitude $2U_0$, so again K should be small enough to warrant $K \ll 4\varkappa^3$, where here $U_0 = 6\varkappa^2$. At the same time, the rear end of the box will generate a rarefaction wave, and some model time later, the calculation will be cut off and the matured undular bore is now ready to be put into the Ostrovsky equation. In case (3) the asymptotic solution is similar to the undular bore generated in case (2), but we can now control the parameters more effectively. The initial undular bore at $s = 0$ occupies the domain $-U_0 s_1 < X < 2U_0 s_1/3$. We choose s_1 to make sure this domain has length $L_{ub} = 5U_0 s_1/3 \gg 1$. The envelope ENV$(X)$ has a similar structure as that in case (2), but a constraint is put on, that is the front end of the box is placed precisely at the front end of the undular bore $X = 2U_0 s_1/3$, while the rear end is chosen far away from the rear end of the bore, which means the initial undular bore is contained in the box with $L > L_{ub}$. Analogous to case (2), the leading wave is a solitary wave of amplitude $2U_0$ and thus again K should be small, $K \ll 4\varkappa^3$ where here $U_0 = 6\varkappa^2 k^2$. Note that the wavelength $2\pi/k$ is a free parameter. The pedestal $D(X)$ is represented in these three respective cases as

$$(1): \qquad \int_{-\infty}^{\infty} D(X)\,dX = -\int_{-\infty}^{\infty} a\,\mathrm{sech}^2(\varkappa X)\,dX = -\frac{2a}{\varkappa} = -24\varkappa\,, \tag{3.19}$$

$$(2): \qquad \int_{-\infty}^{\infty} D(X)\,dX = -a\int_{-\infty}^{\infty} \mathrm{ENV}(X)\,dX = -2aL\,, \tag{3.20}$$

$$(3): \qquad \int_{-\infty}^{\infty} D(X)\,dX \approx -aL\,, \tag{3.21}$$

such that the initial mass is zero. In case (3) we have estimated the integral as approximately half that of case (2) since the initial step is located at the halfway point of the envelope ENV(X). For a numerical domain of total length $2L_n$, a simple choice is (1) $D = -12\varkappa/L_n$, (2) $D = -L/L_n$ and (3) $D = -0.5L/L_n$. However a better choice to avoid end effects is

$$D(X) = \frac{D_0}{2}\left\{\tanh\left(\frac{X+L_e}{L_w}\right) - \tanh\left(\frac{X-L_e}{L_w}\right)\right\}, \quad \int_{-\infty}^{\infty} D(X)\,dX = 2D_0L_e\,, \tag{3.22}$$

where $L_e = L_n/2, L_w = L_n/4$. To keep the pedestal small, we need $|D_0| \ll a$, or $D_0 \ll U_0$, that is, $\varkappa L_e \gg 1$ or $L_e \gg L$.

3.4 Numerical results

First we examine the evolution of an initial KdV solitary wave, case (1), the same as that considered in Grimshaw and Helfrich [39] for a constant environment, but now for a variable medium with $\nu = \nu(s)$ and $\zeta = \zeta(s)$. The outcome is shown in figure 3.2 and we see that the outcome is quite similar to the constant-coefficient case of Grimshaw and Helfrich [39]. Eventually the initial solitary wave is replaced by a wave packet followed by trailing waves. The rotational effect appears to be dominant in this circumstance, with the nonlinear effect partly suppressed, as the variation of the nonlinear coefficient ν, specifically the occurrence of a polarity change or not, does not seem to make much impact on the subsequent evolution. Moreover in both cases (see the middle and right panels) the amplitude of the resultant wave packet is almost the same, although when $\nu_a = -1$ (polarity change), the envelope tends to lie below the zero level more than when $\nu_a = 0.2$ (no polarity change), which indicates some small influence of nonlinearity. We recall that in the KdV regime, see Grimshaw [37], Grimshaw and Yuan [32], Grimshaw et al. [43], when there is no polarity change (ν changes from 1 to 0.2), then to conserve the wave action flux, the

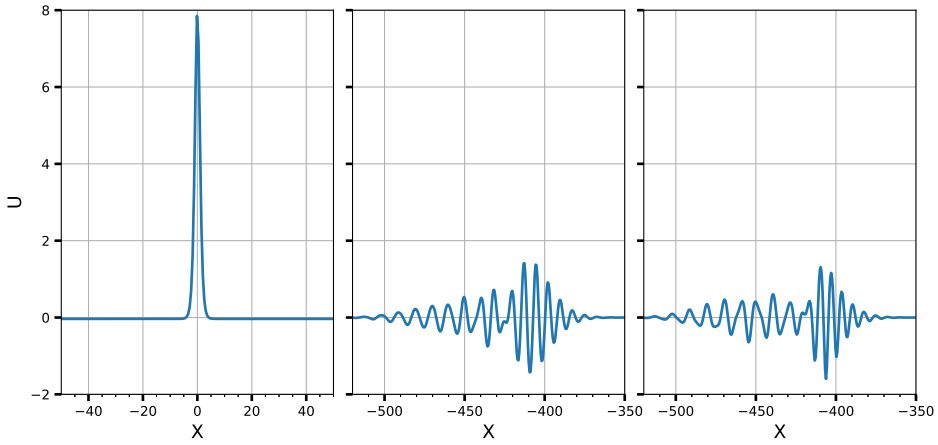

Figure 3.2: A simulation of the Ostrovsky equation (3.1) for the internal solitary wave initial condition (3.16). The left panel is at $s = 0$ with $a = 8$ when $\nu = 1$ and $\zeta = 0.5$; the middle panel is the case without a polarity change at $s_a = 100$ when $\nu_a = 0.2$ and $\zeta_a = 1.5$; the right panel is for the case of polarity change, at $s_a = 100$ when $\nu_a = -1$ and $\zeta_a = 1.5$. In both cases, $K = 0.05$ in (3.14) and (3.15), so that $Ks_a = 5$.

adiabatic law shows that the amplitude of the leading solitary wave a behaves as $a \propto \nu^{1/3}$, but at the same time, conservation of mass results in a trailing shelf which has an amplitude at the solitary wave location proportional to $\nu^{-8/3}\nu_s$ (normally it is approximately one order smaller than $\nu^{1/3}$). In contrast, the situation is different in the case with a polarity change, where the leading solitary wave and the trailing shelf have comparable amplitudes near the critical point where $\nu = 0$, and normally they both are smaller than their counterparts without a polarity change. Hence, in the Ostrovsky equation, the combined effect of rotation and nonlinearity is exerted over the solitary wave, and one of the expected evolution scenarios is that when $\nu_a = 0.2$, the outcome is characterised by a larger amplitude of the envelope and a smaller number of waves contained in the trailing shelf, in contrast to the case with $\nu_a = -1$. Note that here the extinction time s_e (3.5) is of order unity. Since the the model run-time is $s_a = 100$, then $s_e \sim 1$ is relatively too short to take the variation of the nonlinear term into account, and hence leads to the dominant rotational effect.

The initial internal undular bore is generated for convenience from the evolution

of a long box (3.17) in the framework of KdV equation, see figure 3.3. Moreover, in the full Euler equations, this initial box can also be used to generate an undular bore (not shown here). This resultant undular bore can be theoretically described by the modulated cnoidal wave (3.18). The behaviour of undular bores propagating over a variable topography was studied in El et al. [25] in a water wave context and Grimshaw and Yuan [32] in a variable-coefficient KdV model. The effect of the slowly varying topography is the generation of a solitary wave train ahead of the main undular bore, and these two parts are connected where the rear of the solitary wave train interacts with the main undular bore, forming a two-phase modulated wave train. When there is a polarity change, on passage through the critical point (nonlinear coeffcient $\nu = 0$), the leading solitary wave train in the undular bore is not able to retain its shape and is gradually replaced by developing rarefaction waves supporting emerging solitary waves of the opposite polarity, while the rear near-linear periodic waves hold their shapes, but when a rotational effect is jointly taken into account, the outcome becomes more complicated, see figures 3.3-3.5. In general the internal undular bore decays into several wave packets, accompanied by a few residual waves. More specifically and heuristically, the leading nonlinear waves behave like solitary waves, as shown in figure 3.2, but note that then this is followed by inevitable complicated interactions between the radiated inertial-gravity waves and also with the original rear periodic waves, some of which form wave packets propagating coherently. Eventually, some nearly localized wave packets emerge, each one consisting of a long-wave envelope through which shorter, faster waves propagate. Furthermore, depending on the parameter s_1 in the initial condition, which determines the number of waves contained in the initial bore, a different number of wave packets finally appear after long-time evolution. It seems that the more waves there are in the initial bore, then more wave packets are formed, see figure 3.4 and 3.5 (cf. figure 3.3). Unlike the aforementioned cases of a solitary wave, for an undular bore,

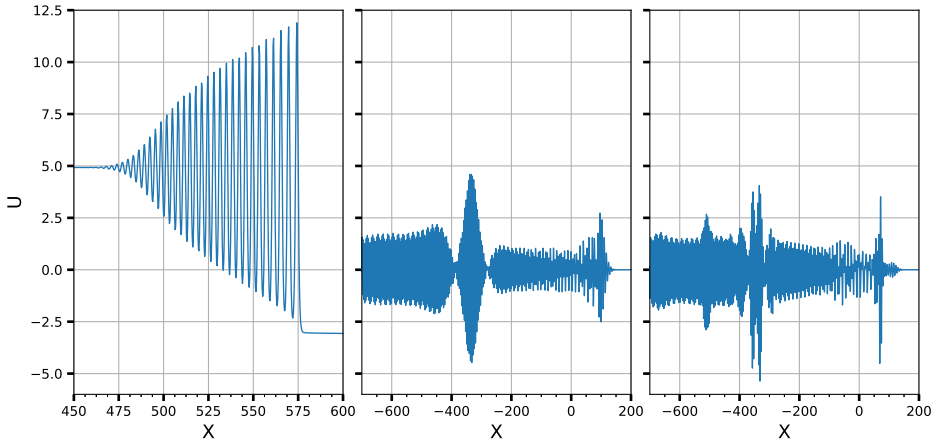

Figure 3.3: A simulation of the Ostrovsky equation (3.1) for the box initial condition (3.17). The left panel is the matured undular bore developed in the KdV equation with a constant coefficient $\nu = 1$ starting from the initial box with $U_0 = 8$ for a run-time duration $s = 20$. Then afterwards, this undular bore is used as the input to the Ostrovsky equation in which a combined effect of varying rotation and nonlinearity is considered, as given in (3.14) and (3.15). The middle panel is at $s_a = 120$ (the origin $s = 0$ of time domain is reset in the Ostrovsky equation) when $\nu_a = 0.2$ and $\zeta_a = 1.5$; the right panel is for the case of polarity change, at $s_a = 120$ when $\nu_a = -1$ and $\zeta_a = 1.5$. In both cases, $K = 0.03$ in (3.14) and (3.15), so that $Ks_a = 3.6$.

the variation of the nonlinear effect plays a crucial role in the evolution. Comparing the cases of $\nu_a = 0.2$ with that of $\nu_a = -1$ in figures 3.3-3.5, it is clear that the value of ν_a can influence the formation of the eventual wave packets to some finite degree. First, when $\nu_a = -1$, the amplitude of the wave envelope, is larger than that when $\nu_a = 0.2$, and also it tends to lie further below the zero level, which can be partially attributed to the nonlinear steepening. The number of wave packets eventually formed and the length scale of each wave packet are related to nonlinear effects, that is, there are more wave packets but each with a shorter length scale when $\nu_a = -1$ than when $\nu_a = 0.2$.

3.5 Discussion and Conclusion

Our focus in this chapter is how an internal undular bore behaves in a long-time limit when the combined effect of topography and background rotation are both taken

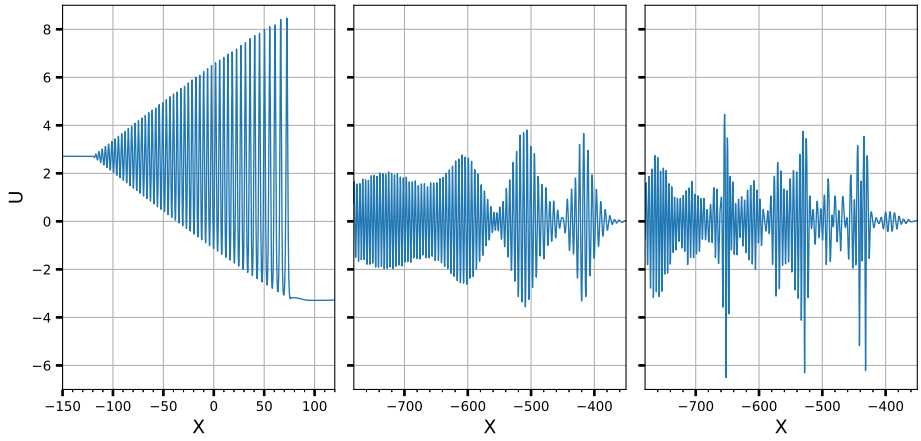

Figure 3.4: A simulation of the Ostrovsky equation (3.1) for the initial condition (3.18). The left panel is at $s = 0$ with $U_0 = 6$, $s_1 = 20$ and wavenumber $k = 1$ when $\nu = 1$ and $\zeta = 0.5$; the middle panel is the case without a polarity change at $s_a = 120$ when $\nu_a = 0.2$ and $\zeta_a = 1.5$; the right panel is for the case of polarity change, at $s_a = 120$ when $\nu_a = -1$ and $\zeta_a = 1.5$. In both cases, $K = 0.03$ in (3.14) and (3.15), so that $Ks_a = 3.6$.

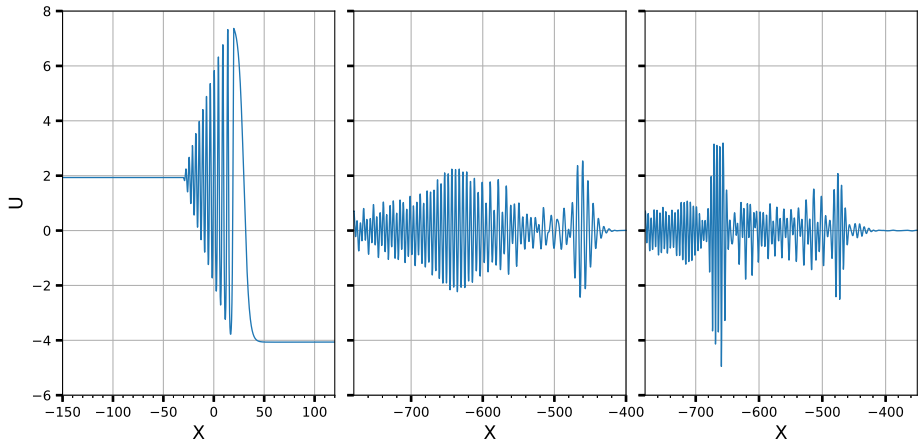

Figure 3.5: The same as in figure 3.4, apart from that $s_1 = 5$.

into account. Since the leading part of an undular bore is composed of a solitary wave train, an initial condition consisting of a single solitary wave is first examined. As found in previous studies, such as Grimshaw and Helfrich [39, 31], due to the rotation, the initial solitary wave decays through the generation of inertia-gravity waves and is completely extinguished on a time scale of $s_e = \sqrt{a\nu/12}/\zeta$. In our long-time model simulation, eventually a coherent envelope wave packet emerges to replace the initial wave. Compared with the set-up of a constant environment in Grimshaw and Helfrich [39, 31], here we consider a variable background environment to simulate internal waves propagating shorewards. We find that the rotational effect is dominant, while nonlinear effects slightly modulate the waveform and amplitude. We note that Grimshaw et al. [44] investigated a similar problem, where they applied the variable-coefficient Ostrovsky equation to a transect in the South China Sea. They showed that the combined effect of shoaling and rotation is to induce a secondary trailing wave packet. Because their model-run time was not very long, the difference with our presented results can be attributed to our much longer model run-time, as here the extinction time $s_e \sim 1$, while we run the model for $s_a = 100 \gg s_e$.

If only the topographic effect is considered, that is the rotational coefficient $\zeta = 0$ in equation (3.1), then depending on whether the waves pass through a critical point (the nonlinear coefficient $\nu = 0$) or not, the evolution scenarios of an undular bore can be quite different. This is examined in our joint paper Grimshaw and Yuan [32]. The main outcome of that paper is in the numerical simulation shown in figure 3.6 (c.f. figure 3.7) where the parameters have been chosen to be typical of those which might occur in the coastal ocean. The front of the undular bore is a depression solitary wave whose amplitude decreases as the critical point is approached and emerges after the critical point as a depression rarefaction wave with several elevation solitary waves emerging from this pedestal. The rear of the undular bore retains its shape, but the wave amplitude decreases and the bore moves more slowly. The deformation of the

undular bore is a non-adiabatic process due mainly to the inconsistency between the preservation of the jump and hence the leading solitary wave amplitude if it were adiabatic, and the adiabatic change in the amplitude of a solitary wave as ν varies, see El et al. [25]. In the case studied by El et al. [25], $|\nu|$ increased, and consequently the solitary waves at the front of the undular bore grow in amplitude and are emitted ahead of the undular bore as a solitary wave train; the rear of this solitary wave train interacts with the undular bore forming a two-phase wave interaction region. In contrast, here $|\nu|$ initially decreases, as shown in figure 3.6, and so the solitary waves at the front of the undular bore are immediately absorbed into the undular bore in a two-phase interaction region. But after passage through the critical point, $|\nu|$ increases, and the leading solitary waves move ahead but are now riding on a negative pedestal which has the form of depression rarefaction wave.

When the rotational effect is also included, the evolution of inertia-gravity waves, resulting in complicated interactions between these radiated waves, and with the rear part of the undular bore, while at the front of the undular bore a few envelope wave packets form and propagate coherently. The nonlinear effects can influence the eventual emergence of these wave packets, manifested by a larger envelope amplitude, more wave packets and a shorter envelope length scale when there is a passage through the critical point ($\nu_a = -1$) than when there is no polarity change ($\nu_a = 0.2$).

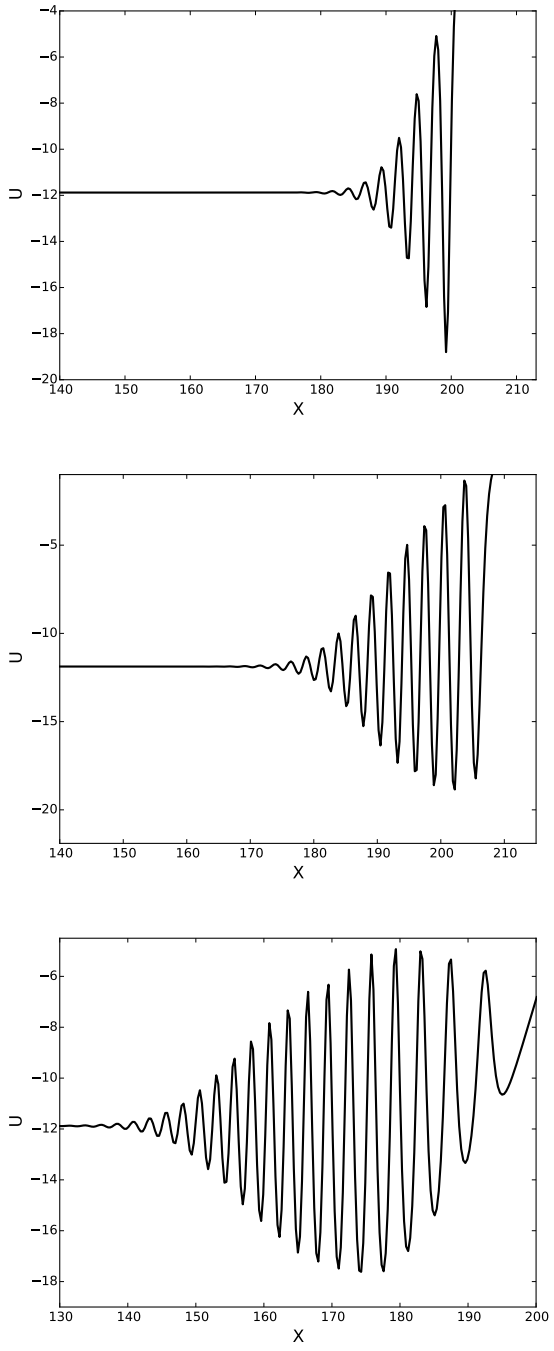

Figure 3.6: A simulation of the variable-coefficient KdV equation, that is $\zeta = 0$ in equation (3.1), when ν varies from -1 to 1 as specified by (3.14) for the undular bore initial condition (3.17) with $U_0 = -12$; the top panel is at $\nu = -1$, the middle panel is at $\nu = 0$ and the bottom panel is at $\nu = 1$. Note the slight variation in the horizontal and vertical axes.

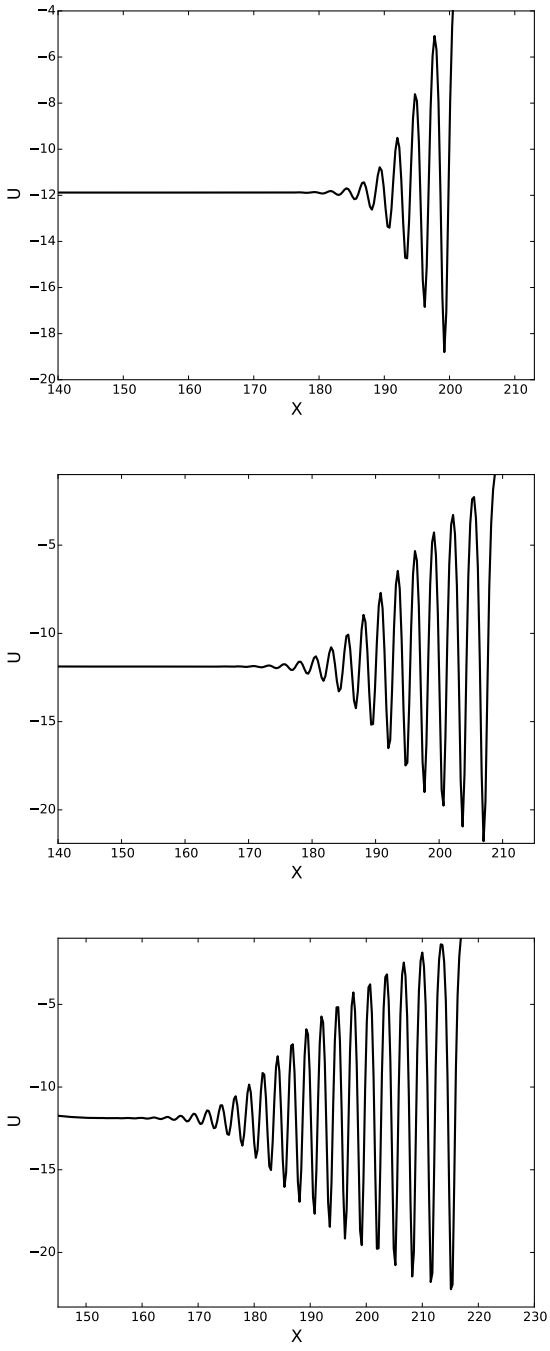

Figure 3.7: A simulation of the KdV equation, that is $\zeta = 0$ in equation (3.1), when $\nu = -1$ is constant, for the undular bore initial condition (3.17) with $U_0 = -12$; the top panel, middle panel and the bottom panel are at the same times as the corresponding panels in figure 3.6. Note the slight variation in the horizontal and vertical axes.

Chapter 4

The evolution of second mode internal solitary waves over variable topography

In this chapter, a study of the propagation of a mode-2 internal solitary wave over a slope-shelf topography is presented. The methodology is based on a variable-coefficient KdV (vKdV) equation, using both analysis and numerical simulations, and simulations using the MIT general circulation model (MITgcm). Following equation (2.18) in Chapter 2, the vKdV equation in physical space is

$$A_t + cA_x + \alpha AA_x + \beta A_{xxx} = 0\,, \tag{4.1}$$

then after a series of transformation (2.14)-(2.19), it is written in the transformed space as

$$U_s + \nu UU_X + U_{XXX} = 0\,. \tag{4.2}$$

4.1 Mode decomposition technique

Taking the Boussinesq and rigid lid approximations, commonly used in oceanography, and as we then assume here, in the absence of a background current $u_0 = 0$, the modal equation (2.3) and boundary conditions (2.4) in Chapter 2 reduce to

$$c^2\phi_{zz} + N^2\phi = 0 \quad \text{for} \quad -h < z < 0\,, \tag{4.3}$$

$$\phi = 0 \quad \text{at} \quad z = -h, 0\,. \tag{4.4}$$

As a result, the expressions for α, β (equations (2.5) and (2.6)) reduce to

$$I\,\alpha = 3\int_{-h}^{0} c^2\phi_z^3\,dz\,, \tag{4.5}$$

$$I\,\beta = \int_{-h}^{0} c^2\phi^2\,dz\,, \tag{4.6}$$

$$I = 2\int_{-h}^{0} c\,\phi_z^2\,dz\,. \tag{4.7}$$

Since we will be projecting the output from the MITgcm onto the complete set of vertical modes, it is now necessary to outline how this will be achieved. In general the modal system (4.3, 4.4) defines an infinite set of internal modes $\phi_n, n = 1, 2, 3, \ldots$ and speeds c_n, where $c_1 > c_2 > \cdots$. Mode-1 has $n = 1$ with no internal zeros and mode-2 has $n = 2$ with just one internal zero. These modes are complete and orthogonal with respect to the weight function N^2, that is

$$\int_{-h}^{0} N^2\phi_n\,\phi_m\,dz = S_n\delta_{nm}\,, \quad S_n = \int_{-h}^{0} N^2\phi_n^2\,dz\,, \tag{4.8}$$

where the subscript n and m represent mode number, and δ_{nm} is the Kronecker delta. Using (4.3, 4.4), we can further obtain

$$S_n = c_n^2 \int_{-h}^{0} \left(\frac{\partial \phi_n}{\partial z} \right)^2 dz \,, \tag{4.9}$$

and an equivalent orthogonality condition,

$$c_n^2 \int_{-h}^{0} \frac{\partial \phi_n}{\partial z} \frac{\partial \phi_m}{\partial z} \, dz = S_n \delta_{nm} \,. \tag{4.10}$$

The vertical particle displacement $\varsigma(x, z, t)$ can be projected onto these modes,

$$\varsigma(x, z, t) = \sum_{1}^{\infty} \varphi_n(x, t) \phi_n(z; x) \,, \tag{4.11}$$

where $\varphi_n(x, t)$ is the amplitude of mode n. Note that once a mode has been selected, φ_n is just its amplitude in the vKdV equation. Then we have

$$\int_{-h}^{0} N^2 \varsigma \phi_n \, dz = \varphi_n S_n \,. \tag{4.12}$$

This can also usefully be written in an alternative form

$$c_n^2 \int_{-h}^{0} \frac{\partial \phi_n}{\partial z} \frac{\partial \varsigma}{\partial z} \, dz = \varphi_n S_n \,. \tag{4.13}$$

When using the MITgcm, one of the outputs readily available is the velocity field (u, w). To find an expression for ς, and noting that taking a z-derivative is not convenient, possibly introducing new errors, we proceed as follows. In the linear long wave approximation

$$\varsigma_t \approx w \,, \tag{4.14}$$

which can be combined with the conservation of mass equation

$$u_x + w_z = 0\,, \tag{4.15}$$

to yield

$$u_x \approx -\varsigma_{tz}\,. \tag{4.16}$$

Then, also noting that to the leading linear long wave order, for each mode n, the vertical displacement ς_n has

$$\frac{\partial \varsigma_n}{\partial t} + c_n \frac{\partial \varsigma_n}{\partial x} \approx 0\,, \tag{4.17}$$

the final approximate expression for φ_n is

$$\varphi_n S_n \approx c_n \int_{-h}^{0} u \frac{\partial \phi_n}{\partial z}\, dz\,. \tag{4.18}$$

With the aid of this mode decomposition technique (4.18), the amplitude φ_n of each mode can be easily obtained from the output of the MITgcm. Futher the energy budget of each can also be obtained. Confining attention to linear long wave theory, the domain-integrated available potential energy (APE) in each mode is

$$P_n = \int\int \frac{1}{2}\rho_0 N^2 \varsigma_n^2\, dxdz\,. \tag{4.19}$$

Again invoking the Boussinesq approximation, and also considering (4.8, 4.9, 4.11), this can be rewritten in an alternative and more convenient form,

$$P_n = J_n \int \varphi_n^2\, dx\,, \quad J_n = \frac{c_n^2}{2} \int_{-h}^{0} \rho_0 \left(\frac{\partial \phi_n}{\partial z}\right)^2 dz\,. \tag{4.20}$$

Note that the modal functions ϕ_n and speed c_n also contain a slow x-dependence, but that is suppressed here at the leading order. In the same slowly-varying environment,

the velocities in each internal wave mode can be obtained as follows,

$$u_n(x,z,t) = c_n \frac{\partial \phi_n(z)}{\partial z} \varphi_n(x,t)\,, \tag{4.21}$$

$$w_n(x,z,t) = -c_n \phi_n(z) \frac{\partial \varphi_n(x,t)}{\partial x}\,. \tag{4.22}$$

Then the domain-integrated kinetic energy (KE) in each mode is

$$K_n = \int\int \frac{1}{2}\rho_0(u_n^2 + w_n^2)\,dxdz \approx \int\int \frac{1}{2}\rho_0 u_n^2\,dxdz = J_n \int \varphi_n^2\,dx\,, \tag{4.23}$$

as in the long wave limit used here $w_n \ll u_n$. As expected, "equipartition of energy" holds here and the total energy can be found as $E_n = 2K_n = 2P_n$. Hence it is sufficient to calculate either K_n or P_n. Further, it is clear that due to the orthogonality of the modes the total kinetic energy and total potential energy are

$$K = \sum_n K_n\,, \quad P = \sum_n P_n\,. \tag{4.24}$$

4.2 Three-layer fluid system

It is well known that a three-layer fluid system is the simplest model that can support mode-2 waves. Indeed, three-layer density structures have been observed in the ocean, see Yang et al. [112] for instance. Hence a three-layer ocean model is used here to investigate the dynamics of mode-2 internal solitary waves. We assume that

$$\rho_0(z) = (\rho_2+\Delta\rho)\Theta(-z-h_1-h_2)+\rho_2\Theta(-z-h_1)\Theta(z+h_1+h_2)+(\rho_2-\Delta\rho)\Theta(z+h_1)\,, \tag{4.25}$$

where ρ_2 is the density of the middle layer, and the density difference $\Delta\rho > 0$; h_1, h_2 and h_3 are the thicknesses of the three layers from top to bottom respectively, and $\Theta(\cdot)$ is the Heaviside function. Note that with this piece-wise constant density

field only two of the infinite set of modes can be found, namely mode-1 and mode-2; the remaining modes are confined to the two interfaces, and cannot be found explicitly with this density profile, this amounts to considering the case of smooth density profile with interfaces of finite thickness, in the limit where the thickness tends to zero. In principle the densities of these three layers can take any reasonable values depending on the specific circumstances, but here to illustrate the dynamics, we choose one special case in which the density of the middle layer is exactly the mean value of that in the upper layer and bottom layer. From (4.3, 4.4) the modal function is given by

$$\begin{aligned}
&\phi = -A_1 \frac{z}{h_1}\,, \quad -h_1 \le z \le 0\,,\\
&\phi = A_1 \frac{z+h_1+h_2}{h_2} - A_2 \frac{z+h_1}{h_2}\,, \quad -h_1-h_2 < z < -h_1\,,\\
&\phi = A_2 \frac{z+h}{h_3}\,, \quad -h \le z \le -h_1-h_2\,.
\end{aligned} \tag{4.26}$$

Note that $\phi = A_1$ at the upper interface $z = -h_1$, and $\phi = A_2$ at the lower interface $z = -h_1 - h_2$. The solution is normalized by $\max[|\phi|] = 1$, so that $\max[|A_1|, |A_2|] = 1$, and without loss of generality, we require that $0 < A_1 \le 1$. The speed c is now found by noting that at $z = -h_1, -h_1 - h_2$, ϕ_z is discontinuous and ρ_{0z} consists of two δ-functions. Integrating the modal equation (4.3) across each interface leads to

$$c^2[\phi_z]^+_- + g'\,\phi = 0\,, \quad g' = g\frac{\Delta\rho}{\rho_2}\,, \tag{4.27}$$

where $[\cdot]^+_-$ is the difference between above and below each interface. Note that these jump conditions represent continuity of total pressure across each interface. Hence the speed c is found from the 2×2 eigenvalue problem,

$$\begin{aligned}
&c^2\{A_1(\frac{1}{h_1}+\frac{1}{h_2}) - \frac{A_2}{h_2}\} - g'A_1 = 0\,,\\
&c^2\{A_2(\frac{1}{h_2}+\frac{1}{h_3}) - \frac{A_1}{h_2}\} - g'A_2 = 0\,,
\end{aligned} \tag{4.28}$$

$$\frac{2g'}{c^2} = (\frac{1}{h_1} + \frac{2}{h_2} + \frac{1}{h_3}) \mp \{(\frac{1}{h_1} - \frac{1}{h_3})^2 + \frac{4}{h_2^2}\}^{1/2} . \tag{4.29}$$

The signs $\mp$ correspond to mode-1 and mode-2 respectively, so that, as expected $c_1 > c_2$. It then follows that

$$\frac{A_1}{A_2} = R = H \pm (H^2+1)^{1/2} , \quad \frac{A_2}{A_1} = \frac{1}{R} = -H \pm (H^2+1)^{1/2} , \quad H = \frac{h_2}{2}(\frac{1}{h_3} - \frac{1}{h_1}) . \tag{4.30}$$

Hence $R > 0 (< 0)$ for mode-1 and mode-2 respectively, so that, as expected, mode-1 has no internal zeros, and mode-2 has just one internal zero. Thus both the phase speed and internal zero criteria for distinguishing between mode-1 and mode-2 are valid here. Also, for mode-1, $R > 1 (< 1)$ according as $H > 0 (< 0)$, that is $h_1/h_3 > 1 (< 1)$, while for mode-2 $|R| < 1 (> 1)$ according as $H > 0 (< 0)$. Note that

$$\frac{g'h_2}{c^2} = \frac{h_2}{h_1} + 1 + H \mp (H^2+1)^{1/2} = \frac{h_2}{h_3} + 1 - H \mp (H^2+1)^{1/2} . \tag{4.31}$$

Then the coefficient α (4.5) is given by

$$I\alpha = 3c^2\{-\frac{A_1^3}{h_1^2} + \frac{A_2^3}{h_3^2} + \frac{(A_1-A_2)^3}{h_2^2}\} , \quad I = 2c\{\frac{A_1^2}{h_1} + \frac{A_2^2}{h_3} + \frac{(A_1-A_2)^2}{h_2}\} . \tag{4.32}$$

Substituting the expressions (4.30) into (4.32) we get that

$$\alpha = \frac{3cA_2}{2h_2}\frac{\Omega}{\Pi} , \quad \Omega = -\frac{h_2^2}{h_1^2}R^3 + \frac{h_2^2}{h_3^2} + (R-1)^3 , \quad \Pi = \frac{h_2}{h_1}R^2 + \frac{h_2}{h_3} + (R-1)^2 . \tag{4.33}$$

Our main concern is how these expressions vary as the lower layer depth h_3 decreases. Since for all the cases we consider, in the deep water $h_1 = h_3$, we can assume that $h_1 > h_3$ as the waves propagate up the slope. In this case $H > 0$, $R > 1$ for mode-1 and $-1 < R < 0$ for mode-2, so that recalling the convention that $A_1 > 0$, $A_1 = 1, 0 < A_2 < 1$ for mode-1, and $0 < A_1 < 1, A_2 = -1$ for mode-2. A useful

approximation is $h_2 \ll h_{1,3}$ when $H \to 0$ and so

$$\begin{aligned} &\text{mode-1}: \quad c^2 = 2g'h_1h_3/(h_1+h_3)\,, \quad A_1 = A_2 = 1\,, \quad \alpha = \frac{3c(h_1-h_3)}{2h_1h_3}\,, \\ &\text{mode-2}: \quad c^2 = g'h_2/2\,, \quad A_1 = -A_2 = 1\,, \quad \alpha = \frac{3c}{2h_2}\,. \end{aligned} \tag{4.34}$$

Another useful limit is $h_3 \to 0$ when $H \to +\infty$, and so

$$\begin{aligned} &\text{mode-1}: \quad c^2 = g'h_1h_2/(h_1+h_2)\,, \quad A_1 = 1\,,\, A_2 = 0\,, \quad \alpha = \frac{3c(h_1-h_2)}{2h_1h_2}\,, \\ &\text{mode-2}: \quad c^2 \approx g'h_3\,, \quad A_1 = 0\,,\, A_2 = -1\,, \quad \alpha = -\frac{3c}{2h_3}\,. \end{aligned} \tag{4.35}$$

Note that in the deep water, $h_1 = h_3$ as we assume, $H = 0$, $R = \pm 1$, $A_1 = A_2 = 1$ for mode-1, $A_1 = -A_2 = 1$ for mode-2, and

$$\begin{aligned} &\text{mode-1}: \quad c^2 = g'h_1\,, \quad \alpha = 0\,, \\ &\text{mode-2}: \quad c^2 = \frac{g'h_1h_2}{(2h_1+h_2)}\,, \quad \alpha = \frac{3c(2h_1-h_2)}{2h_1h_2}\,. \end{aligned} \tag{4.36}$$

These expressions show that for mode-1 $\alpha \geq 0$ when $h_1 \geq h_3$ in the limit $h_2 \ll h_{1,3}$, $\alpha \geq 0$ when $h_1 \geq h_2$ in the limit $h_3 \to 0$, and $\alpha = 0$ when $h_1 = h_3$. For mode-2, $\alpha > 0$ in the limit $h_2 \ll h_{1,3}$, while $\alpha < 0$ in the limit $h_3 \to 0$, but $\alpha \geq 0$ when $2h_1 \geq h_2$ for the case $h_1 = h_3$. In general the sign of α is determined by the sign of $A_2\Omega$, which is defined in equation (4.33), and in particular $\alpha = 0$ when

$$\frac{h_2}{h_1}(1-R^3) = -2H \pm \{4H^2R^3 + (1-R^3)(1-R)^3\}^{1/2}\,, \tag{4.37}$$

which defines the curves in the $h_2/h_1, h_2/h_3$ plane where $\alpha = 0$. Recalling that $h_1 > h_3$, $H > 0$, for mode-1 $R > 1$, the discriminant is positive and only the lower sign can be taken. In the limit $h_1 \to h_3$, this yields $h_2/h_1 \to 4/3$, so that there is a change of sign at this point just above the line $h_2/h_1 = h_2/h_3$. For mode-2, $-1 < R < 0$, the discriminant is positive only when H is large enough, and then

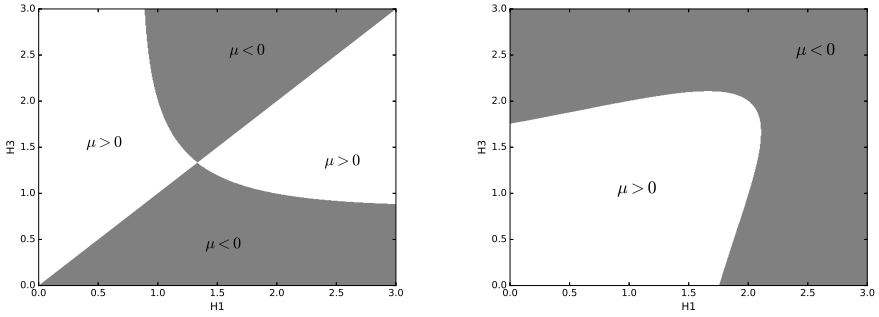

Figure 4.1: Plot of the nonlinear coefficient α (4.33) for mode-1 (left) and mode-2 (right). Shaded areas show negative value, $\mu < 0$. Labels are $H_1 = h_2/h_1, H_3 = h_2/h_3$.

the upper sign must be chosen. In the limit $h_1 \to h_3$, this yields $h_2/h_1 \to 2$. The outcome for the sign of α is shown in figure 4.1. In practice, h_1 and h_2 are constants, and so $H_1 = h_2/h_1$ is constant when the internal solitary wave propagates shoreward, while $H_3 = h_2/h_3$ is the only variable to change as h_3 changes. Hence we consider two cases: a polarity change and no polarity change, which will be shown in the next section.

4.3 From one three-layer system to another

We consider a three-layer system, in which the background current is zero and the density variations across each interface are the same, that is, the density is $\rho_2 - \Delta\rho$, ρ_2 and $\rho_2 + \Delta\rho$ respectively from top to bottom, where $\Delta\rho > 0$, exactly as listed in Section 4.2. Two configurations are investigated, both of which keep the thicknesses of the upper and middle layer as constants, that is, $h_1 = 200\,\mathrm{m}$ and $h_2 = 100\,\mathrm{m}$, and only the bottom layer h_3 varies as the waves move into shallow water. To model a realistic ocean situation, the idealised bathymetry used here has a typical slope-shelf structure, see figure 4.2. Initially in the deep water, the bottom layer $h_3 = 200\,\mathrm{m}$,

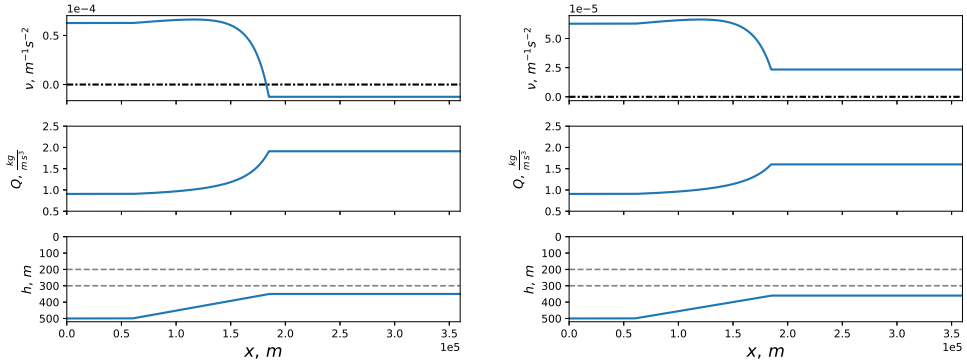

Figure 4.2: Coefficients of the vKdV equation (4.2) for mode-2, together with the corresponding bathymetry and density layers. Left panel is the EXP1, in which there is a polarity change ($h_3 = 50\,\mathrm{m}$ in the shallow water); right panel is the EXP2, in which there is no polarity change ($h_3 = 60\,\mathrm{m}$ in the shallow water). The dark dash-dotted line indicates where $\nu = 0$, while the grey dashed lines denote the two interfaces. Note that in the EXP1, the critical point ($\nu = 0$) locates at approximately $x = 1.8 \times 10^5\,\mathrm{m}$, just in the vicinity of the end of the slope at $x = 1.82 \times 10^5\,\mathrm{m}$.

then decreases along the linear-varying slope to $h_3 = 50\,\mathrm{m}$ (labelled as EXP1) or $h_3 = 60\,\mathrm{m}$ (labelled as EXP2) respectively onto the shelf. As a consequence, the thickness ratio $H_1 = h_2/h_1 = 0.5$ is a constant, while $H_3 = h_2/h_3$ adjusts from $H_3 = 0.5$ in the deep water to $H_3 = 2$ and $H_3 = 1.67$ respectively on the shelf. Although in these two cases EXP1 and EXP2, this 10 m thickness difference on the shelf may seem small, especially when compared with the total water depth (500 m), the corresponding dynamics can be completely distinguished from each other. When $h_3 = 50\,\mathrm{m}$ ($H_3 = 2$) on the shelf, referring to figure 4.1, the nonlinear coefficient α in equation (4.2) is negative, opposite from the positive value in the deep water, which indicates there must be a critical point on the slope, where $\alpha = 0$, and passing through that point, the initial convex wave ($\alpha > 0$) inverses its polarity and turns into a concave wave ($\alpha < 0$), that is, there is a polarity change. In contrast, the other case EXP2 is in a different regime, since α preserves its sign, $\alpha > 0$, so there is no polarity change.

The deformation scenarios of the EXP1 and EXP2 are depicted in figure 4.3. In the EXP1, a single convex wave with an initial amplitude of 18 m propagates

shoreward, and as expected, the evolution is adiabatic without significant change until it reaches the critical point. Prior to the critical point, the vKdV theory predicts that the amplitude decreases as $\alpha^{1/3}$ reduces, where α is the nonlinear coefficient in equation (4.2). Then, approaching the critical point, this slowly-varying solitary wave generates a trailing shelf of the opposite polarity, and this combination passes through the critical point. Thereafter as α becomes negative, this disturbance forms into a leading positive rarefaction wave at whose trailing edge an incipient jump is resolved by an undular bore whose leading component is a solitary wave train of negative polarity, see Grimshaw and Yuan [32]. The case with no polarity change EXP2 is distinct, as α decreases, the mass of the solitary wave increases as $\alpha^{-1/3}$, and this generates a negative trailing pedestal to conserve the total mass. But then instead of passing through a critical point, α approaches a constant value on the shelf, and hence the leading convex wave continues steadily, while new internal solitary waves of small amplitude and negative polarity form from the trailing pedestal.

Next, we compare these results to simulations using the MITgcm model. Our model domain and bathymetry are the same as those in the vKdV equation. The spatial steps are 1 m and 50 m in the vertical and horizontal direction respectively, and using a similar method to that introduced in Guo and Chen [47], two boundary layers, where the resolution exponentially decreases from 50 m to 2.5×10^5 m, are added at the ends of domain to suppress any reflections. In addition, considering the time scale of the waves, we set the time step to be 4 seconds. The background temperature is uniform in this model, 25°C, while the salinity is 5, 20 and 35 PSU respectively for the three layers. Neglecting the pressure deviation in the fluid, the corresponding densities can be achieved by the equation of state at atmospheric pressure with values of 1000.8, 1012.0 and 1023.3 $\mathrm{kg/m^3}$. In addition, to ensure that the model runs smoothly, we invoke a Leith Scheme, see Leith [71], to introduce some viscosity. The KdV-type mode-2 solitary wave is not an exact solution of the

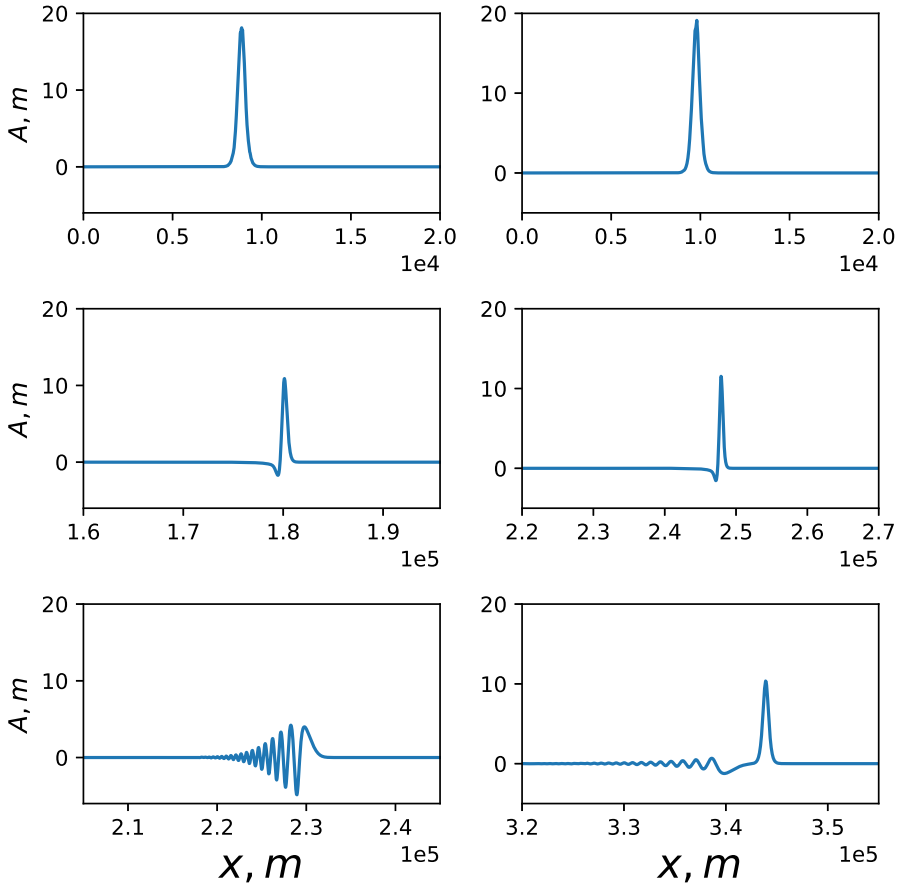

Figure 4.3: The amplitudes of the mode-2 internal solitary waves in simulations of the vKdV equation (4.2). Note that the results are transformed back to the physical space from the calculation space. Left panel is the EXP1, and the critical point is at approximately $x = 1.8 \times 10^5$ m; right panel is the EXP2. One point worth mentioning is that in order to emphasise the waveform, the horizontal scale changes, especially from the top to the middle panel.

Boussinesq equations solved by the MITgcm model, but nevertheless, essentially only some slight modulations are needed. Thus to obtain the initial wave, a preliminary MITgcm model run with the KdV wave as the initial condition is performed. As expected, the final usable stable incident mode-2 waves are followed by some small trailing waves.

Using the modal system (4.3, 4.4), it is found the fluctuation of the interface between the upper and middle layer in the MITgcm model is just the amplitude in the vKdV equation. Figure 4.4 shows a comparison between the vKdV and the MITgcm simulations. Here for brevity, only the result of the EXP1 is exhibited. Despite the fact that the amplitude of the MITgcm result is smaller than that from the vKdV equation, these two have good agreement. The MITgcm model solves the primitive equations, which can support solutions for all modes, including the mode-1 and mode-2 waves, while the vKdV equation by construction is not able to support mode-1 and mode-2 simultaneously. Hence, in the MITgcm simulations there is the possibility for the generation of mode-1 and higher modes, and energy exchange between modes, which is possibly the reason why a smaller amplitude occurs. In addition, viscosity and numerical wave breaking and turbulent mixing can be another sink for the energy. Indeed, as analysed in the following results for the energy budget, these may represent a large portion of the lost energy.

A mode decomposition technique, see equation (4.18) in section 4.1, is implemented on the MITgcm result, see figure 4.5. To be clear, snapshots of the MITgcm simulations are also shown in figure 4.6. As expected, the mode-2 wave decomposition behaves similarly to the evolution based on the vKdV equation (4.2), see figure 4.3. In deep water there is a very small mode-1 feature slaved to the main mode-2 wave, as the latter is not quite an exact mode-2 internal solitary wave as given by KdV theory. However after this mode-2 wave propagates onto the slope, this slaved feature grows into a mode-1 wave train, as energy flows from mode-2 into mode-1.

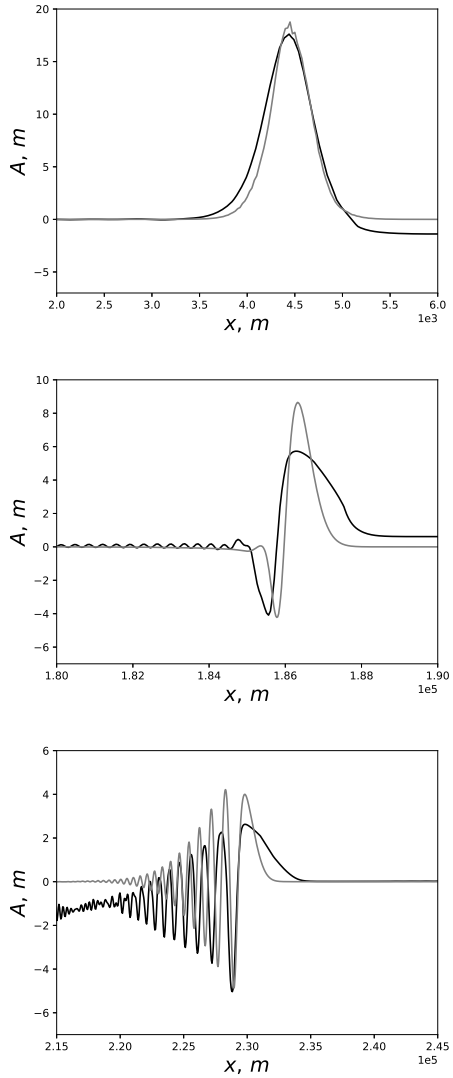

Figure 4.4: Three representative snapshots of the EXP1 at times $t = 0$, 22 and 30 hours (from top to bottom) in a three-layer to three-layer system are illustrated. The grey line is the result from the vKdV equation (4.2), but is transformed back to the physical space, while the dark line is the isopycnal line $\rho = \rho_2 - \Delta\rho = 1000.8\,\mathrm{kg/m^3}$, which is also the interface between the upper and middle layer, captured from the MITgcm model. As the origins of coordinates are not the same, the MITgcm result is shifted in order to make the comparison.

In addition a very small free mode-1 wave is generated which propagates ahead of the main mode-1 wave. The slaved mode-1 wave train accumulates energy gradually during the evolution of the mode-2 wave propagating up the slope, and a leading depression rarefaction forms followed by trailing oscillatory wave trains. Ahead of this slaved component, there is a small freely propagating mode-1 rarefaction. Note that the vKdV theory predicts that nonlinear effects become more significant as the mode-1 wave moves up the slope, see figure 4.7. Finally, on the flat shelf, the slaved mode-1 wave continues to develop but the freely-propagating mode-1 wave can hardly be seen. Importantly, the amplitudes of these mode-1 waves remain much smaller than those of the main mode-2 wave, so the energy transfer is quite small. This can be confirmed from an analysis of the energy budget, see figure 4.8. Here we use the expressions (4.20, 4.23) for the energy in each mode, consistent with the vKdV theory. But we note that in the fully nonlinear MITgcm simulations, for large amplitude waves this could lead to some significant errors, see Lamb [69]. Nevertheless, mode-2 waves lose 0.68 TJ ($\times 10^{12}$ joules) of energy over the continental slope, of which 23.1 GJ (3.4%) is converted into mode-1 waves, and the rest of the energy is presumably lost due to viscosity and the effects of numerical wave breaking and turbulence.

4.4 From three-layer to two-layer system

The configurations in section 4.3 were set up so that the three-layer fluid system persisted from deep to shallow water, onto the shelf. Thus a mode-2 wave can exist over the whole fluid domain. Here we examine the case when the three-layer fluid system does not extend onto the shelf, where there is instead only a two-layer fluid system. That is, the lower layer depth h_3 decreases to zero at a certain point on the slope. In this scenario a mode-2 wave cannot exist past this point and on the shelf.

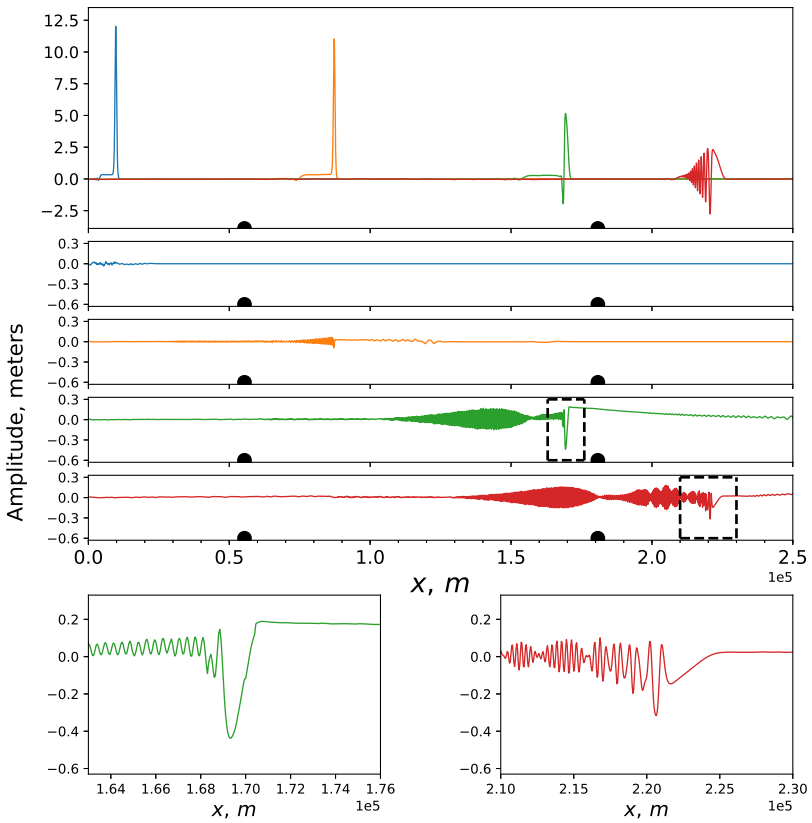

Figure 4.5: The MITgcm simulation of the EXP1 in a three-layer to three-layer system. The upper panel is the mode decomposition result for mode-2 internal solitary waves at times $t = 0,\ 10,\ 21$ and 30 hours, which are shown by blue, orange, green and read solid lines respectively. The lower four panels are results for mode-1 at the same times, and are represented by the same coloured lines as that for mode-2. Dark dots indicate the start and the end of the linearly varying slope, respectively. The lowest two panels are snapshots which are bounded by the corresponding dark dashed rectangle.

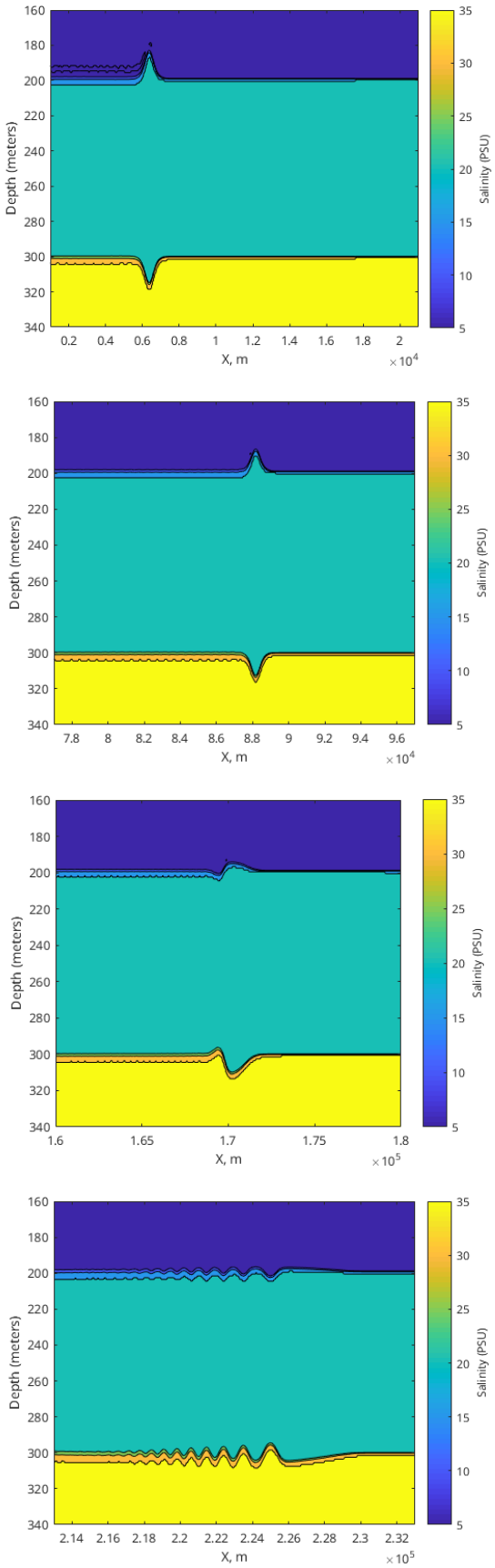

Figure 4.6: The salinity fields, indicating the density field as the temperature is uniform, from the MITgcm simulations of EXP1 in a three-layer to three-layer system. From top to bottom, these are at times $t = 0,\ 10,\ 21$ and 30 hours.

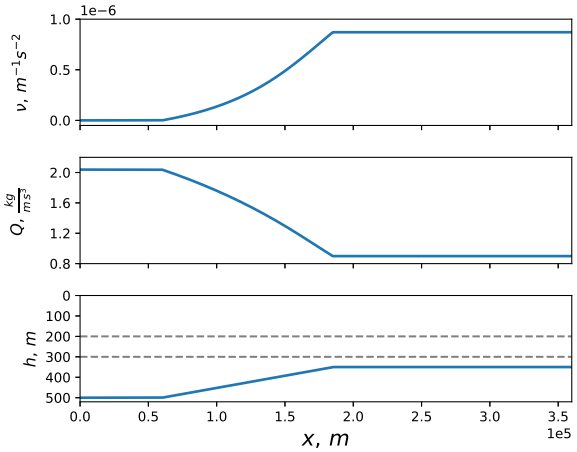

Figure 4.7: Coefficients of the vKdV equation (4.2) for mode-1 in the EXP1. The lowest panel is the corresponding bathymetry and density layers.

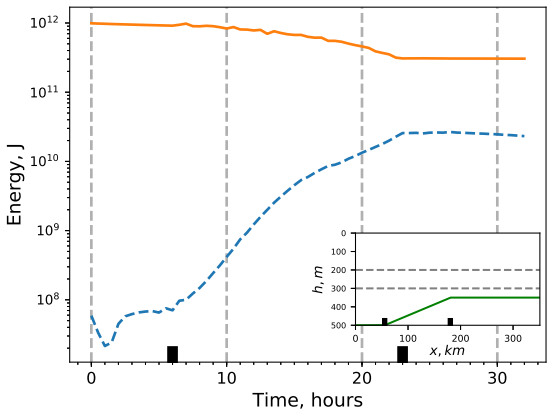

Figure 4.8: The total energy $E_n = K_n + P_n$ in the EXP1, calculated from the MITgcm result, of which mode-1 ($n = 1$) is denoted by the blue dashed line, and mode-2 ($n = 2$) is represented by the orange solid line, together with the corresponding bathymetry and density layers inset. The dark rectangle represents the start and end of the slope respectively. Note that the time cut-off point is selected at $t = 32$ hour, and beyond that point, the freely propagating mode-1 waves radiate away from the calculation domain into the boundary layer, and finally vanish there.

Hence the question examined here is what happens to a mode-2 internal solitary wave as it propagates up the slope. The vKdV theory cannot describe this situation beyond the point where $h_3 = 0$ and consequently we can only use the MITgcm results to investigate this issue.

In the deep water, following the set-up examined in section 4.3, we again build a three-layer system, namely $h_1 = 200,\ h_2 = 100$ and $h_3 = 200\,\mathrm{m}$, but here the bottom layer terminates on the slope, that is, there is a transition point where $h_3 = 0$ and thereafter it becomes a two-layer system on the remainder of the slope and further on the flat shelf, which is labelled as EXP3. With this set-up, comparing with EXP1 in section 4.3, the evolution scenario is similar on the slope before the bottom layer reaches 50 m, see figure 4.9 and 4.10 for the details. After that, the nonlinear coefficient ν, see figure 4.2, which is initially positive, passes through zero, and then keeps decreasing as the bottom layer depth $h_3 \to 0$, and finally $\alpha \to -\infty$, see (4.35), where the KdV theory fails. The MITgcm results show that at first the behaviours on the slope are similar to that in EXP1 (figure 4.5) with a decay of the main mode-2 wave and generation of a small amplitude slaved mode-1 wave and an even smaller freely propagating mode-1 wave. But now, as the transition point is approached, the mode-2 wave is extinguished, and replaced by a mode-1 wave with two components; a slowly moving oscillatory wave train, and a small elevation bore propagating ahead up the slope and onto the shelf. After the waves completely transmit to the two-layer system, the mode-2 wave cannot technically exist and only mode-1 waves can survive. But note that in the MITgcm simulations, the interfaces have a small but finite thickness, which technically does allow mode-2 and higher modes to exist, and form an identifiable signal in the perturbed density field of the pycnocline.

Figure 4.12 and 4.13 show another simulation (labelled as EXP4) in which the thicknesses of the layers are $h_1 = 100,\ h_2 = 300$ and $h_3 = 100\,\mathrm{m}$ in the deep water, and again the bottom layer terminates on the slope. In this case, the nonlinear

coefficient ν in the vKdV equation (4.2), see figure 4.2, is initially negative, opposite from EXP3, and keeps decreasing as the bottom layer depth $h_3 \to 0$, and finally $\alpha \to -\infty$, where again the KdV theory fails. Note that here the initial mode-2 wave is a concave wave, and is not a perfect mode-2 wave in the MITgcm simulation, but has a trailing wave train, as KdV theory predicts. Here no mode-1 waves are visible in the deep water, but as the wave propagates up the slope, again mode-1 waves are generated, similar to those shown in figures 4.5 and 4.9. In this case, after the termination of the three-layer system, a mode-1 coherent wave packet forms, identifiable in the density signal of the thin, but of finite thickness, pycnocline in the MITgcm simulation (not shown here). This wave packet retains its structure on the shelf, but disperses, spreading out and decreasing in amplitude. At the same time a small depression bore forms ahead of this packet, but also disperses and decreases in amplitude as it propagates on the shelf.

These two cases, although different, show that when there is a transition from a three-layer to a two-layer fluid system, the dynamics of the conversion of a mode-2 wave to mode-1 waves is similar overall. In both EXP3 and EXP4 as the mode-2 wave propagates up the slope it deforms and generates some small-amplitude mode-1 waves. After the transition from a three-layer to a two-layer system, small-amplitude mode-1 waves continue and move up the slope and onto the shelf. In EXP3 (figure 4.9), when there is a polarity change on the shelf prior to the transition to a two-layer system, the initial mode-2 wave undergoes a polarity reversal before reaching the transition point, and forms a system of a convex rarefaction wave on which rides a wave train of concave waves. As the transition point is approached, this system disperses and decreases in amplitude. Note that as $h_3 \to 0$, for the mode-2 wave $R = A_1/A_2 \to 0$, see (4.30), and the corresponding horizontal velocity field becomes concentrated in the middle and lower layers, and is positive in the middle layer for the leading rarefaction wave, refer to equation (4.21). Also as $h_3 \to 0$, for a mode-1 wave

$R \to \infty$, and so $\phi_{1z} > 0$ in the middle layer. This implies, from the expression (4.18) with $n = 1$ for the generation of a mode-1 wave from a velocity field $u > 0$ of a mode-2 wave that this will generate a mode-1 wave of elevation. Thus, after the transition, the combination of a rarefaction wave and following wave train forms into a mode-1 elevation bore, from the convex rarefaction wave, followed by a dispersive wave train, both riding on the thin pycnocline. As this system moves onto the shelf, the bore moves ahead of the dispersive wave train, and evolves into a solitary wave, where we note that for this mode-1 wave $\alpha > 0$, see (4.35). In EXP4 (figure 4.12), there is no polarity reversal and the initial concave wave decreases adiabatically in amplitude, with a trailing convex pedestal which grows in amplitude. After the transition, this combination again forms into a mode-1 nonlinear wave packet, but now with a leading depression bore. This is because in this case the leading wave is concave, and the corresponding horizontal velocity field is negative in the middle layer. Hence the mode-1 wave that is generated from this horizontal velocity is now one of depression at its leading edge. As the system evolves onto the shelf, the depression bore begins to break up into a nonlinear wave train, while the following wave packet disperses and decreases in amplitude. Importantly we note that although the leading small amplitude bore has a similar amplitude to EXP3, compare figures 4.9 and 4.12, the following wave packet is noticeably larger in this latter case. We interpret this difference as being due to the relatively larger amplitude and less dispersed structure of the mode-2 wave as it approaches the transition point. The results of the energy budget for these simulations are shown in figure 4.11. In EXP3, only 2.0% of the lost energy 0.92 TJ by the mode-2 waves flows into mode-1 waves, while in EXP4, the conversion rate can reach 15.9% (the mode-2 waves lose 4.14 TJ and 0.66 TJ is obtained by the mode-1 waves). Again, as in EXP1, EXP2 there would seem to be a loss of energy to the effects of wave breaking and turbulence.

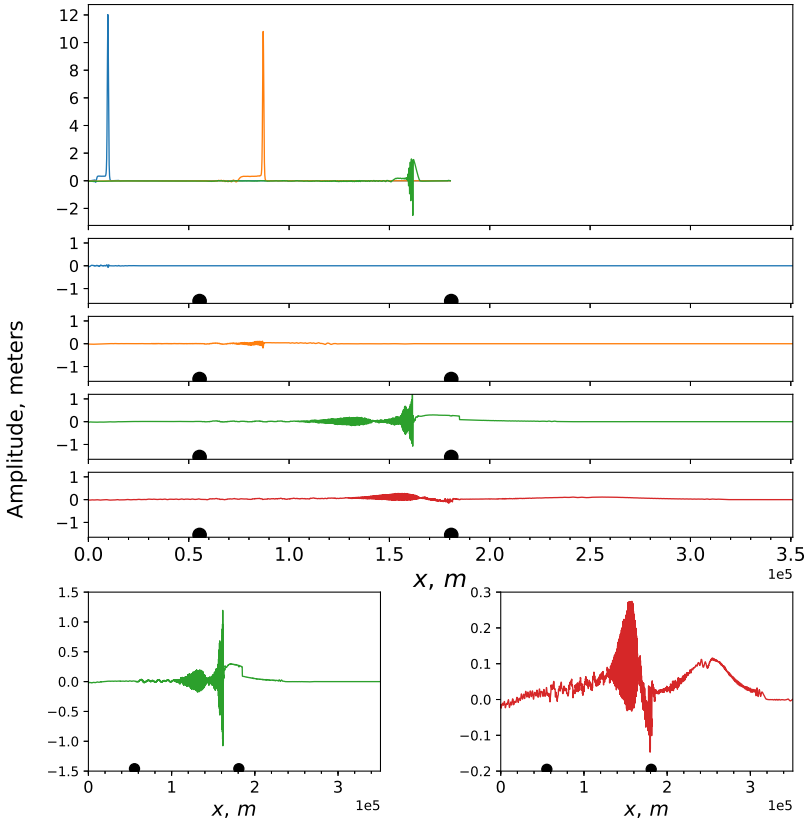

Figure 4.9: The MITgcm simulation of the EXP3 in a three-layer to two-layer fluid system. The upper panel is the mode decomposition result for mode-2 internal solitary waves at times $t = 0,\ 10$ and 21 hours. The lower four panels are results for mode-1 at times $t = 0,\ 10,\ 21$ and 30 hours, and are represented by the same coloured coding as in figure 4.5. Dark dots indicate the start and the end of the linearly varying slope, respectively. The last two panels are the same as the two panels above them, that is, the results for mode-1 at times $t = 21$ and 30 hours, but with an enhanced scale to accentuate the leading mode-1 waves.

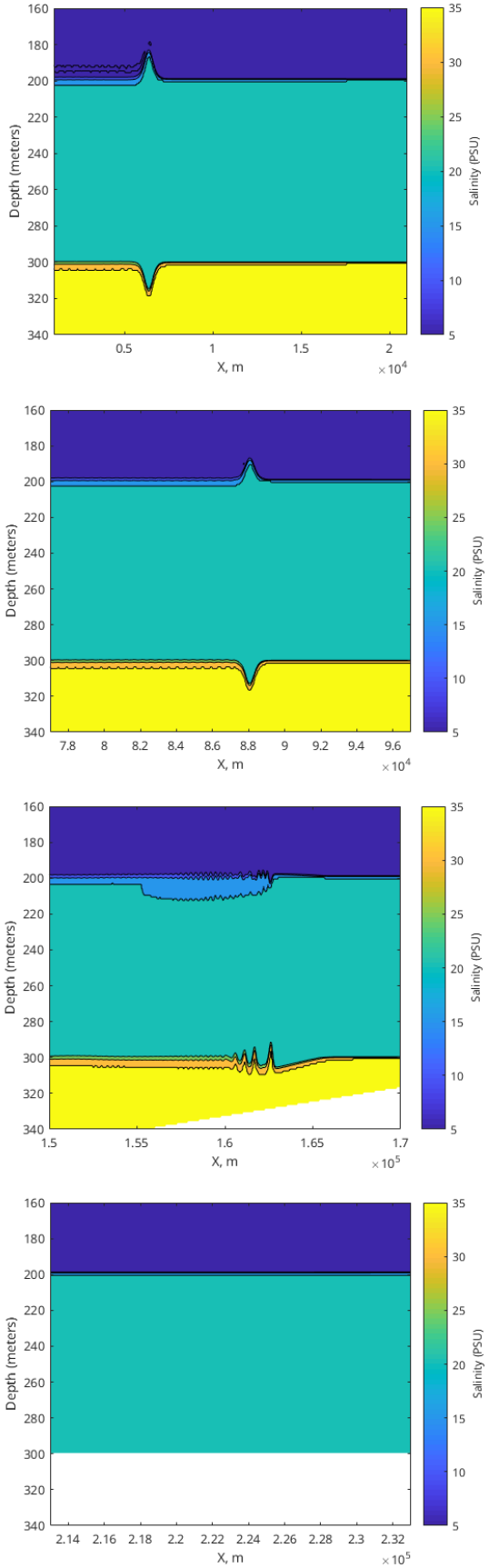

Figure 4.10: The salinity fields, indicating the density field as the temperature is uniform, from the MITgcm simulations of EXP3 in a three-layer to two-layer system. From top to bottom, these are at times $t = 0,\ 10,\ 21$ and 30 hours. The areas in white colour indicate the topography.

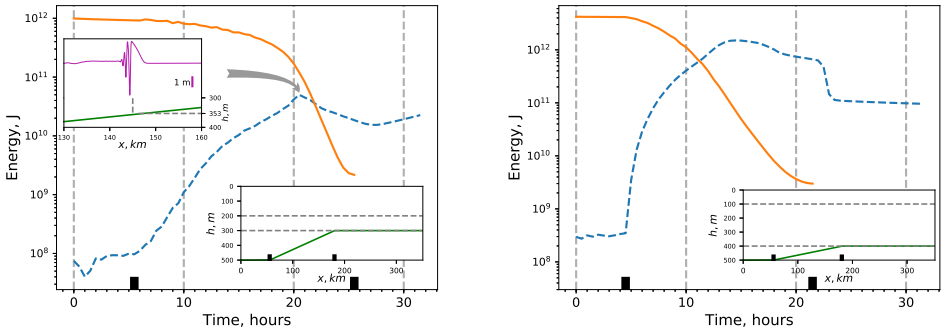

Figure 4.11: The total energy $E_n = K_n + P_n$ of EXP3 (left panel) and EXP4 (right panel). The layout is the same as in figure 4.8, except in EXP3, one extra inset of the mode-2 internal solitary wave propagating to a critical depth $h = 353\,\mathrm{m}$ (where the nonlinear coefficient $\alpha = 0$) is drawn at time $t = 20.5$ hour, and thereafter the mode-1 wave is subject to an adjustment with an increase following a decrease in energy.

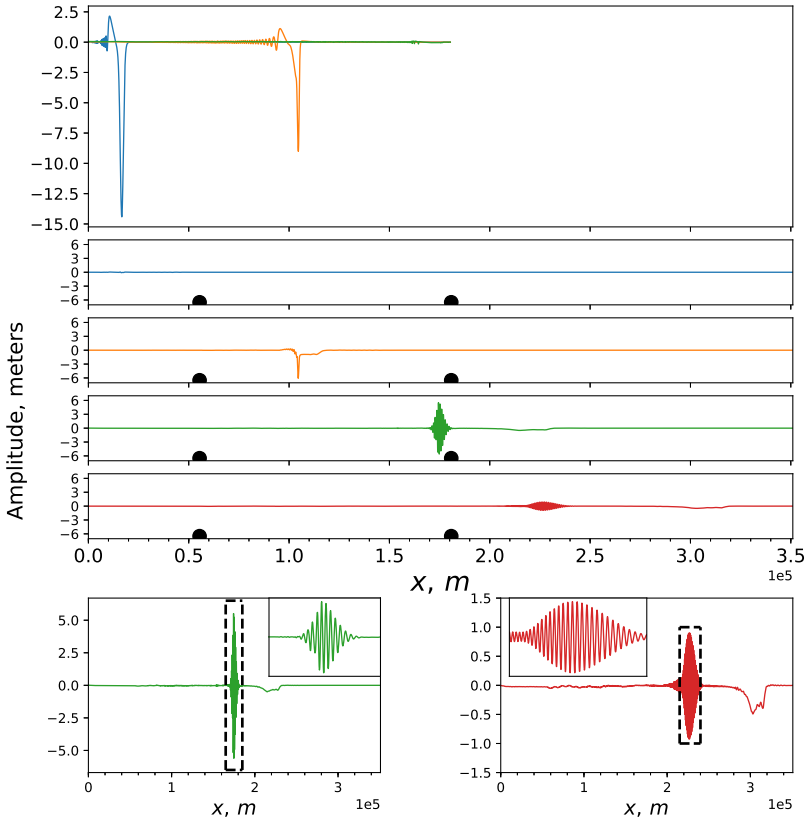

Figure 4.12: The MITgcm simulation of the EXP4 in a three-layer to two-layer fluid system. The layout and coloured coding are the same as in figure 4.9 except that two insets are added onto the last two panels which are snapshots bounded by the corresponding dark dashed rectangle.

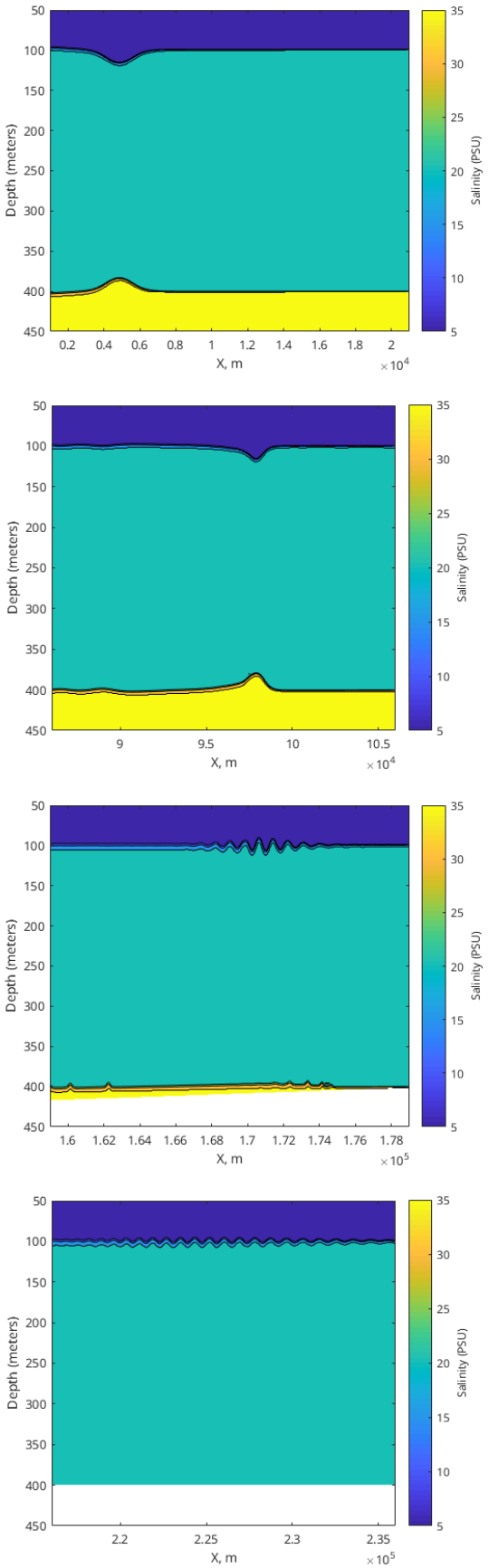

Figure 4.13: The salinity fields, indicating the density field as the temperature is uniform, from the MITgcm simulations of EXP4 in a three-layer to two-layer system. From top to bottom, these are at times $t = 0,\ 10,\ 21$ and 30 hours. The areas in white colour indicate the topography.

4.5 Conclusion

We used the simplest configuration which can support a mode-2 wave, namely a three-layer fluid system, as then the number of fluid parameters is quite small. Given the density field, the topography determines two scenarios. In each an initial mode-2 internal solitary wave propagates onto a slope. In the first case, a three-layer to a three-layer fluid system is considered on a shelf-slope configuration. Depending on the variation of the quadratic nonlinear coefficient ν, this was further classified into two cases. When ν changes sign from positive to negative at a certain critical point on the slope, the amplitude of the mode-2 wave decreases as it propagates up the slope. Then in the vicinity of the critical point, the wave generates a trailing shelf of the opposite polarity. After passing through this critical point and further onto the shelf, the incident mode-2 wave is replaced by a concave solitary wave train, riding on a convex rarefaction wave. This case is contrasted with that when ν does not pass through zero, and there is no such critical point, instead the wave system can move onto the shelf with a reduced, but always positive ν, and thereafter the leading convex solitary wave continues steadily, followed by a small amplitude solitary wave train riding on a concave pedestal. Both these cases are analogous to the case of a mode-1 internal solitary wave propagating up a slope, see Grimshaw [37], Grimshaw et al. [42, 43] for instance. The MITgcm simulations have good agreement with the vKdV theory, both qualitatively and quantitatively. Importantly the MITgcm simulation can also capture the generation of mode-1 waves, which is, by construction, beyond the capability of the vKdV theory. The implementation of a mode decomposition technique facilitates the identification of a small energy transfer from the mode-2 wave to mode-1 waves, mostly slaved to the mode-2 wave, but with a small component propagating ahead of the mode-2 wave.

The other set-up we considered is when the bottom layer vanishes at a transition point on the slope, where $h_3 = 0$, thereby forming a three-layer to two-layer fluid

system. Since the vKdV theory eliminates the possibility of the coupling of mode-2 waves and mode-1 waves, this problem can only be examined using the MITgcm simulations. As expected, the behaviour of the mode-2 wave in the three-layer system is quite similar to that described above, that is, characterised by a decreasing amplitude of the mode-2 wave, a train of the slaved mode-1 waves and some smaller freely propagating mode-1 waves ahead. Then after the transition from a three-layer to a two-layer system, only small-amplitude mode-1 waves continue up the slope and onto the shelf. Nevertheless, the configurations in a three-layer system have a key role in the evolution of the waves even after they propagate into a two-layer system. If a polarity reversal occurs for the mode-2 wave before the transition, then after passing through that critical point (where $\nu = 0$), a system of a convex rarefaction wave carrying a solitary wave train is formed, see figure 4.3. Afterwards this combination transmits to the two-layer system, where mode-2 waves cannot technically be supported and only a mode-1 wave can exist. In the two-layer system, the original leading convex wave fully breaks, and part of the energy goes to a mode-1 bore, which further develops into a elevation mode-1 internal solitary wave, followed by a dispersive wave train. For the case without a polarity change before the transition, qualitatively there is similar dynamics. But, it is noticeable that, after the transition from a three-layer system to a two-layer system, the consequent following wave train is more organised, and has a relatively large amplitude, which indicates a much higher energy transfer rate, 15.9% *v.s* 2.0% as revealed from the energy budget.

In conclusion, our present study suggest that mode-2 internal solitary waves propagate up a slope in much the same manner as mode-1 internal solitary waves, as one would expect since each can be described by a vKdV equation, and the main difference is that in the process, some small but significant mode-1 waves can be generated, presenting a rather complex wave field on the shelf. Importantly, this topographic generation of long wavelength mode-1 waves is essentially different from

the generation of short wavelength mode-1 waves, which can occur on a constant depth and is due to a long-short wave resonance, see Akylas and Grimshaw [4]. However, such co-propagating mode-1 waves are typically exponentially small in the wave amplitude, and we suggest that, unlike the present topographically generated mode-1 waves, are unlikely to be readily observable.

Chapter 5

The propagation of internal solitary waves over 2D variable topography

This chapter presents a horizontally two-dimensional theory based on a variable-coefficient KP (vKP) equation, which is developed to investigate oceanic internal solitary waves propagating over variable bathymetry, for general background density stratification and current shear, if applicable. Following equation (2.18) in Chapter 2, the vKP equation is written in the transformed space as

$$\{U_s + \nu U U_X + U_{XXX}\}_X + \tau U_{yy} = 0\,. \tag{5.1}$$

5.1 Slowly varying solitary waves

One of the basic assumptions of this vKP model is that the y-variations should be sufficiently slow relative to a typical solitary wave scale in the x-direction. This suggests an asymptotic analysis for a slowly varying solitary wave solution of (5.1)

represented by,

$$U \sim a\,\mathrm{sech}^2\{\kappa[X - P(y,s)]\}\,, \quad W = P_s = \frac{\nu a}{3} = 4\kappa^2\,, \tag{5.2}$$

$$V = -\int_X^{+\infty} U\,dX = \frac{a}{\kappa}\{\tanh\left[\kappa(X-P)\right] - 1\}\,. \tag{5.3}$$

In this scenario, the amplitude a and hence the wavenumber κ and the nonlinear phase speed W vary slowly with y and s. Note that (5.2) is defined in a reference frame with linear phase speed c, so that from the mappings (2.14, 2.19), the total phase speed in the physical space is $c_{sol} = c(1-W\lambda)^{-1} \approx c(1+W\lambda)$ since the solitary wave amplitude is required to be small. Using the transformations in (2.14, 2.19) $c_{sol} = c + \alpha a_{sol}/3$ where $a_{sol} = a/Q^{1/2}$ as expected. To determine the variation on the amplitude it is sufficient to substitute (5.2) into the conservation law (2.22) in Chapter 2, with the outcome

$$\left(\frac{2a^2}{3\kappa}\right)_s = \tau\left[\frac{4a^2}{3\kappa}P_y + (\frac{a^2}{\kappa^2})_y\right]_y\,. \tag{5.4}$$

Using the relations that $\nu a = 12\kappa^2, P_s = 4\kappa^2$ this reduces to

$$\left(\frac{\kappa^3}{\nu^2}\right)_s = \tau\left[\frac{2\kappa^3}{\nu^2}P_y + (\frac{3\kappa^2}{2\nu^2})_y\right]_y\,, \quad P_s = 4\kappa^2\,, \tag{5.5}$$

which can be written in the convenient form,

$$\theta_s = \tau\left[2\theta P_y + (\frac{3\theta^{2/3}}{2\nu^{2/3}})_y\right]_y\,, \quad P_s = 4\nu^{4/3}\theta^{2/3}\,, \quad \theta = \frac{\kappa^3}{\nu^2}\,. \tag{5.6}$$

This is a nonlinear mixed hyperbolic-parabolic type system for θ, P, where the first term on the right-hand side of the first equation generates the hyperbolic part and the second term generates the parabolic part. It seems quite difficult to obtain an analytical solution, and hence in the following sections we will numerically solve this

equation system with the constant initial condition that $\theta = \theta_0, P = P_0$. Given an initial wave amplitude a_0, since the coefficients $\nu(y,s)$ and $\tau(y,s)$ are determined by the stratification and topography here, which are known, then the initial condition $\theta_0 = \left[a_0/(12\nu_0^{1/3})\right]^{3/2}$ from equation (5.2), in which $\theta_0 = \theta(y, s = 0)$ and $\nu_0 = \nu(y, s = 0)$. At the same time, note that the waves initially propagate over the flat deep bottom, i.e. no transverse variation, hence the initial condition $P_0 = P(y, s = 0)$ can be arbitrary constant, here we choose $P_0 = 1$. To solve equation (5.6), spatially the terms of first derivative ∂y are approximated by a central finite difference method with second-order accuracy, while the classic fourth-order Runge-Kutta method is chosen to step forward temporally for both θ and P. The spatial and temporal steps are 0.11 km and 1.1×10^{-3} s^3, respectively.

When there are no y-variations, equation (5.6) reduces to the well-known adiabatic law θ is a constant, that is $\kappa \propto |\nu|^{2/3}$ and so $a \propto |\nu|^{1/3}$. However when there are y-variations, then we note that the y-dependence of the coefficients ν, τ can be taken as parametric, consistent with the assumptions made in the derivation of the vKP equation. Assuming here without loss of generality that $\nu > 0$, and since the variation in the transverse direction is very slow, the system (5.6) can be simplified to an asymptotically equivalent form

$$\theta_s = \frac{\tau}{\nu^{2/3}} \left[2\theta\nu^{2/3} P_y + (\frac{3\theta^{2/3}}{2})_y \right]_y , \quad \theta = \frac{\kappa^3}{\nu^2} , \quad P_s = 4\nu^{4/3}\theta^{2/3} . \tag{5.7}$$

But further analytical progress still seems quite difficult without further approximation. Hence, to provide some insight into the structure of the solutions, we linearise this system with respect to the "constant" state $\theta = \theta_0$, noting that this is the adiabatic solution $\kappa \propto \nu^{2/3}$, and so put $\theta = \theta_0 + \widetilde{\theta}$. Linearisation then yields

$$\widetilde{\theta}_s = 2\tau\theta_0 \widetilde{P}_{yy} + \frac{\tau}{\nu^{2/3}\theta_0^{1/3}} \widetilde{\theta}_{yy} , \quad \widetilde{P}_s = \frac{8\nu^{2/3}}{3\theta_0^{1/3}} \widetilde{\theta} . \tag{5.8}$$

The first term on the right-hand side generates a linear hyperbolic equation and small disturbances propagate outward in the y-direction with a speed $y/\varsigma \sim \nu^{1/3}\theta_0^{1/3}(16\tau/3)^{1/2}$, whereas the second term on the right-hand side generates a linear diffusion equation with a diffusion scale y_d where $y_d^2/\varsigma \sim \tau/(\nu^{2/3}\theta_0^{1/3})$, and it is apparent these two terms together constitute the spreading effect in the y-direction. This analysis is similar to that of Kadomtsev and Petviashvili [59] for the stability of a KdV solitary wave to transverse modulations, but more generally, here it demonstrates the extension of that result to the vKP equation (5.1).

As in the well-known KdV theory for a slowly-varying solitary wave, this asymptotic solution does not conserve the mass invariant (2.21), and the resolution is that as the solitary wave deforms a trailing shelf is generated to conserve the total mass. This trailing shelf is essentially a linear long wave of small amplitude but long wavelength and so can carry mass of the same order as that of the solitary wave. The solitary wave mass is $2a/\kappa$ and this varies as $24\theta^{1/3}\nu^{-1/3}$. Relative to the constant state $\theta = \theta_0$, it follows that when ν increases (decreases), the solitary wave amplitude $a = 12\nu^{1/3}\theta^{2/3}$ increases (decreases), then the trailing shelf has the same (opposite) polarity as the solitary wave. However, note that this conclusion could change if θ also has significant variations in the y-direction.

5.2 Model set-up

Two-dimensional effects will be especially significant in an area with an abrupt change in the oceanic background state, such as in the bathymetry, or in the background density and current fields. A typical instance is the New York Bight, which is characterised by a large area of continental shelf containing the Hudson Canyon, see figure 5.1. This area is also affected by the strong Gulf Stream current, as well as by coastal river inflow, and all these factors together make the local wave dy-

namics quite complicated. As ISWs propagate up the shelf from deep water, and pass through the Hudson Canyon, we expect that wave diffraction and refraction will occur. Motivated by this and similar examples we set up an idealised undersea canyon-type topography $h(x, y)$ with typical oceanic length scales, see figure 5.2,

$$h = \frac{\tanh \Omega + 1}{2} \cdot (h_1 - h_2) + h_2 \,, \tag{5.9}$$

$$\text{where} \quad \Omega = \frac{K_2 - K_1 M_y}{x_1 - x_0} \cdot (x - x_0) + K_1 M_y \,, \tag{5.10}$$

$$\text{and} \quad M_y = \left[\tanh \left(\frac{y + y_{ts}}{y_{tw}} \right) - \tanh \left(\frac{y - y_{ts}}{y_{tw}} \right) \right] \cdot L_y + 1.0 \,. \tag{5.11}$$

Here we set $y_{ts} = 6000\,\text{m}$, $y_{tw} = 2000\,\text{m}$, $L_y = 0.7$, $K_1 = -2.7$, $K_2 = 2.7$, and the topography is confined in a domain with size $x \times y = [0 : 80] \times [-40 : 40]$ km^2, so that two edges in the x direction are $x_0 = 0$ and $x_1 = 80\,\text{km}$, while the water depth parameter $h_1 = 350\,\text{m}$ and $h_2 = 500\,\text{m}$ respectively. We also consider an idealized plateau-type topography, see figure 5.2, whose expression is the same as that of the canyon case, except that

$$M_y = \left[\tanh \left(\frac{y - y_{ts}}{y_{tw}} \right) - \tanh \left(\frac{y + y_{ts}}{y_{tw}} \right) + 2 \right] \cdot L_y + 1.0 \,. \tag{5.12}$$

Using these idealized topographies makes it feasible to conduct analytical work in the sequel. Although realistic topography is not considered here, we contend the framework used here can be easily and effectively migrated to the implementation of real topography, whose transverse variation is relatively slower than that in the wave propagation direction. Further, as customary, since the surface disturbances induced by ISW are usually very small (typically $\mathcal{O}(10^2)$ smaller), we make the rigid lid approximation, and also set the background current, $u_0(z) \equiv 0$. The background temperature and salinity profiles are the monthly averaged data from the World Ocean Atlas 2013. We choose data in July at 37.5°N, 72.5°W, in the vicinity of the

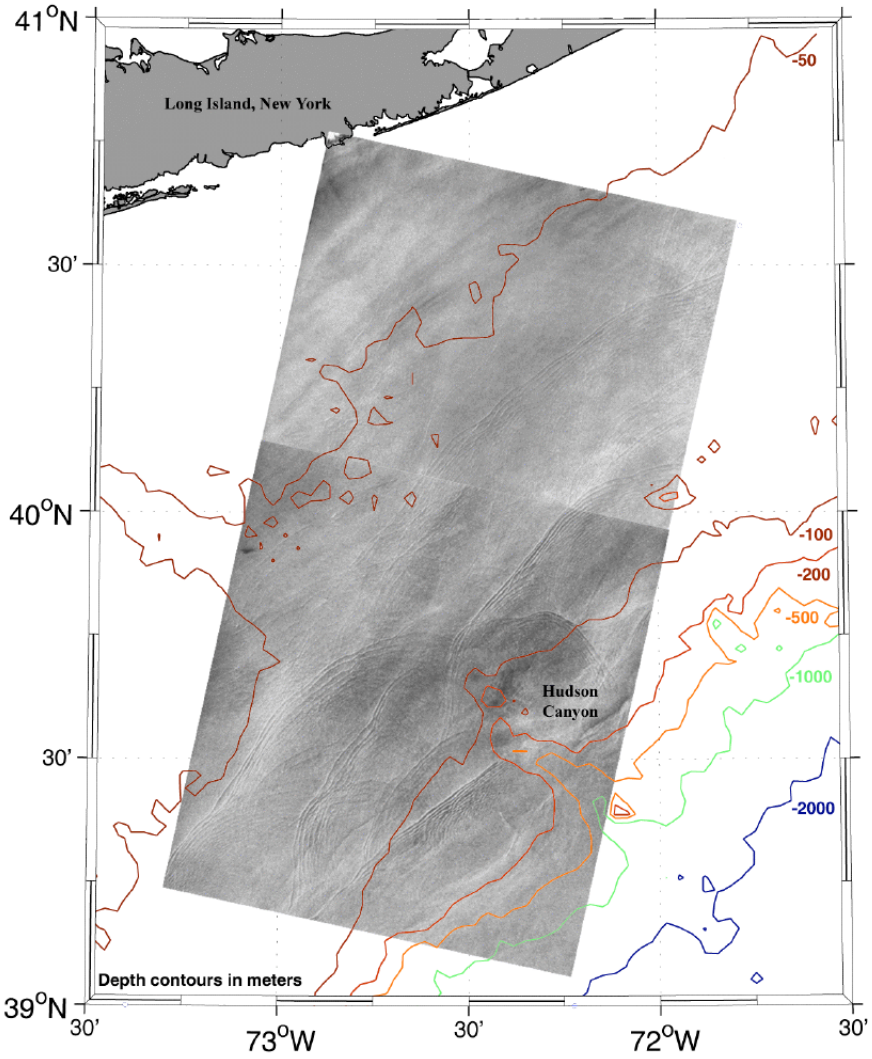

Figure 5.1: ERS-1 synthetic aperture radar (SAR) images of the New York Bight acquired on 18 July 1992 at 15:35 UTC superimposed on the water depth contour lines. (Figure adapted from Jackson [56].)

Hudson Canyon, which is shown in figure 5.3.

When examining 2D effects, another important issue is the preparation of the initial condition. To simulate the waves from a generation site, here we select the well-known KdV solitary wave but with a y-envelope imposed,

$$U(X, y, \varsigma = 0) = E(y) \left\{ a_0 \operatorname{sech}^2 \left[\kappa_0 (X - X_0) + D(X) \right] \right\} , \quad \nu_0 a_0 = 12 \kappa_0^2 . \tag{5.13}$$

Here X_0 is chosen to place the solitary wave in the deep water where $\nu = \nu_0$. $E(y)$ is an envelope function in the transverse y direction, equal to unity in a specified

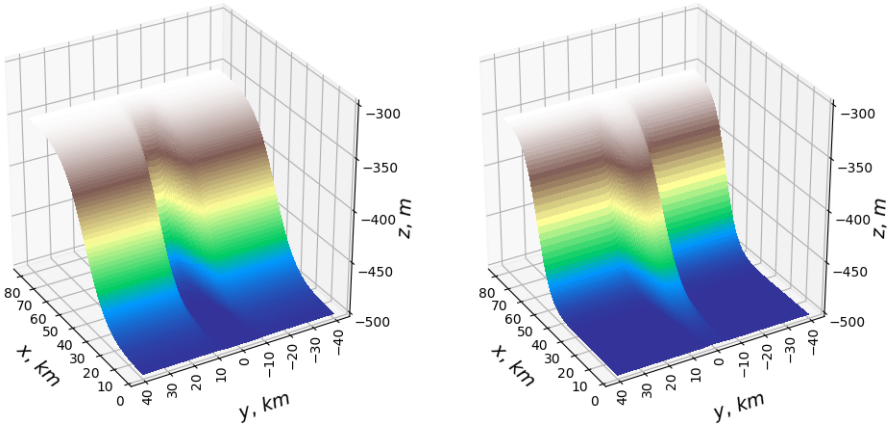

Figure 5.2: Canyon-type (left panel) and plateau-type (right panel) topography. For both cases, the depth range is from 350 to 500 m, while the width of the canyon (or plateau) is approximately 20 km.

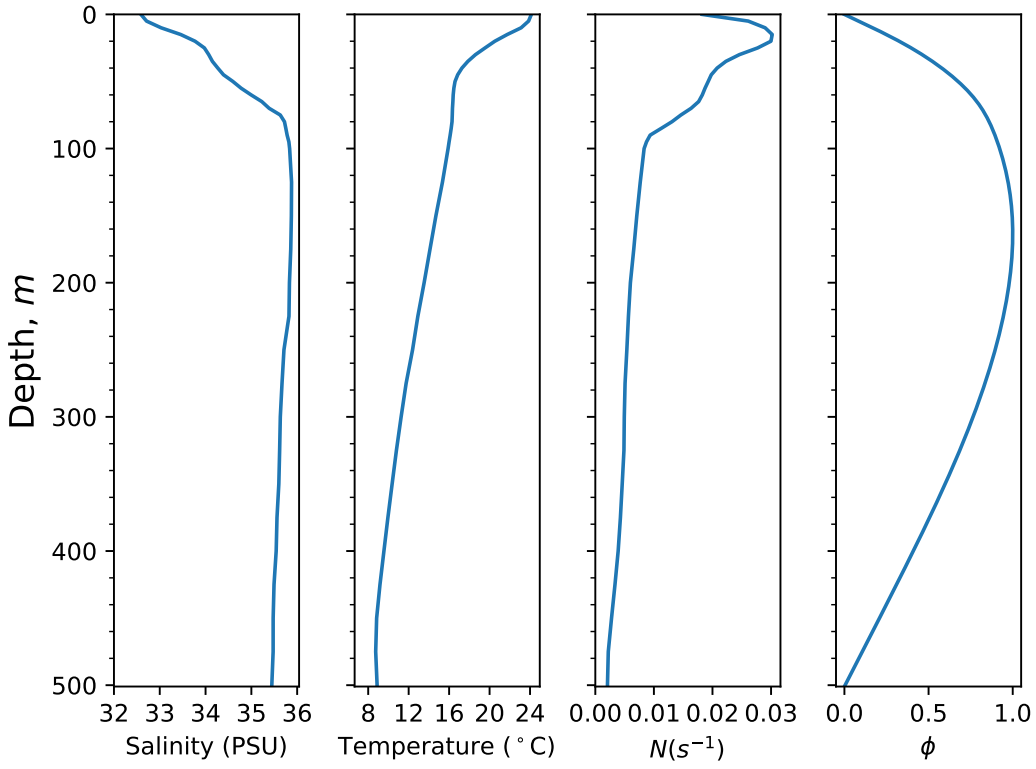

Figure 5.3: The panels from left to right are vertical profiles of the salinity, temperature, buoyancy frequency N and corresponding mode-1 modal function ϕ from equation (4.3, 4.4) respectively. Note that the extrema of N and ϕ are achieved at depths $h = 16$ and $h = 165$ m respectively, which indicates that the most significant internal wave disturbance occurs at a depth where the density gradient is not the largest.

region $|y|< L$ and tapering to zero outside that range,

$$E(y) = \frac{1}{2}\{\tanh\,(\frac{y+y_e}{y_w}) - \tanh\,(\frac{y-y_e}{y_w})\}\,. \tag{5.14}$$

Note that the attenuation in the y-direction should be greater than that in the X-direction, so we choose $y_w \gg 1/\kappa_0$, and also we require $y_e \gg y_w$ to ensure a large value of L. To isolate the dynamics of the 2D topography, we also did simulations with a y-independent initial condition, that is $E(y) \equiv 1$. The mass constraint (2.21) must be satisfied, which implies that in the Fourier space, solutions have no energy at the zero wavenumber. As a consequence, a pedestal $D(X)$ needs to be superimposed on the KdV solitary wave. For a numerical domain of total length $2L_X$ in the X direction, the simplest choice is $D(X) = -12\kappa_0/(\nu_0 L_X)$, so that the initial mass is zero,

$$\int_{-\infty}^{\infty} \left\{a_0\,\mathrm{sech}^2[\kappa_0(X-X_0)] + D(X)\right\}\,dX = \frac{2a_0}{\kappa_0} - \frac{24\kappa_0}{\nu_0} = 0\,. \tag{5.15}$$

The expression (5.15) is a good choice for a periodic domain. However because here two sponge layers are deployed at the two edges of the X-domain (details below), a form with an envelope which avoids possible end effects is used,

$$D(X) = \frac{D_0}{2}\{\tanh\,(\frac{X+L_e}{L_w}) - \tanh\,(\frac{X-L_e}{L_w})\}\,, \quad \int_{-\infty}^{\infty} D(X)\,dX = 2D_0L_e = -\frac{24\kappa_0}{\nu_0}\,. \tag{5.16}$$

In principle, the lengths L_e and L_w can be chosen freely, but to facilitate the numerical calculations, it is better to keep the pedestal small, that is to say $|D_0| \ll a_0$, and hence $|\kappa_0|L_e \gg 1$, so one combination of the typical values is $L_e = L_X/2, L_w = L_X/4$.

The asymptotic theory developed in section 5.1 can be applied to estimate the deformation of the solitary wave amplitude a, ignoring any effect of the small pedestal. First, we use the asymptotic solution for $\theta \sim \theta_0$ in equation (5.7) where $\theta^2 \propto a^3/\nu$ to

estimate that overall the amplitude a will deform adiabatically as $|\nu|^{1/3}$, with a consequent effect on the phase speed. In the physical variables x, t this is $c/(1-W\lambda) \approx c(1+W\lambda)$ since $W = \nu a/3 \sim |\nu|^{4/3}$ is a small perturbation. Then, in addition, the effect of the envelope function $E(y)$ can be estimated using the linearised system (5.8). It is clear that the main variation will then come from the end-points $y = \pm y_e$ of the envelope. These will generate small disturbances propagating in the y-direction with speeds proportional to $\nu^{1/3}\theta_0^{1/3}(16\tau/3)^{1/2}$, and at the same time diffusing on a length scale y_d where $y_d^2/s \sim \tau/(\nu^{2/3}\theta_0^{1/3})$. Both processes are enhanced as the initial wave amplitude increases through the dependence on $\theta_0^{2/3} \propto a_0$, and also enhanced as y_w decreases, that is sharper fronts at the ends of $E(y)$.

5.2.1 Numerical method and results

Although the formulation of the vKP equation (5.1) is for any mode, in this paper we focus on only mode-1 waves, which are the most commonly observed in the ocean. Using the background profiles shown in figures 5.2 and 5.3, the nonlinear coefficient $\nu < 0$, indicating that mode-1 ISWs are waves of depression. To ensure the simulations are in the weakly nonlinear regime, here we choose $-15\,\mathrm{m}$ as the initial amplitude in all cases.

In both cases of the undersea canyon-type and plateau-type topography, the initial solitary wave with the envelope $E(y)$ defined in (5.14) immediately disperses along the transverse y direction when the simulations start, and importantly the wave fronts are not straight, but instead are curved backwards relative to the x direction, see figure 5.4. This is because the local phase speed is a function of the local wave amplitude, which decays on both sides away in the y-direction from the initial main wave centred at $y = 0$. This permanent cross-domain dispersion results in a dramatic decrease of the amplitude of the main wave with distance in the x-direction of propagation. On the other hand, after propagating away from the flat

bottom and up the slope, the waves also begin to deform in the x-direction due to the effect of the nonlinear coefficient ν in (5.1) which combines the physical nonlinear coefficient α with the physical linear dispersive coefficient β, and also absorbs the magnification factor Q, see figure 5.6. The asymptotic theory developed in section 5.1 predicts the deformation of the main wave is determined by two components in the mapping space, that is, the terms related with ν and τ respectively, see equation (5.7). More specifically, let us focus on the central line in the y direction, that is $y = 0$. Figure 5.5 shows that along the propagation direction $|\nu|$ increases, and hence the amplitude of the evolving main wave will increase, since it deforms as $|\nu|^{1/3}/Q^{1/2}$ in the physical space, but at the same time the afore-mentioned spreading in the y-direction will lead to some amplitude decay. It turns out the latter is overwhelmingly significant and causes the wave amplitude to decay, see figure 5.4. To conserve the total mass, this decay generates a trailing shelf with positive polarity, and there is evidence that this shelf begins to fission into several small ISWs.

The features described above occur for both the canyon and plateau cases, and the main difference between these two cases is that the central part of the wave field around $y = 0$ is propagating faster over the canyon than over the plateau, see figure 5.4. This can be partly attributed to the topographic variations in the linear phase speed c, see figure 5.6, which shows that c is greater over the canyon than over the plateau. However the difference is quite small, of $\mathcal{O}(5\%)$, and comparable with the change in c from deep to shallow water, due to scaling dependence on $\sqrt{h}$. Furthermore, this effect is purely kinematic and linear, whereas the simulations of the nonlinear vKP equation (5.1) are in a reference frame moving with the speed c, and will contain dynamic effects due to the amplitude-dependent phase speed W for the evolving ISW. This can be estimated from our simulations as follows. Suppose that the y-variations (the canyon or plateau) are removed from the topography, then the evolving ISW will deform according to the adiabatic law $\kappa \propto |\nu|^{1/3}$ and

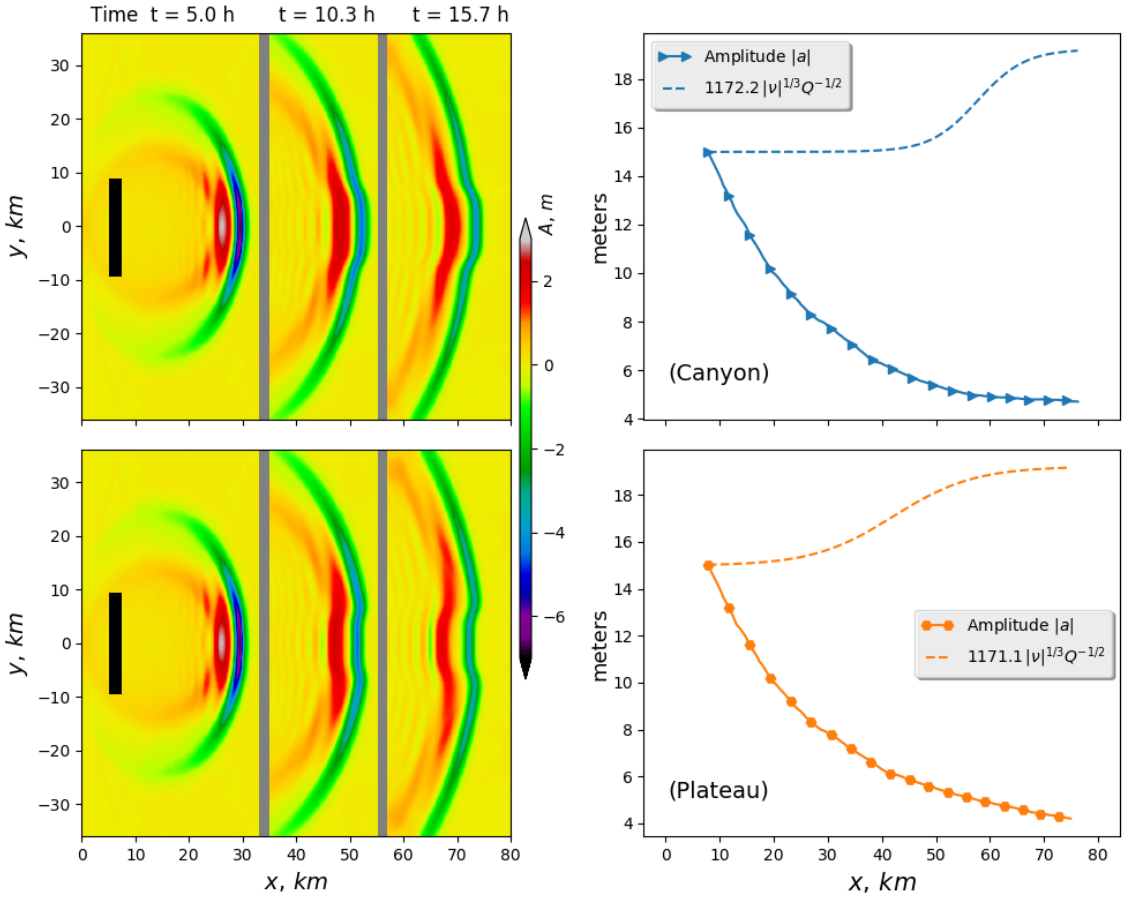

Figure 5.4: Three snapshots of the wave amplitude A for the canyon-type (top left panel) and plateau-type (bottom left panel) topography at times $t = 5.0$, 10.3 and 15.7 hours are illustrated. The initial solitary wave with an amplitude of $-15\,\mathrm{m}$ is indicated by a black rectangle, and the results at different times are separated by solid grey columns. The amplitude of the leading wave $|a|$ in the x-direction at the central point $y = 0$, together with the $|\nu|^{1/3}Q^{-1/2}$ times a normalising factor are plotted on the right two panels, where the discrepancy in the evolution of $|a|$ and $|\nu|^{1/3}Q^{-1/2}$ can be attributed to the significant spreading effect in the y direction due to the envelope $E(y)$ imposed on the initial solitary wave.

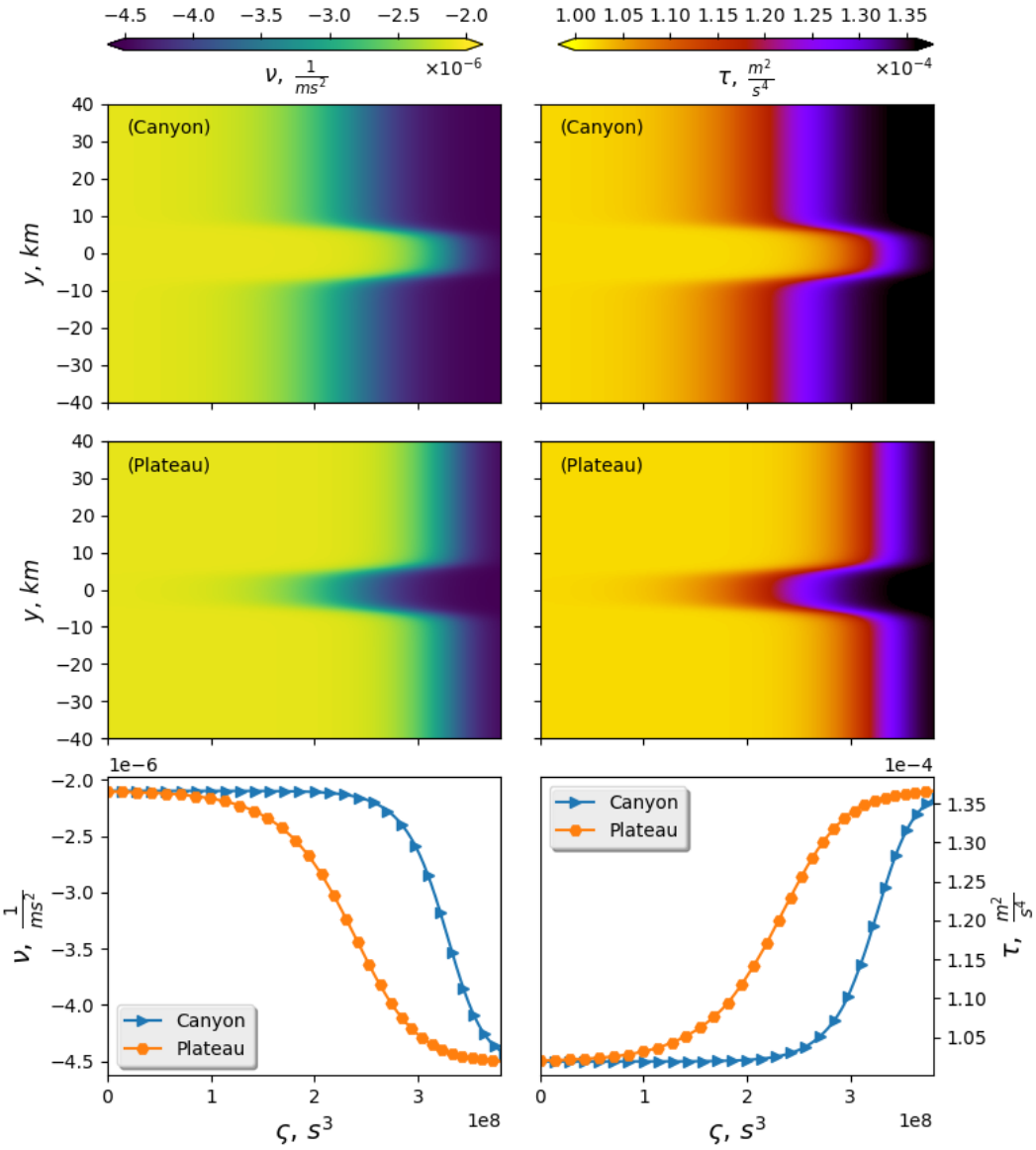

Figure 5.5: The nonlinear coefficient ν and the y-dispersive coefficient τ in the transformed space for both the canyon-type and plateau-type topography are shown in the left two and right two panels respectively, whereas the values at the centre point $y = 0$ are displayed on the lowest two panels.

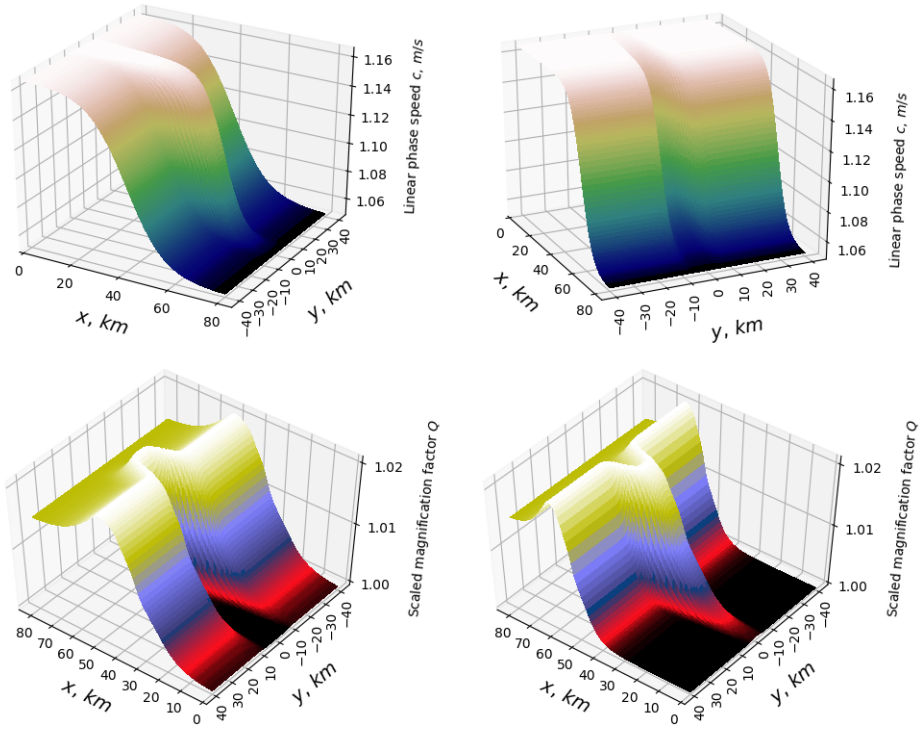

Figure 5.6: The linear phase speed c calculated from the modal function for cases of the canyon-type (left top panel) and plateau-type (right top panel) topography. Formally c is positively associated with the water depth h, that is, $c = \sqrt{Nh}$ for internal waves. The bottom two panels are the normalised linear magnification factor Q also for canyon (left) and plateau (right) cases, which are of the same order as c.

then $W = 4\kappa^2$, see (5.2). This forms a base level to determine the effect of a canyon, or plateau, on the nonlinear phase speed W. Then with the canyon or plateau topography restored we use the asymptotic expression that $\theta = \theta_0$, see (5.7) and the accompanying discussions. Of course, this adiabatic estimate is within the confines of a slowly-varying assumption, so that at fixed "time" s, the state θ is asymptotically equivalent no matter whether or not there are y-variations in the background topography. Then from equation (5.7) we get that

$$\frac{W_c}{W_r} = \left(\frac{\nu_c}{\nu_r}\right)^{4/3} \quad \text{and} \quad \frac{W_p}{W_r} = \left(\frac{\nu_p}{\nu_r}\right)^{4/3}, \tag{5.17}$$

where the subscript r indicates the reference level without y-variations, while c and p indicate the canyon and plateau case respectively. The results of (5.17) are shown in figure 5.7. Initially, the waves are over the flat bottom where there are no y-variations, but with the propagation up the slope, which will then become more and more significant. We note immediately an important consequence, in view of the nonlinear effects of y-variations on W, the canyon-type topography actually slows down the propagation ($W_c/W_r < 1$), contrasting with the speed-up of the plateau-type topography ($W_c/W_r > 1$). Nevertheless, the magnitude of $W\lambda = \nu a\lambda/3$ ($\mathcal{O}(10^{-1})$) is much smaller than the corresponding linear phase speed c ($\mathcal{O}(1)$), which is to say, although the effects of the y-variations can slightly modulate the phase speed $c_{sol} \approx c(1+W\lambda)$, the linear phase speed c is still dominant, and this is precisely what is seen in figure 5.4 and 5.8.

Although the simulations shown in figure 5.4 are intended to describe the propagation of ISW over 2D topography in the ocean, the underlying dynamics induced by the topography alone is not very well exhibited, since it is mostly hidden by the significant y spreading induced by the truncated initial condition. In practice oceanic ISWs are limited in the transverse direction, however this scale could be quite long, and hence in figure 5.8 we show the simulations when the initial condition on the flat

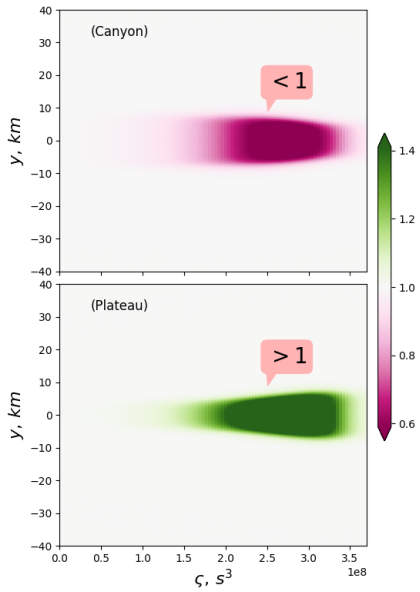

Figure 5.7: The dimensionless nonlinear phase speed W with respect to the base level (without y-variations) for the canyon-type and plateau-type topography.

bottom before the waves reach the slope has no y-dependence, that is $E(y) \equiv 1$. The evolution of the wave again obeys the adiabatic law in the physical space, the amplitude of the leading wave $|a| \sim |\nu|^{1/3}/Q^{1/2}$, and due to mass conservation, a trailing shelf (indicated by light green colour) of the same polarity is generated. Initially, the wave evolution at the central part around $y = 0$ behave qualitatively similar to the previous cases, that is, it is largely determined by the linear phase speed c, but at the same time, is slightly modulated by the small nonlinear phase speed W, which has an opposite effect to that of c. Then after moving up the slope, the effects of the y-variations in the bathymetry become important and so the adiabatic law fails, and the y-dependence has to be taken into account in equation (5.5) or (5.6). With the gradual propagation up the slope, the waves in the canyon (plateau) propagate ahead (behind) the waves outside, and the non-adiabatic effects due to the y-variations of the topography become further enhanced, leading to a significant distinction between the wave amplitudes at different y-locations. Nevertheless, the total mass along the x direction on each y-section has to be conserved, which, together with the spreading effect in the y direction, leads to a complicated transverse modulation (shown by the

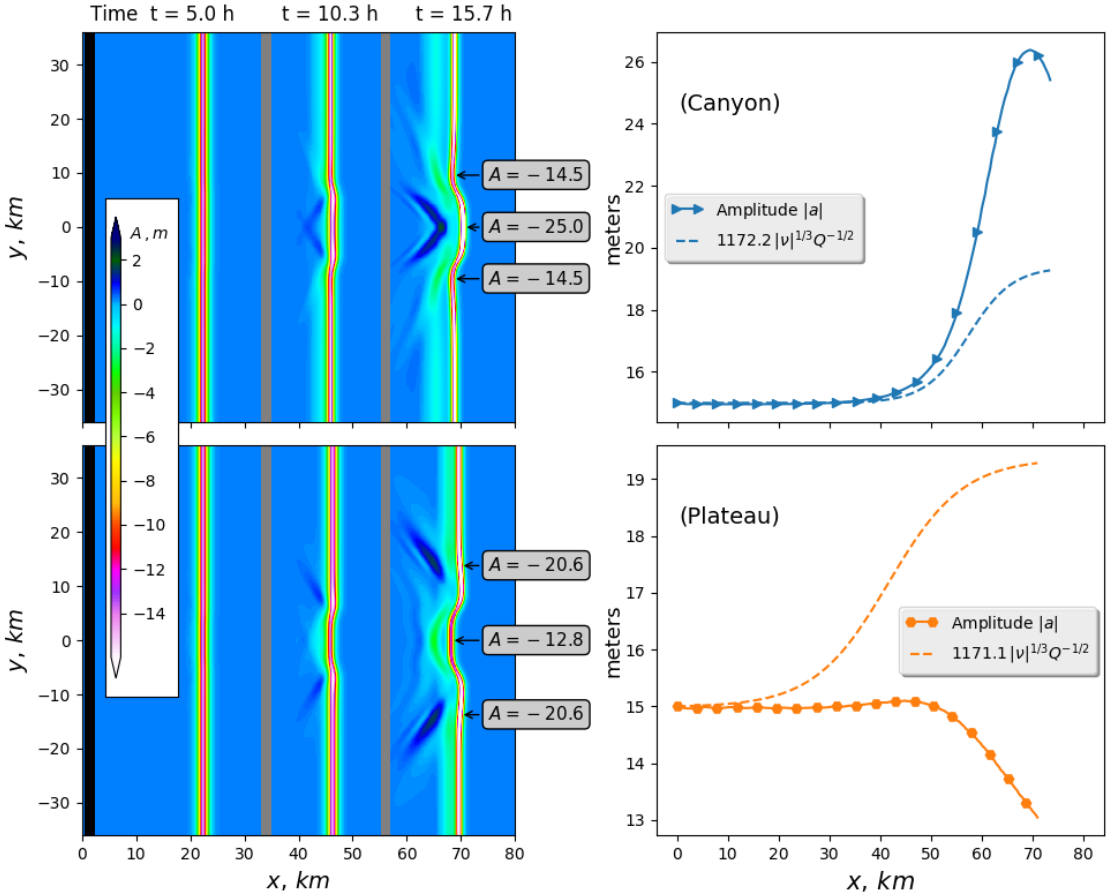

Figure 5.8: The left two panels are the wave amplitudes for both the canyon-type (top panel) and plateau-type (bottom panel) topography, where three time layers are shown (marked over the pictures), and each of them are separated by grey solid columns. The initial wave with an amplitude of $-15\,\mathrm{m}$ is represented by a dark rectangle, which fills all the y domain and enters the region from $x = 0$. In each case, typical wave amplitudes A at three points are listed. The right two panels show the corresponding amplitudes of the leading waves $|a|$ along the central line $y = 0$ in the y direction, and additionally $|\nu|^{1/3}Q^{-1/2}$ times a normalising factor is also plotted.

dark blue colour).

To examine this explanation in more detail, a set of calculations based on the equation system (5.6) is shown in figure 5.9 where we plot the amplitude of the leading wave using the expressions for $\theta = \kappa^3/\nu^2$ in (5.6) and the solitary wave expression $\nu a = 12\kappa^2$ (5.2) so that $a = 12(\theta^2\nu)^{1/3}$. Note that the asymptotic theory (5.6) is based on (2.22) and so conservation of wave action flux is automatically satisfied. It is apparent that in the canyon case, over the slope, the amplitude of the leading wave $|a| = 12(\theta^2|\nu|)^{1/3}$ in the canyon increases, contrasting with the decline in the periphery of the canyon. Moreover, this feature expands with "time" s and exerts more influence on the wave field, as the asymptotic theory based on (5.6) predicts. Simultaneously, at the central part, the increase of the mass represented by the leading wave $24(|\theta/\nu|)^{1/3}$ leads to an opposite polarity trailing shelf (see the dark blue colour in figure 5.8) in order to conserve the total mass in the X direction. In contrast, the mass undergoes a decrease outside the submarine canyon, and so using the mass conservation law again, a trailing shelf of the same polarity forms, which further develops into several small ISWs (see the light green colour in figure 5.8). A similar interpretation can be applied to the plateau case, but with an opposite structure. As we have noted, small y-variations of the topography can lead a significant distinction through the coefficients ν and τ. In order to examine which coefficient is the more effective, we show in figure 5.10 calculations from the system (5.6) when the y-dependence of ν and then τ are separately removed. We see that when only the y-dependence of the coefficient ν is removed, the wave field is quite different from that using the full expression for ν, see figure 5.9. However if instead only the y-variations in τ are removed, then the wave structure is almost the same as when the full expression for τ is used. We infer that it is the y-variations in the nonlinear coefficient ν which essentially determine the evolving wave field, at least for the system parameters used here.

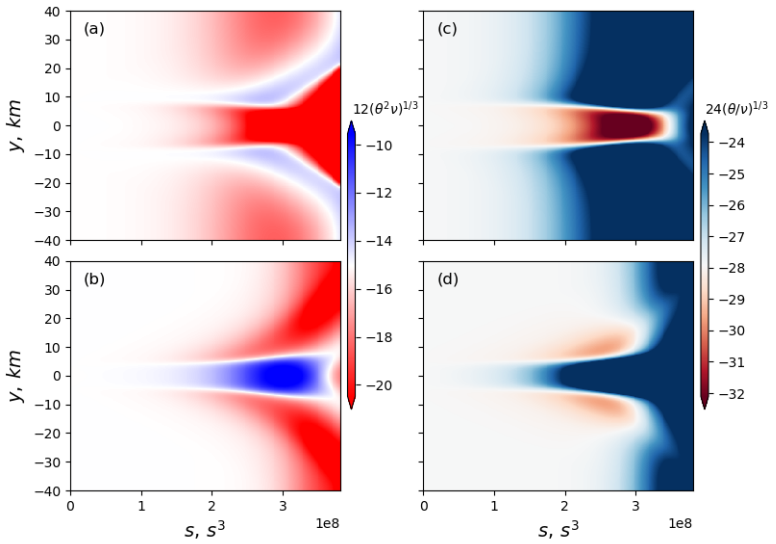

Figure 5.9: The leading amplitude $a = 12(\theta^2\nu)^{1/3}$ calculated from equation system (5.6) in the transformed space for the canyon-type (a) and plateau-type (b) topography, whereas the mass represented by the leading wave $24(\theta/\nu)^{1/3}$ is shown in (c) for the canyon-type topography, (d) for the plateau case.

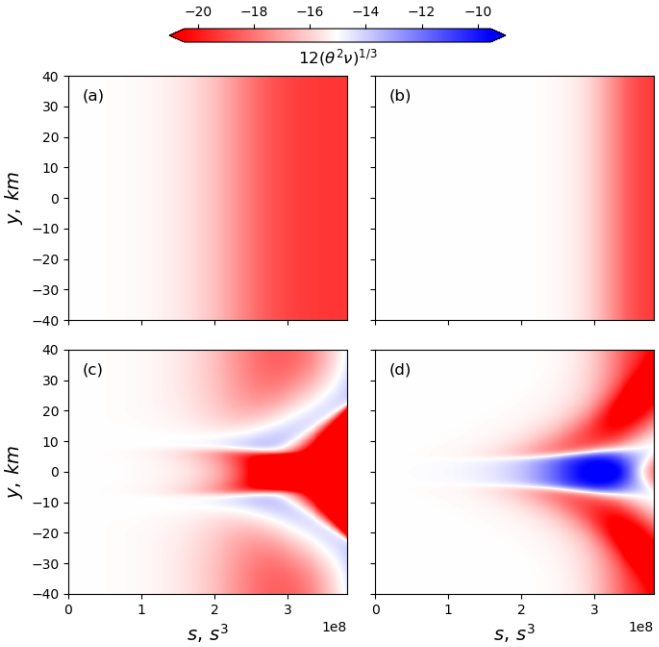

Figure 5.10: The leading wave amplitude $a = 12(\theta^2\nu)^{1/3}$ calculated from equation system (5.6) in the transformed space for the canyon-type ((a) and (c)) and plateau-type ((b) and (d)) topography, where (a) and (b) are the results based on the primitive $\tau(y, s)$, but a new $\nu(s)$ whose y-variations are removed. Similarly, (c) and (d) use $\nu(y, s), \tau(s)$, in which the y-dependence of τ is erased.

5.3 MITgcm model simulations

Access to 2D observational data which incorporates a complete shoaling process is impractical. Thus here we use instead a fully nonlinear and non-hydrostatic three-dimensional (3D) primitive equation model, MITgcm, to do both qualitative and quantitative comparisons.

Since our presented KP theory is non-dissipative, the dissipation (eddy viscosity) in the MITgcm model is also set to be zero, so that formally it solves the incompressible Boussinesq equations. The simulation domain, topography and background profiles are exactly the same as in the KP theory, see figure 5.2 and 5.3. In the x direction, 60 of a total 800 grid points at the end of the domain are designed to be a boundary layer with a decrease of resolution, telescoped exponentially from 100 to $10^4\,m$, whereas the same strategy is used to avoid reflections from boundaries in the y direction, and both sides hold 30 grid points as boundary layers (totally there are 360 grid points), with resolution from 250 to $10^4\,m$. In the vertical direction, there are 190 z-levels with $2\,m$ resolution in the upper 175 layers followed by 15 bottom layers with $10\,m$ resolution. Note that as indicated by the modal function, see figure 5.3, the maximum vertical excursion should occur at approximately depth $h = 165\,m$, which is covered by the fine resolution. Time step is $2\,s$, short enough compared with the typical temporal scale of a mode-1 ISW.

To be succinct, here we only show the results with the truncated initial condition, which can be observed more often in the real ocean. As the KdV-type solitary wave, given by equation (5.13), is not fully compatible with the Boussinesq equations solved by the MITgcm model (although for small-amplitude waves which are in a weakly nonlinear regime, the difference is very small), thus a 2D simulation is first conducted on a flat bottom (depth $h = 500\,\mathrm{m}$) environment with a KdV solitary wave as the initial incident wave, using the background profiles in figure 5.3. Then we let the wave evolve until it reaches a stable state, which is cut off and ready to be used.

Essentially in the y direction, it is not easy to impose a smooth envelope on the initial solitary wave in the MITgcm 3D simulations, as described in equation (5.13). A compromise method is to copy this preliminary 2D solution to fill a central region whose y-direction width is almost the same as the central part of the envelope given in equation (5.14), whereas the other areas are assumed to be at rest. But these sudden jumps between the initial wave and its periphery will undoubtedly modulate the dynamics to some extent. Indeed, the discrepancy induced by the initial conditions is significant within several hours after the model launches, but nevertheless then a good agreement between the MITgcm and the vKP theory is achieved, see figure 5.11.

To further examine the robustness of the vKP simulations, the locations of the wavefronts in the x-y space at four different time layers are depicted in figure 5.11, and these demonstrate that overall a good agreement holds between the vKP simulations and the MITgcm model, except that the curvatures of the wave fronts in the vicinity of canyon (or plateau) topographic features are more abrupt in the KP simulation, which can be partly ascribed to the interpolation used when that is transformed back from the mapping space to the physical space. To make this claim more robust, a quantitative comparison of the amplitude A is also shown in figure 5.11, in which the wave amplitude of the MITgcm model is calculated using a mode decomposition technique developed by Yuan et al. [116], see Section 4.1 in Chapter 4, which was originally derived in a 2D (x-z) domain. However, since here the y-variations are assumed to be much slower than the x-variations, this technique can be applied in any (x-z) section without too much loss of accuracy. We see that the agreement is good, implying that here the variable coefficient KP model and the accompanying analytical interpretations are quite robust.

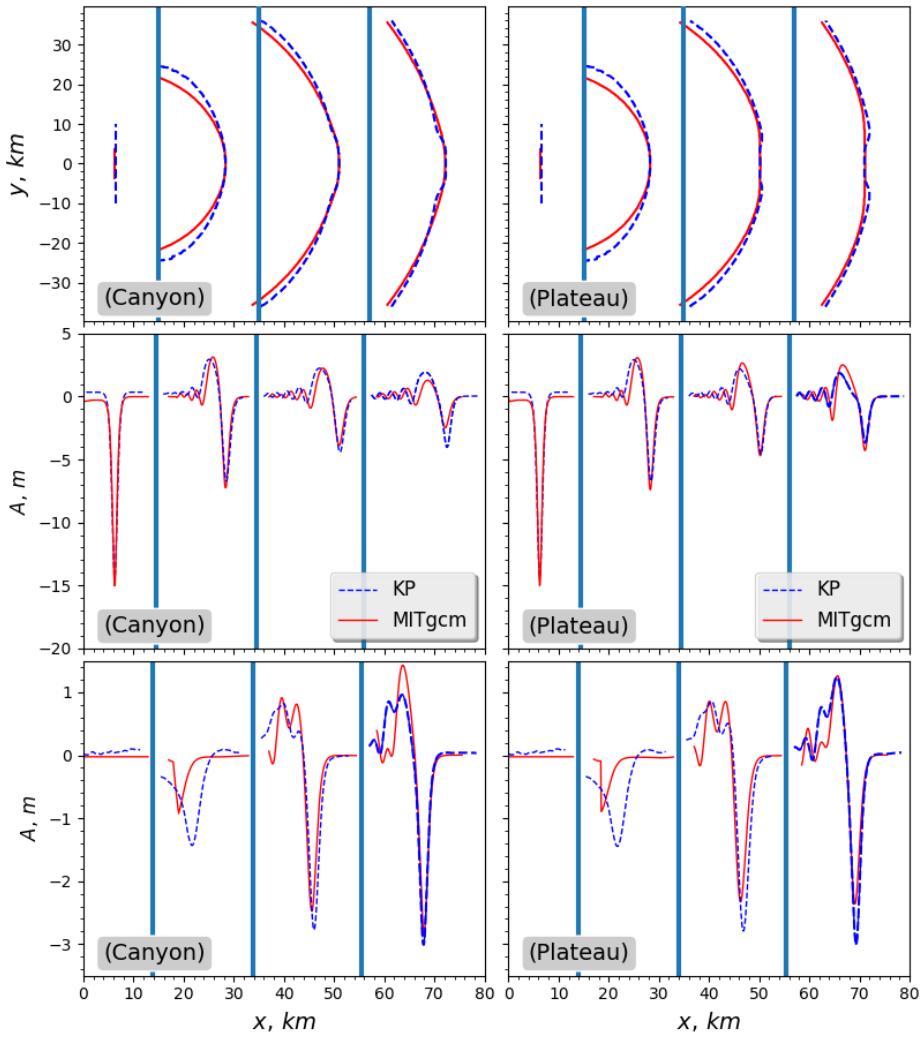

Figure 5.11: The top two panels are the locations of the wavefronts from the MITgcm (solid red lines) and the vKP simulations (dashed blue lines) respectively in the cases of canyon-type and plateau-type topography, shown for times at $t = 0.0$, 5.0, 10.3 and 15.7 hours. Selected at the same times, the comparisons of the wave amplitude A on the central line $y = 0$ and the off-centre section $y = 20\,\text{km}$ along the x-direction are shown in the middle and bottom two panels respectively.

5.4 Conclusion

The vKP model can be widely applied to the real ocean, under the assumption that the y-variations are much slower than those in the propagation x-direction. In the simulations reported here we have considered 2D bathymetry which is either a submarine canyon or a submarine plateau, these being prototypes of more complicated topographic scenarios. For slowly-varying solitary waves, if there are no y-variations, then from the well-known KdV theory the evolution scenarios of ISWs can be expressed by the adiabatic law $a \propto |\nu|^{1/3}$ relating the amplitude a with the nonlinear coefficient ν, assuming that, as here, ν does not change sign. However, when y-variations are taking into consideration, then an additional spreading effect in the y direction, characterised by a propagation speed proportional to $\nu^{1/3}\theta_0^{1/3}(16\tau/3)^{1/2}$ and a diffusion scale $y_d^2/s \sim \tau/(\nu^{2/3}\theta_0^{1/3})$, will also play a crucial role. Our simulations show that this can even be overwhelmingly dominant, depending on the initial conditions, such as in our two cases shown in figure 5.4. But when the initial KdV solitary wave is y-independent in the flat bottom region before the topographic slope, then a very complicated scenario of evolution occurs, which can be explained by the asymptotic theory of the slowly varying solitary wave, combined with the creation of a trailing shelf induced by mass conservation in the X direction.

For the submarine canyon-type and plateau-type bathymetries, the essential dynamics are controlled by the transformed coefficients ν and τ, representing the effects of nonlinearity and transverse diffraction, respectively. For the simulations reported here, we have found that the former is the more effective. We have developed an asymptotic theory of a slowly varying solitary wave which can be used to examine the effect of y-variations in these coefficients. In particular we have found that the nonlinear phase speed W (5.2) has a tendency to oppose the change of the corresponding linear phase speed c due to the y-variations in the topography, although the nonlinear correction term $W\lambda$ is too small to fully compensate the change in c,

as the ratio is typically $\mathcal{O}(10^{-1})$. That is the phase speed (in the physical space) $c_{sol} \approx c(1 + W\lambda)$ is essentially determined by c. Further, we have found very good agreement between the vKP simulations and simulations using the MITgcm model, both qualitatively and quantitatively.

Chapter 6

Topographic effect on oblique internal wave-wave interactions

As introduced at Chapter 1, in the coastal ocean, internal waves sourcing from different generation sites can have an oblique interaction. In addition, due to the variable topographic features, refraction and diffraction can also occur, which also facilitates the emergence of oblique internal wave-wave interactions. For example, at the periphery of Dongsha Atoll in the South China Sea, very complicated internal wave-wave interactions were recorded by satellite images, see figure 1.4 and figure 6.1. It is conceivable that in the ocean, oblique interactions between several internal waves can occur, however we contend that the basic interactions between two internal solitary waves need to be first deeply understood, as the investigations on oblique internal wave-wave interactions are not common, although we note that Xue et al. [111], Wang and Pawlowicz [107], Chen et al. [19], Shimizu and Nakayama [96]. In this chapter, the attention is given to the topographic effect on oblique interactions between two internal solitary waves, in which the theories developed in Chakravarty and Kodama [16, 17, 18] were applied to study three cases, each with a different pair of wave amplitude and oblique angle, given the observations in Xue et al. [111], Wang and Pawlowicz [107], Chen et al. [19].

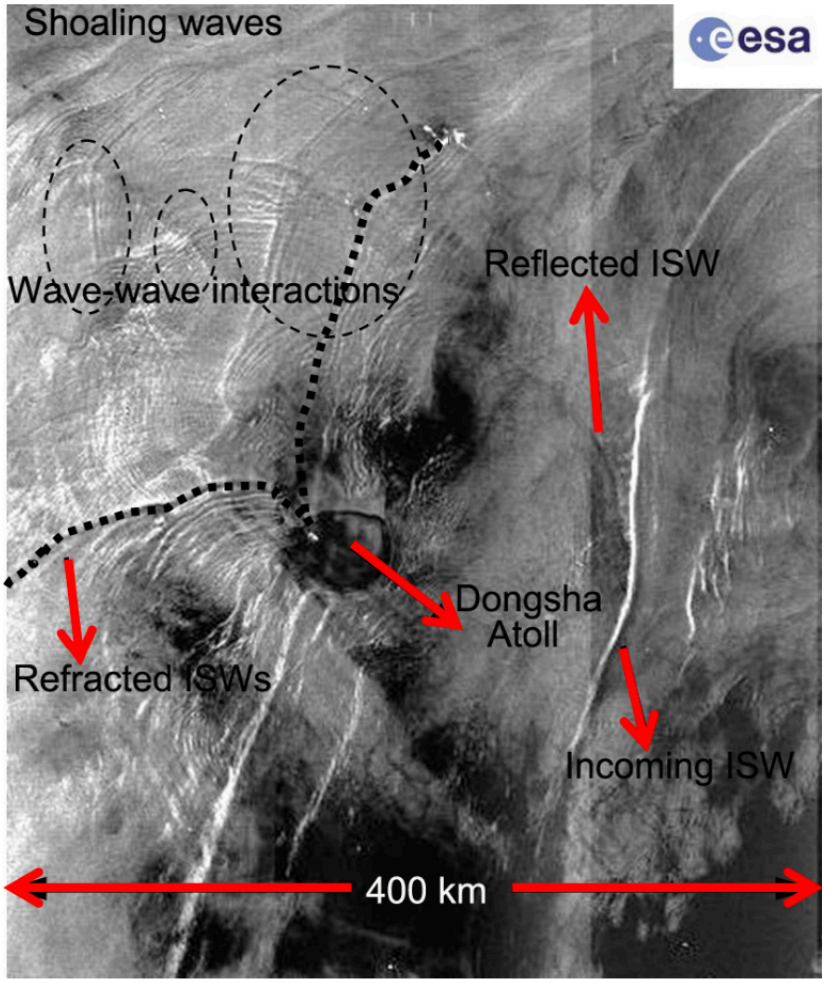

Figure 6.1: The complicated wave field recorded by an Envisat Advanced SAR image on 14:15 UTC, 03-NOV-2005. [Figure adopted from Guo and Chen [48].]

The analyses are based on a variable-coefficient Kadomtsev-Petviashvili (vKP) equation. Following equation (2.18) in Chapter 2, the vKP equation is written in the transformed space as

$$\{U_s + \nu U U_X + U_{XXX}\}_X + \tau U_{yy} = 0\,. \tag{6.1}$$

6.1 Initial condition

First we consider the case of constant topography and a horizontally uniform background so that $\nu = \nu_0\,, \tau = \tau_0$ are constants in the vKP equation (6.1), namely,

$$[U_s + \nu_0 U U_X + U_{XXX}]_X + \tau_0 U_{yy} = 0\,. \tag{6.2}$$

It can be further transformed to the canonical form,

$$[4\Lambda_\vartheta + 6\Lambda\Lambda_\xi + \Lambda_{\xi\xi\xi}]_\xi + 3\Lambda_{YY} = 0\,, \tag{6.3}$$

$$\vartheta = Rs\,, \quad X = L\xi\,, \quad y = MY\,, \quad U = P\Lambda\,, \tag{6.4}$$

$$\text{where} \quad R = \frac{L^3}{4}\,, \quad L^2 = M^2 = \frac{3}{\varkappa_0}\,, \quad P = \frac{2\varkappa_0}{\mu_0}\,. \tag{6.5}$$

From the work of Chakravarty and Kodama [16, 17, 18], the KP equation (6.3) admits multi-soliton solutions which feature an arbitrary number of asymptotic line solitons in the far-field and a complex wave structure formed by the interactions between intermediate solitons in the near-field. One of the advantages of these solutions is they can be constructed through measuring certain characteristics of the given wave pattern, including but not limited to the number of line solitons in the far-field ($Y \gg 0$ and $Y \ll 0$), the amplitude and slope of each line soliton. Chakravarty and Kodama [18] applied this method to the construction of an observed surface wave

interaction pattern and Yeh and Li [114] made a realisation of a variety of these KP soliton formations in the laboratory. Now we will briefly introduce this theory, in which the solution of equation (6.3) can be represented by

$$\Lambda(\xi, Y, \vartheta) = 2(\ln \varphi)_{\xi\xi}\,, \tag{6.6}$$

where the φ-function $\varphi(\xi, Y, \vartheta)$ is defined as the Wronskian of N functions $f_1, \cdots, f_N$, each of which satisfy the linear equations, $f_Y = f_{\xi\xi}$, $f_\vartheta = -f_{\xi\xi\xi}$, and can further be expressed as a sum of exponential functions

$$f_n = \sum_{m=1}^{M} a_{nm} \exp(\theta_m)\,, \quad \theta_m = \sigma_m \xi + \sigma_m^2 Y - \sigma_m^3 \vartheta\,, \quad n = 1, 2, \ldots, N\,. \tag{6.7}$$

This depends on $M > N$ real parameters, ordered as $\sigma_1 < \cdots < \sigma_M$, and the constant coefficients a_{nm} form an $N \times M$ matrix $\mathbb{A}$, all of whose $N \times N$ minors must be non-negative to ensure the non-singularity of the solution (6.6). In general, this solution consists of N line-solitons as $Y \gg 0$ and $M - N$ line-solitons as $Y \ll 0$. For example, the pattern labelled by (c) in figure 6.2 can be interpreted as the case with $M = 3$, $N = 1$.

The solution containing only one soliton is defined by $M = 2$, $N = 1$, so that

$$\varphi = \exp(\theta_1) + a \exp(\theta_2)\,, \tag{6.8}$$

where $a > 0$ is a free parameter which determines the location of the soliton. Without changing the value of Λ in equation (6.6), this can be recast to the following form,

$$\varphi = 1 + a \exp(\theta_2 - \theta_1)\,. \tag{6.9}$$

Then substituting (6.9) into (6.6) we have

$$\begin{aligned}
&\Lambda = \Lambda_0 \operatorname{sech}^2\left(\frac{\Phi+\Phi_0}{2}\right),\\
&\Lambda_0 = \frac{k^2}{2} = \frac{1}{2}(\sigma_2-\sigma_1)^2\,, \quad \Phi = \theta_2-\theta_1 = k\xi + lY - \omega\vartheta\,, \quad \exp\Phi_0 = a\,,\\
&k = \sigma_2-\sigma_1\,, \quad l = \sigma_2^2-\sigma_1^2\,, \quad 4\omega k = k^4+3l^2\,,
\end{aligned} \tag{6.10}$$

where Λ_0 is the wave amplitude, while Φ is the phase consisting of the wavenumbers $k\,, l$ in the ξ and Y directions and the frequency ω. There is a phase shift Φ_0 determined by the free parameter $a > 0$ and the choice $a = 1$ places the wave passing through the origin $\xi = Y = 0$ at $\vartheta = 0$. Equation (6.10) can be further written in physical variables,

$$\begin{aligned}
&\Lambda = \Lambda_0 \operatorname{sech}^2\sqrt{\frac{\Lambda_0}{2}}\,(\xi + Y\tan\Psi - C\vartheta + \xi_0)\,,\\
&C = \frac{1}{2}\Lambda_0 + \frac{3}{4}\tan^2\Psi\,, \quad \xi_0 = \frac{\ln a}{\sqrt{2\Lambda_0}}\,,
\end{aligned} \tag{6.11}$$

which yields the well-known KdV solitary wave. It is clear that this solution describes an oblique solitary wave whose crest line has a slope $\tan\Psi$, where the angle Ψ is measured counterclockwise from the Y-axis. This oblique solitary wave is not stationary and it propagates in the positive ξ direction with the phase speed C; its speed in the direction normal to the crest line is $C\cos\Psi$. Note that the soliton (6.11) is defined in the mapping space (6.4) and this translates in equation (6.2) with an amplitude $U = P\Lambda_0$ and an unchanged slope $\tan\Psi$. In practice, usually $P = 2\tau_0/\nu_0 \sim \mathcal{O}(10^2)$, thus the magnitude of Λ_0 is usually small.

Our interest here is in the 2-soliton interactions which can be constructed from (6.6, 6.7). It was shown by Chakravarty and Kodama [16, 17, 18] that one distinct type arises when $M = 3, N = 1$ or 2; one when $M = 4, N = 1$ or 3 and when $M = 4, N = 2$ there are seven distinct cases that can occur. Here "distinct" means they cannot be obtained from another such solution through an inversion of symmetry,

such as $(\xi, Y, \vartheta) \to (-\xi, -Y, -\vartheta)$. Taking account of this theory and the observed two-ISWs interactions in the ocean, we select a V-shape wave consisting of two oblique ISWs as the initial condition for the KP equation (6.1) and (6.2), that is

$$\begin{aligned} U(X, y, s = 0) &= U_1^0(X, y) + U_2^0(X, y)\,, \\ U_1^0 &= U_1 H(y) \operatorname{sech}^2 \sqrt{\frac{U_1}{2}}\,(X - y \tan \Psi_0)\,, \\ U_2^0 &= U_2 H(-y) \operatorname{sech}^2 \sqrt{\frac{U_2}{2}}\,(X + y \tan \Psi_0)\,, \end{aligned} \tag{6.12}$$

where U_1 and U_2 are the amplitudes for the upper ($y > 0$) and lower ($y < 0$) branch respectively, and their counterparts in the mapping space (6.4) are $\Lambda_1 = U_1/P$ and $\Lambda_2 = U_2/P$. Here we have assumed that each branch has the same inclination with angle $\mp\Psi_0$ relative to the y-axis, which is measured counterclockwise. $H(y)$ is the Heaviside step function, defined by

$$H(y) = \begin{cases} 1, & y \geq 0\,, \\ 0, & y < 0\,. \end{cases} \tag{6.13}$$

A similar initial condition was used by Chakravarty and Kodama [17] to study the oblique interaction of surface solitary water waves. More comprehensively, Kao and Kodama [63] gave a detailed numerical description of this initial V-shape condition associated with equation (6.3), and it was found that depending on the wave amplitude and angle the V-shape wave eventually converges (asymptotically) to some of the exact soliton solutions (6.6). Their main possible outcomes of interest to our present application are schematically indicated in figure 6.2. Patterns (a) and (b) can be described by $M = 4, N = 2$ and the solutions are constructed from (6.6, 6.7), which correspond to (2143) and (3142)-type solutions respectively, as in Chakravarty and Kodama [16, 17, 18]. Patterns (c) and (d) correspond to $M = 3$, $N = 1$ and 2 whose respective solutions are (312) and (231)-type. Patterns (e) and (f) are (2341)-

type ($M = 4, N = 3$) and (4123)-type solutions ($M = 4, N = 1$). Note that the pair of patterns (c, d) can be transformed between each other using the inversion from $y \to -y$, and also for patterns (e, f). Pattern (a) in figure 6.2 was initially investigated by Miles [79], who found the phase shift, while patterns (c) and (d) are resonant interactions as Miles [80] noted. For pattern (b), a Mach stem arises in the interaction zone. There are no corresponding exact analytical soliton solutions at the critical angle Ψ_c depicted by the green dashed line in figure 6.2 (see Kao and Kodama [63]), although Kodama et al. [65] numerically explored this case and found that the stem length has a logarithmic increase when approaching the critical angle. In practice, the critical angle Ψ_c is related to the magnitude of $\Lambda_{1,2}$, see figure 6.2, which are usually not large, since $P = 2\tau_0/\nu_0 \sim \mathcal{O}(10^2)$. There are six such wave patterns shown in figure 6.2, where the boundaries are given by the relations $\sqrt{2\Lambda_2} + \sqrt{2\Lambda_1} = 2\tan\Psi_0$ (a transition from pattern (a) to (b), green dashed line), $\sqrt{2\Lambda_1} - \sqrt{2\Lambda_2} = 2\tan\Psi_0$ (a transition from pattern (b) to the limiting case (c), thick line) and $\sqrt{2\Lambda_2} - \sqrt{2\Lambda_1} = 2\tan\Psi_0$ (a transition from pattern (b) to he limiting case (d), thin line). Patterns (a-c) are more often recorded for internal waves in the ocean, see Chen et al. [19], Wang and Pawlowicz [107], Xue et al. [111], and the SAR image in our figure 1.4. In the subsequent sections we will consider only these three cases.

In the coastal ocean, the along-crest width of the ISWs is mostly in the range from several kilometers to several hundred kilometers, for instance see Chen et al. [19], Wang and Pawlowicz [107], Xue et al. [111]. Then depending on the scale of interest, two scenarios arise; one is when the initial waves fill the whole transverse calculation domain, while the other one is when they are truncated. In our context, for the latter case, the initial V-shape wave (6.12) is confined in a y-direction envelope which equals unity in a specified region $|y| < y_b$ and tapers to zero outside that range,

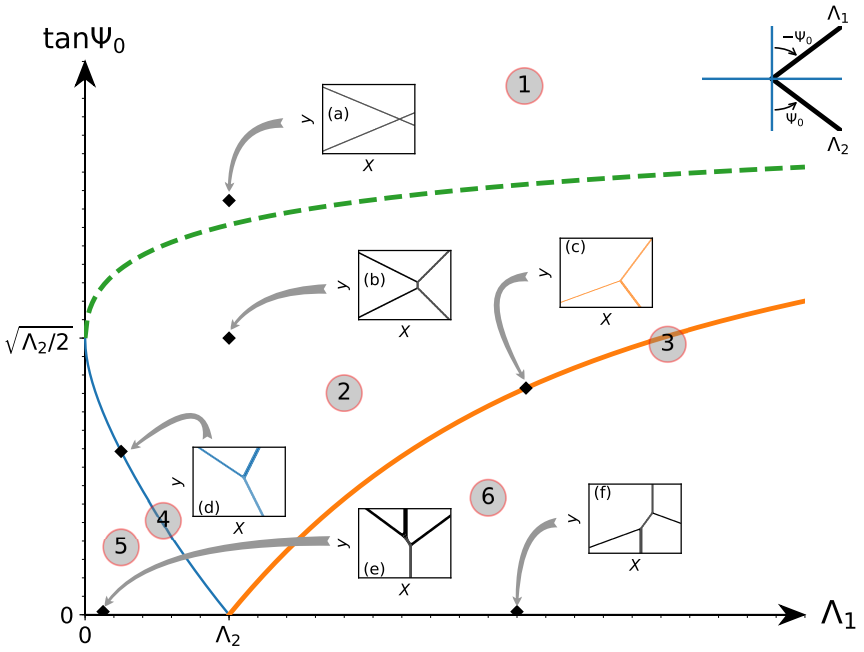

Figure 6.2: The initial V-shape wave (6.12) is depicted in the right upper corner. In the constant-coefficient KP equation (6.3), with the amplitude of the lower branch Λ_2 fixed, the developed wave patterns which evolve corresponding to the amplitude of the upper branch Λ_1 and slope $\tan\Psi_0$ are shown. The evolution regime can be divided into six regions, and specially the region 3 and 4 are just along the thick line (in the colour of orange) and thin line (in blue) respectively. The green dashed line is given by $\sqrt{2\Lambda_1}+\sqrt{2\Lambda_2} = 2\tan\Psi_0$, the thick line is given by $\sqrt{2\Lambda_1}-\sqrt{2\Lambda_2} = 2\tan\Psi_0$, and the thin line is given by $\sqrt{2\Lambda_2}-\sqrt{2\Lambda_1} = 2\tan\Psi_0$.

using an envelope

$$\mathrm{ENV}(y) = \frac{1}{2}\left[\tanh\left(\frac{y+y_e}{y_w}\right) - \tanh\left(\frac{y-y_e}{y_w}\right)\right]. \tag{6.14}$$

We need $y_e \gg y_w$ to ensure a large value of y_b.

6.2 Boundary conditions

An important numerical issue is the boundary condition in the y direction. For the case that the initial along-crest width is short relative to the calculation domain, that is with the envelope $\mathrm{ENV}(y)$ (6.14) imposed on the initial wave $U(X, y, s = 0)$

(6.12), two boundary layers are added to the two y boundaries to avoid radiated waves re-entering the calculation domain. Note that in the calculated space (see equation (6.1)), in the X direction, the waves propagate with the nonlinear phase speed $\alpha U/3$ which is usually very small, therefore no boundaries are needed in the X direction considering our relatively short computation time. In contrast, for the case that the initial waves fill the whole transverse domain, we use the window-scheme method, see Schlatter et al. [95], to transform U into a function η which equals to U in the interior but rapidly decays to zero near the boundaries $y = \pm L_y$, that is essentially a decomposition of U,

$$U = \eta + (1 - W)U \quad \text{with} \quad \eta = WU\,, \tag{6.15}$$

where $W(y)$ is the window function defined as

$$W(y) = \exp\left(-a \left|\frac{y}{L_y}\right|^n\right)\,. \tag{6.16}$$

Here we choose two parameters, $n = 95$ and $a = (1.02)^n \ln 10$, analogous to those in Kao and Kodama [63]. This decomposition replaces the aperiodic U with η which can, with exponential accuracy, be taken as periodic in the y-direction. We assume that outside the boundaries $y = \pm L_y$, the solution can be described by a form U_0, that is the initial condition (6.12) but moving with its corresponding phase speed C (6.10). When the background is horizontally uniform, i.e. equation (6.2) governs the system, then this treatment is very accurate. However when variable topography is considered, this treatment will undoubtedly induce numerical errors. In the computations here the transverse length in the y direction is sufficiently large that the central interaction zone is not affected by the boundary values over the times of computation as demonstrated by test computations on larger domains (not shown). The transverse length being large also guarantees that the post-interaction

waves, have no chance to re-enter the domain to contaminate the calculations. Then through the transformation,

$$U = \eta + (1 - W)U_0 \,, \tag{6.17}$$

we recast the variable-coefficient equation (6.1) to the form,

$$\begin{aligned}
&[\eta_s + \nu\eta\eta_X + \eta_{XXX}]_X + \tau\eta_{yy} = G_1(X, y, s) + G_2(X, y, s) \,, \\
&G_1(X, y, s) = -(1 - W)\left[\partial_X\left(U_0 + \nu U_0\partial_X U_0 + \partial_X^3 U_0\right) + \tau\partial_y^2 U_0\right] \,, \\
&G_2(X, y, s) = \nu(1 - W)\partial_X[WU_0\partial_X U_0 - \partial_X(\eta U_0)] + \tau[2(\partial_y W)(\partial_y U_0) + U_0\partial_y^2 W] \,.
\end{aligned} \tag{6.18}$$

Recall that we have assumed U_0 satisfies the vKP equation (6.1) in the boundary layers, thus $G_1 = 0$ and only the term G_2 takes effect. For the horizontally uniform background, the derivation is the same except replacing $\nu(s, y)\,, \tau(s, y)$ with constants $\nu_0\,, \tau_0$.

6.3 Model set-up

The South China Sea (SCS) is very active for ISWs, and there have been many studies there, see for instance Alford et al. [7]. The bathymetry of the SCS is shown in figure 1.4, and it is clear that in the large expanse of the coastal area, the depth is mostly shallower than 500 m. In addition, a lot of complicated internal wave interactions have been recorded there, see for instance the inset of a SAR image. If we choose the northwest direction (prominent wave propagation direction, see Guo and Chen [48]) to be the x axis, then in the coastal area there is no abrupt change of the bathymetry along the y axis. In order to understand the dynamics, in our model an idealised y-independent shoaling topography with depth varying from 500

to 200 m is deployed in a large domain with $x \times y = [0 : 300] \times [-200 : 200]$ km, see figure 6.3. We note that although Yuan et al. [118] in the study of a single internal solitary wave propagating over a slope showed that a small transverse variation of the topography can induce a perceptible transverse modulation of the wave, here we focus on the effect of just one-dimensional variation of the topography on the oblique interaction of two solitary waves.

The background temperature and salinity profiles are the monthly averaged data in the SCS selected in summer from the World Ocean Atlas 2013, see figure 6.4. As mentioned before, observations have confirmed the existence of mode-2 ISWs in the ocean, but nevertheless, here we confine our attention on only mode-1 waves, and consequently ignore any possible energy transfer between modes when wave interactions occur. The corresponding modal function of the vKP equation shown in figure 6.4 indicates that initially the maximum particle displacement occurs at depth $h \approx 190$ m. The negative sign of the nonlinear coefficient ν depicted in figure 6.3 implies that our leading ISWs are always depression waves, and no polarity changes emerge.

As mentioned in the Introduction, although there are a few studies of oblique internal wave interactions in the ocean, in general these investigations were not sufficiently detailed to provide a deep insight into this common but complicated phenomenon, even for the case of a flat topography. Here we use the comprehensive theory of KP solitons developed by Chakravarty and Kodama [16, 17, 18] (briefly described above in section 6.1) to interpret our simulations of ISW interactions both for a constant depth and with a shoaling topography.

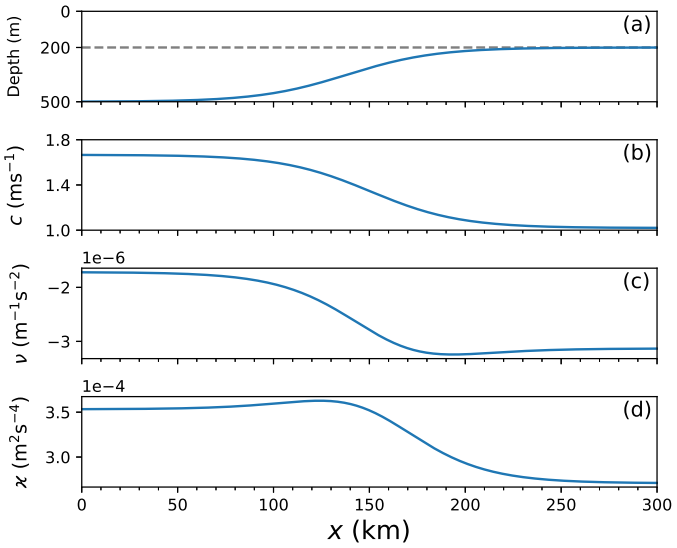

Figure 6.3: The y-independent bathymetry h (a); the linear phase speed c (b); the nonlinear coefficient ν (c); the dispersive coefficient τ (d).

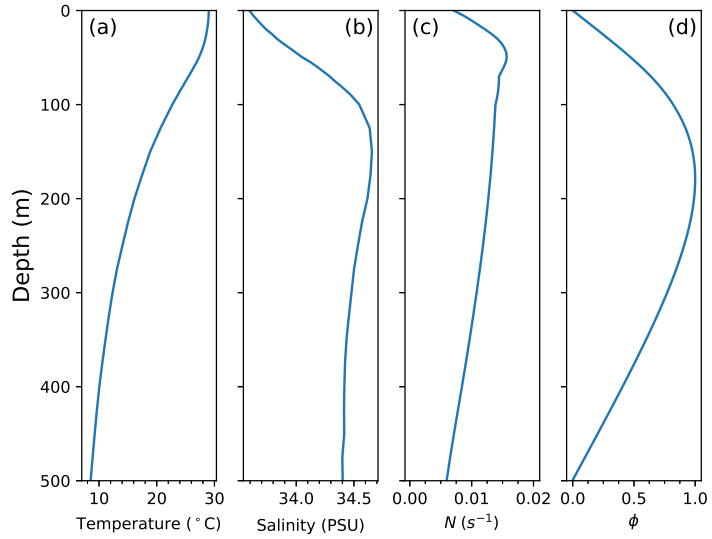

Figure 6.4: The vertical profiles of the temperature (a), salinity (b), buoyancy frequency N (c) and the corresponding mode-1 modal function ϕ (d).

6.4 Experiment 1

We first examine the case, labelled as EXP1, with the initial condition of equal wave amplitudes $A_1 = A_2 = -15\,\mathrm{m}$ for the two branches and the angle $\Psi_0 = 16^\circ$ (larger than the critical angle 15.1°). In a constant depth of $h = 500\,\mathrm{m}$, this set-up is located in region 1 of figure 6.2 and the initial V-shape wave will asympotically evolve to the so-called X-shape wave or O-soliton, see panels (a4-a6) in figure 6.5. Subsequent to the release of the initial depression waves, two small post-interaction depression waves immediately emerge. At the same time, since the mass conservation law (2.21) has to be satisfied, waves with the opposite polarity (here elevation) are generated at the rear of the leading waves, see panel (a5). Then as the solution evolves, the post-interaction waves mature and eventually an X-shape wave emerges followed by a parabolic-shaped trailing wave train of opposite polarity, see panel (a6). A prominent feature of the developed X-shape wave is the phase shift in the interaction zone, also see figure 6.6, which can be interpreted through the analyses based on equation (6.3) in the transformed space (6.4). Adapting from Chakravarty and Kodama [16, 17, 18], the φ-function of the matured X-shape wave for the constant-coefficient equation (6.3) is represented by

$$\varphi = 1 + \exp\left(-\Phi_1\right) + \exp\left(-\Phi_2\right) + B_{12}\exp\left(-\Phi_1 - \Phi_2\right), \tag{6.19}$$

$$\Phi_{1,2} = k_{1,2}\xi + l_{1,2}Y - \omega_{1,2}\vartheta\,, \quad k_{1,2} = \sigma_{2,4} - \sigma_{1,3}\,, \quad l_{1,2} = \sigma_{2,4}^2 - \sigma_{1,3}^2\,, \quad 4\omega_{1,2}k_{1,2} = k_{1,2}^4 + 3l_{1,2}^2\,, \tag{6.20}$$

$$B_{12} = \frac{\Upsilon^2 - (k_1 - k_2)^2}{\Upsilon^2 - (k_1 + k_2)^2}\,, \quad \Upsilon = \frac{l_1}{k_1} - \frac{l_2}{k_2}\,, \tag{6.21}$$

where the parameters have been chosen to make the phase shift of the initial incident wave to be zero. To examine this wave pattern, we take the asymptotic limits $\xi \to \pm\infty$, similar to the procedure used by Miles [79]. Note that the incident 1-

soliton solutions can be obtained by letting $\xi \to +\infty$ with either Φ_1 or Φ_2 fixed. The former limit yields one 1-soliton (6.10) with phase Φ_1 and $\Phi_0 = 0$, and the latter limit gives the other 1-soliton (6.10) with phase Φ_2 and $\Phi_0 = 0$. After the interaction, we let $\xi \to -\infty$ with either Φ_1 or Φ_2 fixed again. The former choice yields the 1-soliton solution (6.10) with phase Φ_1 and $\Phi_0 = \log B_{12}$, while the latter choice yields (6.10) with phase Φ_2 and $\Phi_0 = \log B_{12}$. This implies that the incident solitons emerge unchanged but with a phase shift in the ξ-direction of $\Delta_{1,2}$ where $\exp(k_{1,2}\Delta_{1,2}) = B_{12}$. Since $B_{12} > 0$ to ensure the existence of the solution, the phase shifts can be positive or negative according to $B_{12} > 1$ or $0 < B_{12} < 1$. Since in our case the amplitudes A_1, A_2 are equal, the phase shifts are the same for the upper and lower branches. In physical variables, the theoretical estimated phase shift is $\Delta_x = 1245\,\mathrm{m}$, slightly smaller than our numerical result $\Delta_x = 1300\,\mathrm{m}$, see figure 6.6. Moreover, using the modified Miles theory due to Yeh et al. [115], Kodama [64], the maximum amplitude occurring at the mid-point of the interaction is given by

$$A_{max} = \begin{cases} (1+\Gamma)^2 A_0, & \text{for} \quad \Gamma < 1\,, \\ \frac{4A_0}{1+\sqrt{1-\Gamma^{-2}}}, & \text{for} \quad \Gamma > 1\,, \end{cases} \tag{6.22}$$

where $\Gamma = \sqrt{P}\tan\Psi/\sqrt{2A_0}$ and $A_0 = A_1 = A_2$. It is clear that at the critical angle Ψ_c where $\Gamma = 1$ depicted by the green dashed line in figure 6.2, the maximum amplitude A_{max} can reach four times the soliton amplitudes A_0, as noted by Miles [79]. The estimated A_{max} is $-45\,\mathrm{m}$ in our case, while the numerical result shows the value of $-43\,\mathrm{m}$, see figure 6.6. The slight discrepancy between them is attributed to the evolution time, which is not quite long enough to let the initial V-shape wave evolve to this 2-soliton solution. Another important point is that during the interaction, the amplitudes of the initial two wave branches are unchanged, and furthermore, for the matured X-shape wave the amplitudes of the two post-interaction waves are the same as those of the initial V-shape wave, see panel (a6) in figure 6.5.

When the effect of the shoaling topography is taken into account, there is a different scenario. In the deep water, the initial wave behaves like its counterpart in the constant case, but with the propagation up the slope, the front parts of the waves first experience the topographic effect, manifested as an increasing amplitude and a decreasing linear phase speed, see panel (a2) in figure 6.5. The total phase speed is composed of the linear phase speed c and the nonlinear phase speed $\alpha AQ^{1/2}/3$, and the latter has an opposite effect to that of the former, albeit the linear phase speed c is dominant, see Yuan et al. [118]. The incident waves begin to bend and tend to be parallel to the shore, with a decrease in the angle Ψ. Note that for this set-up, the critical angle $\Psi_c = 15.1°$, delineated by the green dashed line in figure 6.2, is only a little smaller than the initial angle $\Psi_0 = 16°$. Thus due to the shoaling effect, it is possible that the evolution regime transfers from region 1 to region 2 in figure 6.2. Then the X-vertex wave is replaced by a merged front, called the Mach stem following Miles [80], which emerges as a result of the resonant interaction between the upper right branch and the upper left branch, as well as between the lower right and the lower left branch. The length and strength of this merged front are also varying with time. We will give more details in the next section. This whole pattern continues to propagate into the shallow water and the amplitude continues to increase as $|\nu|^{1/3}$ (see figure 6.3 for ν) according the well-known adiabatic law determined by conservation of wave action flux (see for instance Yuan et al. [118]), and meanwhile the mass of the leading depression wave, proportional to $|\nu|^{-1/3}$, decreases, which results in the emergence of the trailing wave trains with the same polarity due to the mass conservation law (2.21). In the simulation, at least one trailing wave pattern with the same polarity as the leading waves is generated. But afterwards the y-dependence has to be taken into account and the adiabatic law fails.

Figure 6.6 shows the wave amplitude of the leading wave at the center $y = 0$, and eventually it is more than four times larger than the initial wave. Note that as Tsuji

and Oikawa [102] pointed out, the resonance and hence the amplification of the wave amplitude at the mid-point of the interaction can be suppressed to some extent when it approaches a critical depth where the quadratic coefficient ν approaches zero. From panel (a3) in figure 6.5, we see that the interaction zone does not have much influence on the evolution of the initial two branches, which still behave approximately like the adiabatic shoaling process predicted by the KdV theory. In contrast, the evolution of the post-interaction waves are highly affected by the interaction, see panel (a3). The post-interaction waves adjacent to the interacted merged front have a relatively smaller amplitude compared with the neighbouring waves along the wave crest. This could be due to the conservation of the wave action flux, since around the junction of the merged front and the post-interaction waves, a large y-gradient is needed to compensate the increase of the energy induced by the increasing amplitude. This indicates the failure of the KdV adiabatic law. After the waves propagate onto the flat shelf, the linear phase speed is the same for all waves, however the nonlinear phase speed $\alpha A Q^{1/2}/3$ is dependent on the wave amplitude, so the post-interaction wave branches will be curved with the larger waves moving faster.

6.5 Experiment 2

Next we set the initial wave amplitudes $A_1 = A_2 = -20\,\mathrm{m}$ and the angle $\Psi_0 = 8^\circ$ (smaller than the critical angle 17.3°), which is pattern (b) in figure 6.2 in the constant depth $h = 500\,\mathrm{m}$ water; this set-up is labelled as EXP2. At the initial stage, the evolution is almost the same as in EXP1, which is partly characterised by the radiation of two post-interaction waves and a parabolic-shaped wave train of opposite polarity. The essential difference is the generation of a Mach stem in the middle of the initial two wave branches and its length is increasing with time. Eventually the pattern asymptotically converges to the (3142)-type solutions in Chakravarty and

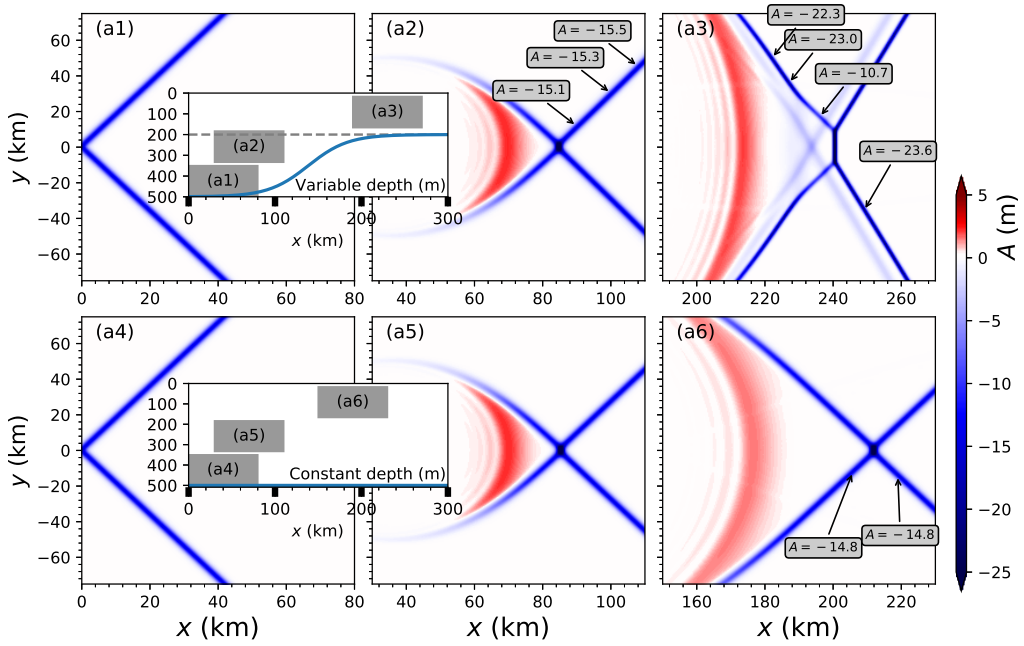

Figure 6.5: For EXP1, panels (a1-a3) are selected to exhibit the evolution of wave patterns in the case of shoaling topography at times $t = 0$, 12, 42 hours respectively. In contrast, panels (a4-a6) are for the case of constant topography at times $t = 0$, 12, 30 hours respectively. Note that as the waves propagate faster in the constant-depth case, so the snapshot is not an exact one-to-one match. The aspect ratio of every panel is the same, that is $x \times y = 80 \times 150\,\text{km}$, and the corresponding depth of every panel is indicated by insets.

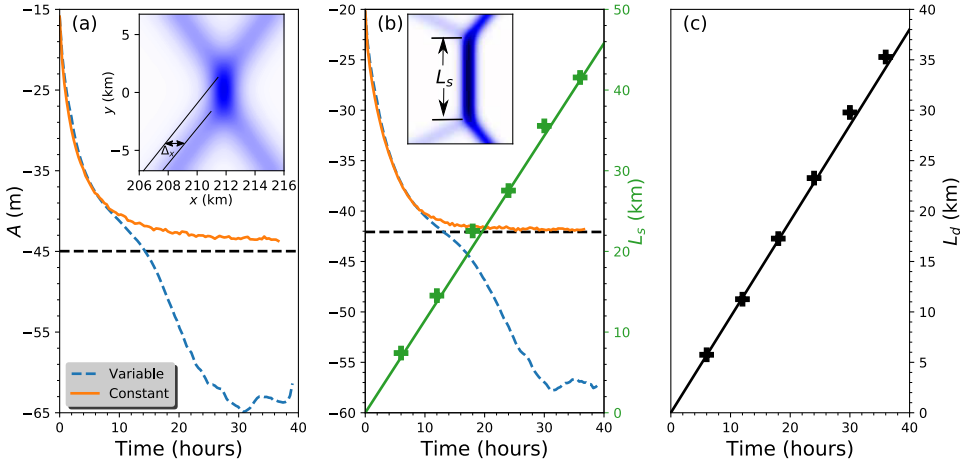

Figure 6.6: (a) In EXP1, the time series of the leading wave amplitude along $y = 0$ for the cases of both varying and constant topography. The inset is a zoom-in of panel (a6) in figure 6.5. (b) In EXP2, the time series of the leading wave amplitude along $y = 0$ for the cases of both varying and constant topography. The inset is a zoom-in of panel (b6) in figure 6.7. The other scale shows the length of the intermediate Mach stem L_s predicted by the theory (green solid line) and the numerical simulations (green plus sign). (c) The downward distance L_d varying with time in EXP3 is shown and the solid line is the theoretical result, while the plus sign is from numerical simulations.

Kodama [16, 17, 18]. The φ-function in the transformed space (6.4) is given by

$$\varphi = E(1,3) + bE(1,4) + aE(2,3) + abE(2,4) + cE(3,4)\,, \tag{6.23}$$

where $E(i,j) = (\sigma_j - \sigma_i)\exp(\theta_i + \theta_j)$, the phase θ_n, $n = 1,2,3,4$ is defined in equation (6.7), and $a, b, c > 0$ are parameters which determine the location of the solitons. Using the same method of asymptotic limits introduced before, when $\xi \to +\infty, Y \to +\infty$, the soliton, see analogously the right upper branch in figure 6.7, can be obtained from the balance between the terms $bE(1,4)$ and $cE(3,4)$, which yields the 1-soliton solution (6.10) with the amplitude $\Lambda_{13} = (\sigma_3 - \sigma_1)^2/2$, the phase $\Phi_{13} = \theta_3 - \theta_1$ and the phase shift

$$\Phi_{013} = \ln\left\{\frac{(\sigma_4 - \sigma_1)}{(\sigma_4 - \sigma_3)}\frac{b}{c}\right\}. \tag{6.24}$$

Similarly, when $\xi \to +\infty, Y \to -\infty$ (the right lower branch), the soliton is given by expression (6.10) with the amplitude $\Lambda_{24} = (\sigma_4 - \sigma_2)^2/2$, the phase $\Phi_{24} = \theta_4 - \theta_2$ and the phase shift

$$\Phi_{024} = \ln\left\{\frac{(\sigma_3 - \sigma_2)}{(\sigma_4 - \sigma_3)}\frac{a}{c}\right\}. \tag{6.25}$$

On the other hand as $\xi \to -\infty$ the dominant terms in (6.23) are either the pair $E(1,3), E(1,4)$ yielding a 1-soliton with the amplitude $\Lambda_{34} = (\sigma_4 - \sigma_3)^2/2$ and the phase $\Phi_{34} = \theta_4 - \theta_3$ (the left upper branch) or the pair $E(1,3), E(2,3)$ yielding a second 1-soliton with the amplitude $\Lambda_{12} = (\sigma_2 - \sigma_1)^2/2$ and the phase $\Phi_{12} = \theta_2 - \theta_1$ (the left lower branch). They have the respective phase shifts

$$\Phi_{034} = \ln\left\{\frac{(\sigma_3 - \sigma_1)}{(\sigma_4 - \sigma_1)}\frac{1}{b}\right\}, \quad \Phi_{012} = \ln\left\{\frac{(\sigma_3 - \sigma_1)}{(\sigma_3 - \sigma_2)}\frac{1}{a}\right\}. \tag{6.26}$$

Importantly, the total phase shift is locked for all values of $a, b, c > 0$, as Miles [79] pointed out,

$$\Phi_{013} + \Phi_{034} = \Phi_{024} + \Phi_{012}\,. \tag{6.27}$$

The generation of the Mach stem is a consequence of the resonance between the upper right branch and the upper left branch, as well as between the lower right and the lower left branch. Note that the Mach stem can be represented by the soliton solution (6.10) with the amplitude $\Lambda_{14} = (\sqrt{2\Lambda_0} + \tan\Psi_0)^2/2$ and the phase $\Phi_{14} = \theta_4 - \theta_1$. Then the length of the stem L_s can be expressed as $L_s = (\sqrt{2\Lambda_0} - \tan\Psi_0)\vartheta$, which is obtained by examining the location of the intersection point between the stem and the initial upper left branch.

Since in the present case, the amplitudes of the initial two branches are the same, that is $\Lambda_{13} = \Lambda_{24} = A_0/P$ where $A_0 = A_{1,2}$, and the initial wave passes through the origin $\xi = Y = 0$ at time $s = 0$, the phase shift $\Phi_{013} = \Phi_{024} = 0$, which fixes two values from a, b, c and only one free parameter is left. In the physical space, through the transformation (2.14), the estimated amplitude of the post-interaction wave is

-4 m, matches well with the numerical result, see panel (b6) in figure 6.7. The length of the stem L_s is shown in panel (b) of figure 6.6, and there is a remarkable agreement between the theory and numerical simulations. In addition, from equation (6.22), the amplification factor (relative to the initial wave amplitude) is $(1+\Gamma)^2 = 2.1$ since $\Gamma = 0.45 < 1$, and again a very good consistency with the numerical results, see figure 6.6.

The evolution scenario over the shoaling topography is similar to that in EXP1, except for the evolution of the intermediate Mach stem. As the solution evolves, the amplitude of the stem is not constant either along y-sections or along the stem itself, in contrast to the eventual constant amplitude in the flat bottom case. Figure 6.6 shows the increasing amplitude of the leading wave along $y = 0$. The magnification of the wave amplitude in the interaction zone is not as efficient as that in EXP1, since here it increases approximately once, smaller than the twice in EXP1. Note that here the varying topography is y-independent, thus any transverse effect must enter the equation through the spreading term τU_{yy} in the vKP equation (6.1). Since the two initial wave branches are oblique, the front parts experience the topographic effect and consequently deform earlier than the rear parts. Then this discrepancy along the branches induces a complicated modulation in both the X direction due to the mass conservation law and further in the y direction to respond to the variations in the X direction, as the wave action flux must be conserved. From panel (b3) in figure 6.7, we find that the stem has a very special structure. As we mentioned before, in general, the waves with larger amplitude propagate faster, however panel (b3) shows that along the stem, the wave at $y = 0$ section with smaller amplitude surprisingly propagates faster than its larger neighbouring waves. This indicates a profound topographic effect on wave-wave interactions. Also note that after time $t = 42$ h (see panel (b3)), the whole wave pattern will propagate onto the flat shelf, and if the flat shelf is long enough, then the stem is likely to become parallel to the

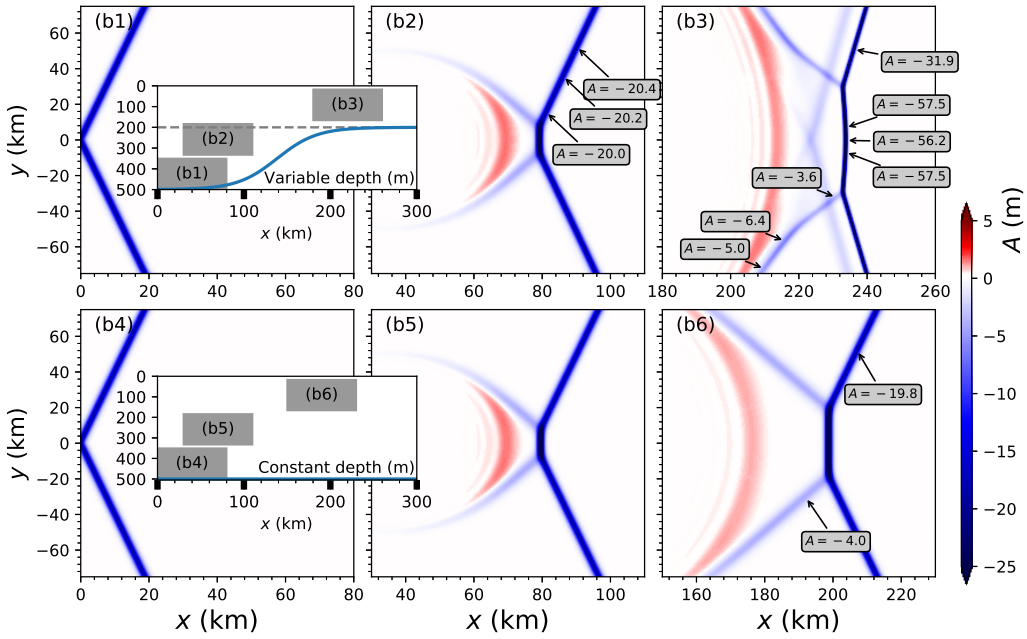

Figure 6.7: The layout is the same as in figure 6.5, but for EXP2.

shore. However, we are not able to verify this here , as our computational domain is not sufficiently long.

6.6 Experiment 3

In EXP2, in the case of constant depth, we showed that the resonant interaction between the initial wave and the post-interaction wave generated a third wave (Mach stem). In this section, we will examine this further. In figures 6.2, patterns (c) and (d) have the same dynamical features, both of which need two initial branches with different amplitudes. Here we select pattern (c) with the initial condition $A_1 = -25\,\mathrm{m}$, $A_2 = -10\,\mathrm{m}$, and the angle $\Psi_0 = 3.67°$ satisfying the critical relation $\sqrt{2\Lambda_1} - \sqrt{2\Lambda_2} = 2\tan\Psi_0$ (the thick line in figure 6.2). This case is labelled as EXP3. Note that as shown in our figure 1.4 and also in Chen et al. [19], this pattern has been observed in the SCS. Here the φ-function of the developed wave pattern, see panel

(c6) in figure 6.8, is

$$\varphi = 1 + \exp(-\Phi_1) + \exp(-\Phi_2)\,. \tag{6.28}$$

As $\xi \to +\infty$, this describes two incident solitons with respective phases as defined in (6.20). But as $\xi \to -\infty$, this describes the generation of a third resonant soliton with phase $\Phi_3 = k_3 x + l_3 y - \omega_3 t$, where k_3, l_3, ω_3 satisfy the resonance conditions,

$$\begin{aligned} &\omega_3 = \omega_1 - \omega_2\,, \quad k_3 = k_1 - k_2\,, \quad l_3 = l_1 - l_2\,, \\ &4\omega_i k_i = k_i^4 + 3l_i^2\,, \quad i = 1, 2, 3\,. \end{aligned} \tag{6.29}$$

Upon noting that $\Phi_3 = \Phi_1 - \Phi_2$, fixing Φ_3 and taking the limit $\xi \to -\infty$ yields

$$\tau \sim 1 + \exp(-\Phi_3)\,, \quad u \sim \frac{k_3^2}{2}\operatorname{sech}^2\left(\frac{\Phi_3}{2}\right)\,. \tag{6.30}$$

Thus the amplitude of the third wave is $k_3^2/2$, which is $-3.4\,\mathrm{m}$ using our physical variables, very close to the numerical result $-3.3\,\mathrm{m}$, see panel (c6) in figure 6.8. From equation (6.11), the propagation speed is related to the amplitude and angle. In this set-up two branches are of the same inclination but different initial amplitudes, and it follows that the intersection point will move downward with respect to $y = 0$ based on a simple geometric relation. In the transformed space (6.4), the downward distance is

$$L_d = \frac{(\Lambda_2 - \Lambda_1)s}{4\tan\Psi_0}\,, \tag{6.31}$$

which is confirmed by our numerical simulations shown in the physical space, see figure 6.6.

It is clear that in this case, there are no mechanisms that can boost the amplitude at the intersection point, which is different from the previous two cases. When the topographic effect is considered, as before, a wave train of opposite polarity, together with a second wave pattern with the same polarity, follows the leading wave

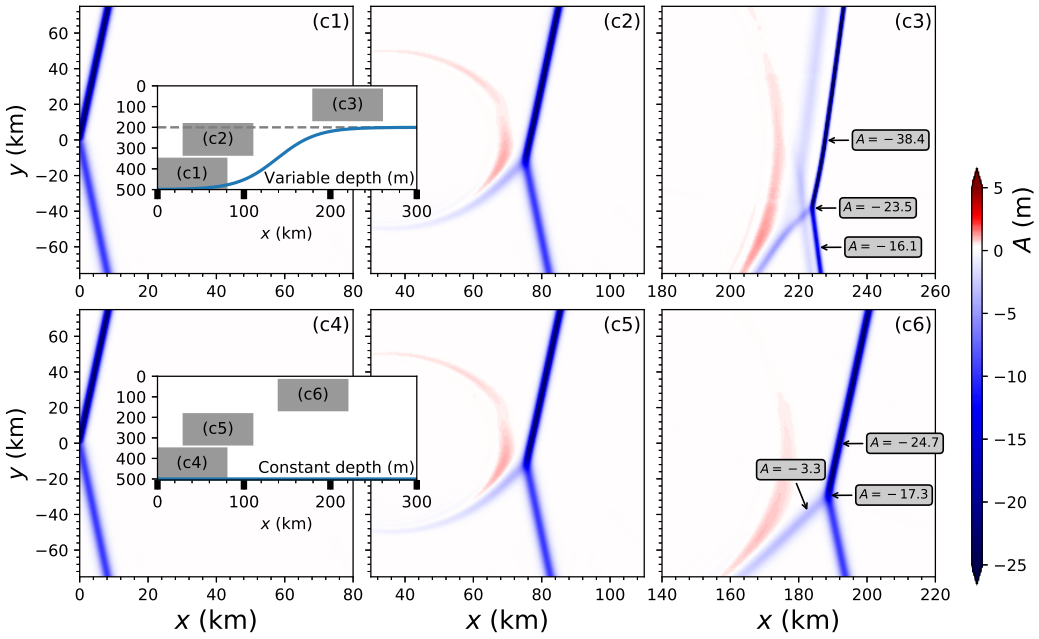

Figure 6.8: The layout is the same as in figure 6.5, but for EXP3.

pattern, see panel (c3) in figure 6.8. In addition, in panel (c3), the curvature of the leading two wave branches is perceptible. Note that the absence of a resultant large-amplitude intermediate wave in the interaction zone seems to suppress the transverse modulation, which suggests that the evolution can be partly predicted by KdV theory, see for instance Grimshaw et al. [42, 43].

6.7 Short along-crest width

The aforementioned cases are such that the initial waves fill the whole transverse domain and indeed this set-up can be of some practical interest. In a realistic ocean, although the along-crest width can be as long as several hundred kilometres, in some circumstances, it is permissible to focus only on central parts, where the effect induced by the wave edges is considered unimportant. Nevertheless, since the real ocean can be regarded as open for ISWs, the case in which waves can propagate freely in the transverse direction should also be examined, which amounts here to

considering a wave with a short along-crest width propagating in a large domain. In this sub-section we will examine this issue. The set-ups are the same as those in the previous three cases, except that a y-envelope ENV(y) (6.14) is imposed on the initial wave. Figures 6.9-6.11 show the evolution scenarios. For each figure, the horizontal view is quite similar qualitatively, which is presumably indicative of the significance of the spreading effect in the transverse direction. However closer scrutiny shows that topographic effect does still modulate the amplitude of the waves.

We consider the case of constant water depth first. After the initial launch, similar post-interaction waves and their consequent trailing opposite wave trains emerge just as in EXP1-EXP3. However, here due to the spread in the y direction, then another pair of wave trains of opposite polarity arises behind the two leading branches as a consequence of mass conservation. Note that the dispersion relation of the KP equation (6.3) for a linear wave $\Phi = \exp(ik\xi + ilY - i\omega\vartheta)$ with frequency ω and wavenumbers k, l is given by

$$\omega = -\frac{k^3}{4} + \frac{3l^2}{4k}\,, \tag{6.32}$$

from which the group velocity of the wave is

$$C_{g\xi} = -\frac{3}{4}\left(k^2 + \frac{l^2}{k^2}\right)\,, \quad C_{gY} = \frac{3l}{2k}\,. \tag{6.33}$$

The (always) negative sign of the group speed $C_{g\xi}$ in the ξ direction implies that any small perturbation must propagate in the negative ξ direction. Thus in the physical space, any generated small-amplitude wave trains will appear behind the leading waves and gradually detach from them. Then the spreading effect keeps expanding the waves in the y-direction at the cost of decreasing wave amplitude from the periphery gradually up to the centre. As mentioned, the nonlinear phase speed is related to the amplitude, so as a result, overall the initial two oblique waves become parallel to the shore, and eventually they merge into one large leading wave,

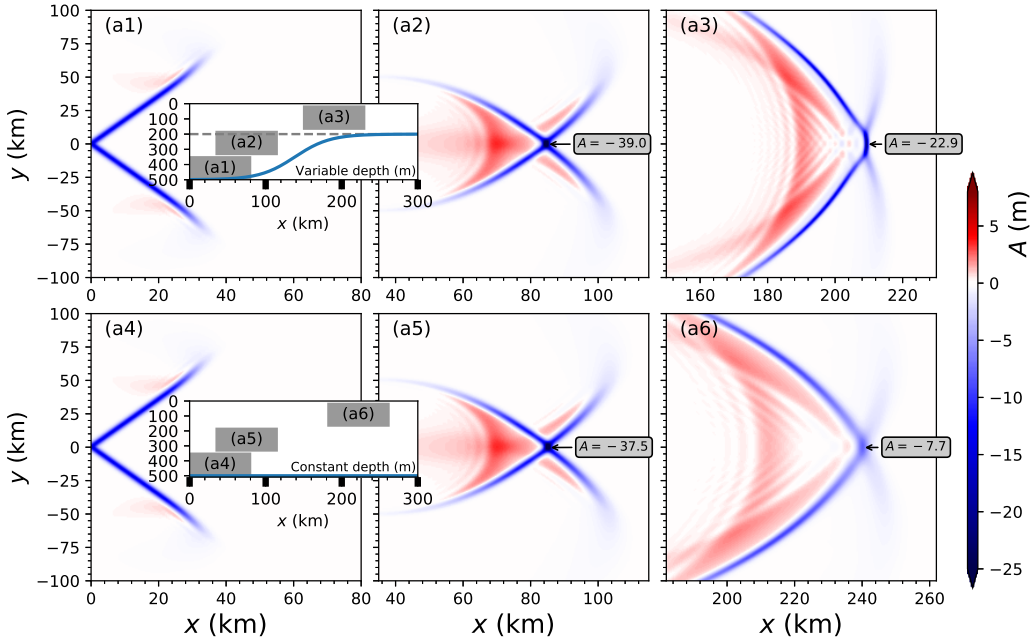

Figure 6.9: The layout is the same as in figure 6.5 but the aspect ratio of every panel is $x \times y = 80 \times 200$ km here. The set-up is the same as that in EXP1, except that an envelope is imposed on the initial V-shape wave.

followed by the post-interaction waves and wave trains of opposite polarity. This wave pattern continues to propagate, but the spreading effect radiates the energy away from the calculation domain.

When the topographic effect is taken into consideration, the spreading effect is still dominant, but at the same time, the amplitude is enlarged by the shoaling process, compared with that in the constant water depth. Especially, the difference in the eventual merged leading wave in figure 6.9 is appreciable, which can be ascribed to the topographic effect, see also figure 6.5.

6.8 Conclusion

Motivated by the observations reported in Chen et al. [19], Wang and Pawlowicz [107], Xue et al. [111] and many SAR images, we have examined three cases of oblique internal wave-wave interactions using a V-shape wave consisting of two branches of

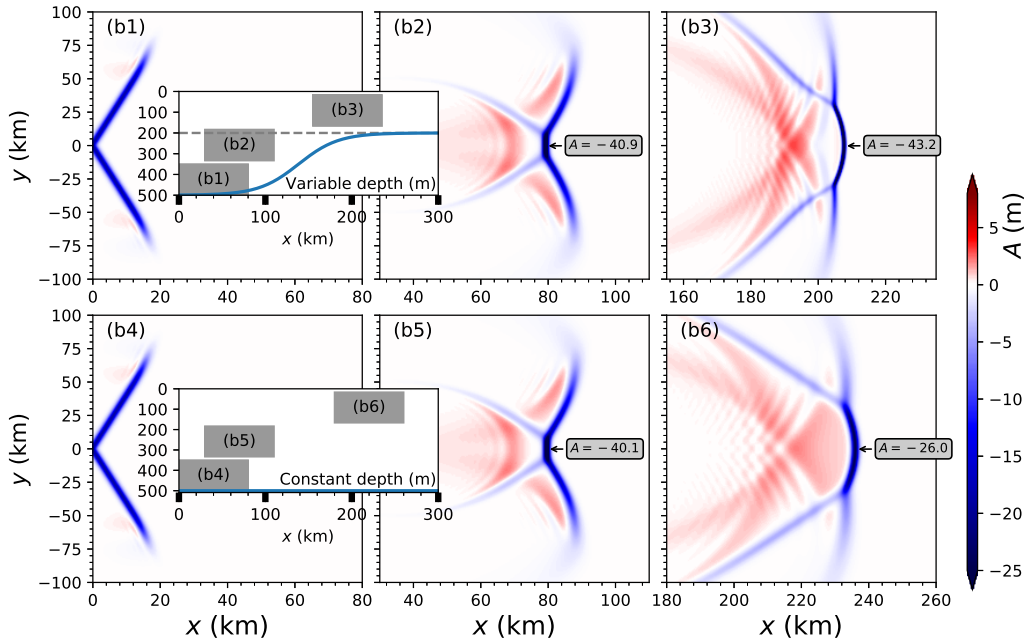

Figure 6.10: The layout is the same as in figure 6.5 but the aspect ratio of every panel is $x \times y = 80 \times 200$ km here. The set-up is the same as that in EXP2, except that an envelope is imposed on the initial V-shape wave.

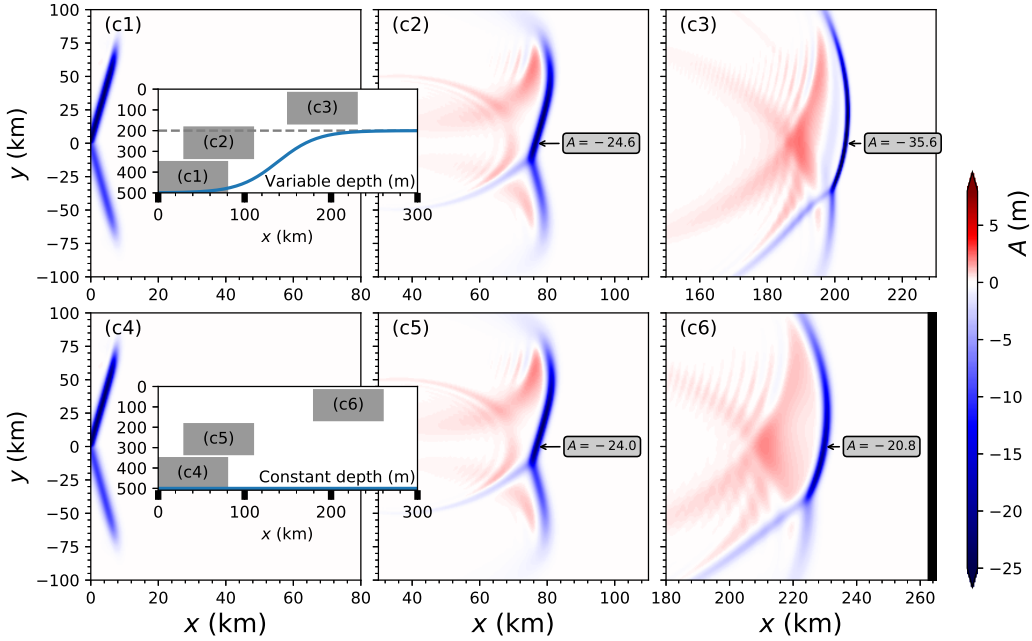

Figure 6.11: The layout is the same as in figure 6.5 but the aspect ratio of every panel is $x \times y = 80 \times 200$ km here. The set-up is the same as that in EXP3, except that an envelope is imposed on the initial V-shape wave.

ISWs as the initial condition.

In constant depth water, when the along-crest width is relatively short compared with the domain of interest, the spreading effect in the transverse direction is dominant, which eventually destroys the initial structure of two oblique waves and leads to the emergence of one merged leading wave followed by wave trains of opposite polarity. However, if we consider the case when the initial waves fill the whole transverse domain, then the evolution scenario can be categorised into six types depending on the amplitude and slope of each wave branch. From these six types, patterns (c) and (d) have the same dynamical feature and so do patterns (e) and (f), see figure 6.2.

Both patterns (a) and (b) contain an intermediate zone characterised by relatively large-amplitude waves and in our specific cases these are three times as large as the initial waves in pattern (a) and twice the initial waves in pattern (b). For pattern (a), there is a phase shift in the interaction zone and this zone is neither expanding nor shrinking with time, while for pattern (b), the intermediate area is an uniform stem whose transverse length is linearly increasing with time. The occurrence of this stem is a superposition of the interaction emerging between upper two wave branches and that arising between lower two waves and this was further examined in pattern (c), in which a third post-interaction wave is apparent.

The effect of shoaling topography modulates the wave field, primarily manifested as augmented leading depression waves followed by parabolic-shaped wave trains of opposite polarity and secondary wave trains of the same polarity, which is induced by mass conservation in the X direction. As waves propagate up the shoaling topography, their phase speeds decrease. Then the front parts of the leading waves undergo the topographic effect earlier than the rear parts, which overall results in decreasing angles of the oblique leading wave branches. This feature can make the evolution pattern move from one region to another as described in figure 6.2. Also,

the post-interaction wave branches have a special structure because the amplitudes and discrepancies along the branches induce curvatures with larger waves propagating faster. When the along-crest width is short, the wave amplitude is amplified by the shoaling process, although the spreading effect in the transverse direction is still dominant, as for constant depth. Since here the generated wave trains are of small amplitude, they can be treated approximately as small linear perturbation. Then the dispersion relation for the KP equation shows that these small perturbations have a negative group velocity in the X direction and detach from the leading waves, which is affirmed by our numerical simulations.

It is clear that for these internal wave-wave interactions, the relationships between amplitude and angle are very significant. We note that the existing observations on this phenomena are mainly from SAR imagery and aerial photography and sometimes it is just one snapshot rather than sequential images. Here we caution that it may not be very reliable to interpret just one observed wave pattern from an instantaneous image, and it is desirable to obtain also information of the whole water column.

Chapter 7

Future possible work

The equations that have been used are of the KdV equation type. However, in a variable medium, when there is a polarity change (the quadratic nonlinear coefficient passes through zero) or the wave amplitude is relatively large, a cubic nonlinear term becomes significant, and this is described by the Gardner equation, also called the extended KdV equation, see for instance Grimshaw et al. [40]. Although the solitary wave solution of this is now well-known, there is still much to study here for undular bores. Note that Esler and Pearce [26] and Kamchatnov et al. [61, 62] have shown that the additional cubic term adds considerable complexity when examining undular bores. Thus the investigation of internal undular bores in the framework of the Gardner equation is quite worthy and challenging.

In Chapter 6, oblique internal wave-wave interactions are investigated. Theoretical and numerical results are provided, but there is a lack of quantitative observational evidence. Since *in-situ* observations are impractical to collect the horizontal 2D information simultaneously and available radar images are snapshots rather than sequential images capturing a relatively complete evolution process, an economic and feasible way is to conduct laboratory experiments and then compare these results with our developed theories. One possible scenario is that there is some energy transfer between different modes, and if that is indeed the case, since the KdV-type

theory is not able to incorporate more than one distinguished mode simultaneously, then either coupled KdV systems or the full Euler equations will need to be invoked.

The KP theory formally requires the variation in the transverse direction is one order weaker than that in the primary direction, which limits its applicability to some practical scenarios. Benney and Luke [11] derived an isotropic equation for water waves of finite amplitude, also see Milewski and Keller [81], which is written as

$$\xi_{tt} - c^2\Delta\xi = \alpha\Delta^2\xi + \beta\left[(|\nabla\xi|^2)_t + \xi_t\Delta\xi\right] , \tag{7.1}$$

where ξ is surface velocity potential, c, α, β are coefficients, $\Delta = \partial_{xx} + \partial_{yy}$ is the two-dimensional Laplacian operator acting on horizontal variables, while ∇ is the gradient operator. This Benney-Luke equation can be reduced to the KdV equation when only uni-directional waves are taken into account, and has the KP equation as a limiting case in nearly uni-directional situations. One advantage is that this equation is isotropic, which makes it suitable for the study of more general two-dimensional wave evolution. However the classic Benney-Luke equation is only for water waves, and hence it is worth deriving a modified Benney-Luke equation for internal waves in which two-dimensional variable topography is also considered. Note that the classic Benney-Luke equation is a Boussinseq-type system, for which there is literature where depth dependence is included, see for example Esler and Pearce [26] and Kamchatnov et al. [61, 62], but these are for one-dimensional topography. In addition, the MCC equation (mentioned in Chapter 1) is an extension of the Benney-Luke equation to interfacial waves, and again only for one-dimensional topography.

Bibliography

[1] Mark J. Ablowitz and Harvey Segur. *Solitons and the inverse scattering transform*. SIAM, 1981.

[2] Mark J. Ablowitz, David J. Kaup, Alan C. Newell, and Harvey Segur. Nonlinear-evolution equations of physical significance. *Physical Review Letters*, 31(2):125, 1973.

[3] Mark J. Ablowitz, David J. Kaup, Alan C. Newell, and Harvey Segur. The inverse scattering transform-Fourier analysis for nonlinear problems. *Studies in Applied Mathematics*, 53(4):249–315, 1974.

[4] T. R. Akylas and R. H. J. Grimshaw. Solitary internal waves with oscillatory tails. *Journal of Fluid Mechanics*, 242:279–298, 1992.

[5] Matthew H. Alford. Internal swell generation: The spatial distribution of energy flux from the wind to mixed layer near-inertial motions. *Journal of Physical Oceanography*, 31(8):2359–2368, 2001.

[6] Matthew H. Alford. Redistribution of energy available for ocean mixing by long-range propagation of internal waves. *Nature*, 423(6936):159–162, 2003.

[7] Matthew H. Alford, Jennifer A. MacKinnon, Jonathan D. Nash, Harper Simmons, Andy Pickering, Jody M. Klymak, Robert Pinkel, Oliver Sun, Luc Rainville, and Ruth Musgrave. Energy flux and dissipation in Luzon Strait:

Two tales of two ridges. *Journal of Physical Oceanography*, 41(11):2211–2222, 2011.

[8] A. Alias, R. H. J. Grimshaw, and K. R. Khusnutdinova. On strongly interacting internal waves in a rotating ocean and coupled Ostrovsky equations. *Chaos*, 23(2):023121, 2013.

[9] A. Alias, Roger H. J. Grimshaw, and Karima R. Khusnutdinova. Coupled Ostrovsky equations for internal waves in a shear flow. *Physics of Fluids*, 26 (12):126603, 2014.

[10] T. Brooke Benjamin. Internal waves of finite amplitude and permanent form. *Journal of Fluid Mechanics*, 25(2):241–270, 1966.

[11] D. J. Benney and J. C. Luke. On the interactions of permanent waves of finite amplitude. *Journal of Mathematics and Physics*, 43:309–313, 1964.

[12] David John Benney. Long non-linear waves in fluid flows. *Studies in Applied Mathematics*, 45(1-4):52–63, 1966.

[13] J. Boussinesq. *Essai sur la théorie des eaux courantes.* Mémoires présentées par divers savants à l'Académie des Sciences. Impr. nationale, 1877.

[14] Joseph Boussinesq. Théorie de l'intumescence liquide appelée onde solitaire ou de translation se propageant dans un canal rectangulaire. *Comptes Rendus Acad. Sci (Paris)*, 72:755–759, 1871.

[15] Shuqun Cai and Jieshuo Xie. A propagation model for the internal solitary waves in the northern South China Sea. *Journal of Geophysical Research: Oceans*, 115(C12), 2010.

[16] Sarbarish Chakravarty and Yuji Kodama. Classification of the line-soliton

solutions of KPII. *Journal of Physics A: Mathematical and Theoretical*, 41 (27):275209, 2008.

[17] Sarbarish Chakravarty and Yuji Kodama. Soliton solutions of the KP equation and application to shallow water waves. *Studies in Applied Mathematics*, 123 (1):83–151, 2009.

[18] Sarbarish Chakravarty and Yuji Kodama. Construction of KP solitons from wave patterns. *Journal of Physics A: Mathematical and Theoretical*, 47(2): 025201, 2013.

[19] Guan-Yu Chen, Cho-Teng Liu, Yu-Huai Wang, and Ming-Kuan Hsu. Interaction and generation of long-crested internal solitary waves in the South China Sea. *Journal of Geophysical Research: Oceans*, 116(C6), 2011.

[20] Wooyoung Choi and Roberto Camassa. Fully nonlinear internal waves in a two-fluid system. *Journal of Fluid Mechanics*, 396:1–36, 1999.

[21] J. C. B. Da Silva, A. L. New, and J. M. Magalhaes. Internal solitary waves in the Mozambique Channel: Observations and interpretation. *Journal of Geophysical Research: Oceans*, 114(C5), 2009.

[22] E. M. de Jager. On the origin of the Korteweg-de Vries equation. *arXiv preprint math/0602661*, 2006.

[23] V. D. Djordjevic and L. G. Redekopp. The fission and disintegration of internal solitary waves moving over two-dimensional topography. *Journal of Physical Oceanography*, 8(6):1016–1024, 1978.

[24] Philip G. Drazin and Robin S. Johnson. *Solitons: an introduction*, volume 2. Cambridge university press, 1989.

[25] G. A. El, Roger H. J. Grimshaw, and Wei K. Tiong. Transformation of a shoaling undular bore. *Journal of Fluid Mechanics*, 709:371–395, 2012.

[26] J. G. Esler and J. D. Pearce. Dispersive dam-break and lock-exchange flows in a two-layer fluid. *Journal of Fluid Mechanics*, 667:555–585, 2011.

[27] David Farmer, Qiang Li, and Jae-Hun Park. Internal wave observations in the South China Sea: The role of rotation and non-linearity. *Atmosphere-Ocean*, 47(4):267–280, 2009.

[28] V. N. Galkin and Yu. A. Stepanyants. On the existence of stationary solitary waves in a rotating fluid. *J. Appl. Maths. Mech.*, 55:939–943, 1991.

[29] Clifford S. Gardner, John M. Greene, Martin D. Kruskal, and Robert M. Miura. Method for solving the korteweg-devries equation. *Physical Review Letters*, 19 (19):1095–1097, 1967.

[30] John Anthony Gear and Roger Grimshaw. Weak and strong interactions between internal solitary waves. *Studies in Applied Mathematics*, 70(3):235–258, 1984.

[31] R. Grimshaw and K.R. Helfrich. The effect of rotation on internal solitary waves. *IMA J. Appl. Math.*, 77:326–339, 2012.

[32] R. Grimshaw and C. Yuan. The propagation of internal undular bores over variable topography. *Physica D: Nonlinear Phenomena*, 333:200–207, 2016.

[33] R.H.J. Grimshaw, J-M. He, and L.A. Ostrovsky. Terminal damping of a solitary wave due to radiation in rotational systems. *Stud. Appl. Math.*, 101:197–210, 1998.

[34] Roger Grimshaw. Evolution equations for long, nonlinear internal waves in stratified shear flows. *Studies in Applied Mathematics*, 65(2):159–188, 1981.

[35] Roger Grimshaw. Evolution equations for weakly nonlinear long internal waves in a rotating fluid. *Studies in Applied Mathematics*, 73(1):1–33, 1985.

[36] Roger Grimshaw. *Environmental stratified flows*. Number 3. Springer Science & Business Media, 2002.

[37] Roger Grimshaw. Internal solitary waves in a variable medium. *GAMM-Mitteilungen*, 30(1):96–109, 2006.

[38] Roger Grimshaw. Coupled Korteweg–de Vries Equations. In *Without Bounds: A Scientific Canvas of Nonlinearity and Complex Dynamics*, pages 317–333. Springer, 2013.

[39] Roger Grimshaw and Karl Helfrich. Long-time solutions of the Ostrovsky equation. *Studies in Applied Mathematics*, 121:71–88, 2008.

[40] Roger Grimshaw, Efim Pelinovsky, and Oxana Poloukhina. Higher-order Korteweg-de Vries models for internal solitary waves in a stratified shear flow with a free surface. *Nonlinear Processes in Geophysics*, 9:221–235, 2002.

[41] Roger Grimshaw, Efim Pelinovsky, and Tatiana Talipova. Damping of large-amplitude solitary waves. *Wave motion*, 37(4):351–364, 2003.

[42] Roger Grimshaw, Efim Pelinovsky, and Tatiana Talipova. Modelling internal solitary waves in the coastal ocean. *Surveys in Geophysics*, 28(4):273–298, 2007.

[43] Roger Grimshaw, E. Pelinovsky, T. Talipova, and Oxana Kurkina. Internal solitary waves: propagation, deformation and disintegration. *Nonlinear Processes in Geophysics*, 17(6):633–649, 2010.

[44] Roger Grimshaw, Chuncheng Guo, Karl Helfrich, and Vasiliy Vlasenko. Com-

bined effect of rotation and topography on shoaling oceanic internal solitary waves. *Journal of Physical Oceanography*, 44(4):1116–1132, 2014.

[45] Roger Grimshaw, Yury Stepanyants, and Azwani Alias. Formation of wave packets in the Ostrovsky equation for both normal and anomalous dispersion. *Proc. R. Soc. A*, 472:20150416, 2016.

[46] Roger H. J. Grimshaw, Karl R. Helfrich, and Edward R. Johnson. Experimental study of the effect of rotation on nonlinear internal waves. *Physics of Fluids*, 25(5):056602, 2013.

[47] C. Guo and X. Chen. Numerical investigation of large amplitude second mode internal solitary waves over a slope-shelf topography. *Ocean Modelling*, 42: 80–91, 2012.

[48] C. Guo and X. Chen. A review of internal solitary wave dynamics in the northern South China Sea. *Progress in Oceanography*, 121:7–23, 2014.

[49] Pu Guo, Wendong Fang, Zijun Gan, Rongyu Chen, and Xiaomin Long. Internal tide characteristics over northern South China Sea continental slope. *Chinese Science Bulletin*, 51:17–25, 2006.

[50] A. V. Gurevich and L. P. Pitayevsky. Nonstationary structure of a collisionless shock wave. *Soviet Journal of Experimental and Theoretical Physics*, 38:590–604, 1974.

[51] Karl R. Helfrich. Decay and return of internal solitary waves with rotation. *Physics of Fluids*, 19(2):026601, 2007.

[52] Karl R. Helfrich and W. Kendall Melville. Long nonlinear internal waves. *Annu. Rev. Fluid Mech.*, 38:395–425, 2006.

[53] Peter E. Holloway, Efim Pelinovsky, Tatyana Talipova, and Belinda Barnes. A nonlinear model of internal tide transformation on the Australian North West Shelf. *Journal of Physical Oceanography*, 27(6):871–896, 1997.

[54] Ming-Kuang Hsu, Antony K. Liu, and Cheng Liu. A study of internal waves in the China Seas and Yellow Sea using SAR. *Continental Shelf Research*, 20 (4):389–410, 2000.

[55] Xiaodong Huang, Zhaohui Chen, Wei Zhao, Zhiwei Zhang, Chun Zhou, Qingxuan Yang, and Jiwei Tian. An extreme internal solitary wave event observed in the northern South China Sea. *Scientific reports*, 6:30041, 2016.

[56] C. R. Jackson. An atlas of internal solitary-like waves and their properties, 2nd ed. Technical report, Global Ocean Assoc., Alexandria, Va. (Available at http://www.internalwaveatlas.com), 2004.

[57] Sen Jan, Ren-Chieh Lien, and Chi-Hua Ting. Numerical study of baroclinic tides in Luzon Strait. *Journal of Oceanography*, 64(5):789–802, 2008.

[58] R. I. Joseph. Solitary waves in a finite depth fluid. *Journal of Physics A: Mathematical and General*, 10(12):L225, 1977.

[59] B. B. Kadomtsev and V. I. Petviashvili. On the stability of solitary waves in weakly dispersing media. In *Sov. Phys. Dokl*, volume 15, pages 539–541, 1970.

[60] A. M. Kamchatnov. *Nonlinear Periodic Waves and Their Modulations: An Introductory Course*. World Scientific, 2000. ISBN 9789810244071.

[61] A. M. Kamchatnov, Y.-H. Kuo, T.-C. Lin, T.-L. Horng, S.-C. Gou, Richard Clift, G. A. El, and Roger H. J. Grimshaw. Undular bore theory for the Gardner equation. *Physical Review E*, 86(3):036605, 2012.

[62] A. M. Kamchatnov, Y.-H. Kuo, T.-C. Lin, T.-L. Horng, S.-C. Gou, Richard Clift, G. A. El, and Roger H. J. Grimshaw. Transcritical flow of a stratified fluid over topography: analysis of the forced Gardner equation. *Journal of Fluid Mechanics*, 736:495–531, 2013.

[63] Chiu-Yen Kao and Yuji Kodama. Numerical study of the KP equation for non-periodic waves. *Mathematics and Computers in Simulation*, 82(7):1185–1218, 2012.

[64] Yuji Kodama. KP solitons in shallow water. *Journal of Physics A: Mathematical and Theoretical*, 43(43):434004, 2010.

[65] Yuji Kodama, Masayuki Oikawa, and Hidekazu Tsuji. Soliton solutions of the KP equation with V-shape initial waves. *Journal of Physics A: Mathematical and Theoretical*, 42(31):312001, 2009.

[66] C. Gary Koop and Gerald Butler. An investigation of internal solitary waves in a two-fluid system. *Journal of Fluid Mechanics*, 112:225–251, 1981.

[67] D. J. Korteweg and G. de Vries. On the change of form of long waves advancing in a rectangular channel, and a new type of long stationary wave. *Phil. Mag.*, 39:422–443, 1895.

[68] T. Kubota, D. R. S. Ko, and L. D. Dobbs. Weakly-nonlinear, long internal gravity waves in stratified fluids of finite depth. *J. Hydronautics*, 12(5):157–157, 1978.

[69] Kevin G. Lamb. Energy and pseudoenergy flux in the internal wave field generated by tidal flow over topography. *Continental shelf research*, 27(9): 1208–1232, 2007.

[70] Chi-Yuan Lee and Robert C. Beardsley. The generation of long nonlinear internal waves in a weakly stratified shear flow. *Journal of Geophysical Research*, 79(3):453–462, 1974.

[71] C. E. Leith. Stochastic models of chaotic systems. *Physica D: Nonlinear Phenomena*, 98(2-4):481–491, 1996.

[72] Antony K. Liu and Ming-kuang Hsu. Internal wave study in the South China Sea using Synthetic Aperture Radar (SAR). *International Journal of Remote Sensing*, 25(7-8):1261–1264, 2004.

[73] Antony K. Liu, Feng-Chun Su, Ming-Kuang Hsu, Nan-Jung Kuo, and Chung-Ru Ho. Generation and evolution of mode-two internal waves in the South China Sea. *Continental Shelf Research*, 59:18–27, 2013.

[74] Robert R. Long. Some aspects of the flow of stratified fluids. *Tellus*, 7(3): 341–357, 1955.

[75] Michael S. Longuet-Higgins. On the mass, momentum, energy and circulation of a solitary wave. In *Proceedings of the Royal Society of London A: Mathematical, Physical and Engineering Sciences*, volume 337, pages 1–13. The Royal Society, 1974.

[76] Michael S. Longuet-Higgins and J. D. Fenton. On the mass, momentum, energy and circulation of a solitary wave. II. In *Proceedings of the Royal Society of London A: Mathematical, Physical and Engineering Sciences*, volume 340, pages 471–493. The Royal Society, 1974.

[77] John Marshall, Alistair Adcroft, Chris Hill, Lev Perelman, and Curt Heisey. A finite-volume, incompressible Navier Stokes model for studies of the ocean on parallel computers. *Journal of Geophysical Research: Oceans*, 102(C3): 5753–5766, 1997.

[78] John Marshall, Chris Hill, Lev Perelman, and Alistair Adcroft. Hydrostatic, quasi-hydrostatic, and nonhydrostatic ocean modeling. *Journal of Geophysical Research: Oceans*, 102(C3):5733–5752, 1997.

[79] John W. Miles. Obliquely interacting solitary waves. *Journal of Fluid Mechanics*, 79(1):157–169, 1977.

[80] John W. Miles. Resonantly interacting solitary waves. *Journal of Fluid Mechanics*, 79(1):171–179, 1977.

[81] Paul A. Milewski and Joseph B. Keller. Three-dimensional water waves. *Studies in Applied Mathematics*, 97(2):149–166, 1996.

[82] Motoyasu Miyata. An internal solitary wave of large amplitude. *La mer*, 23 (2):43–48, 1985.

[83] Motoyasu Miyata. Long internal waves of large amplitude. In *Proceedings of the IUTAM Symposium on Nonlinear Water Waves*, pages 399–406, 1988.

[84] Hiroaki Ono. Algebraic solitary waves in stratified fluids. *Journal of the Physical Society of Japan*, 39(4):1082–1091, 1975.

[85] A. R. Osborne and T. L. Burch. Internal solitons in the Andaman Sea. *Science*, 208(4443):451–460, 1980.

[86] A. R. Osborne, T. L. Burch, and R. I. Scarlet. The influence of internal waves on deep-water drilling. *Journal of Petroleum Technology*, 30(10):1497–1504, 1978.

[87] L. A. Ostrovsky. Nonlinear internal waves in a rotating ocean. *Oceanology*, 18 (2):119–125, 1978.

[88] L. A. Ostrovsky and Yu A. Stepanyants. Internal solitons in laboratory experiments: Comparison with theoretical models. *Chaos: An Interdisciplinary Journal of Nonlinear Science*, 15(3):037111, 2005.

[89] Lev A. Ostrovsky and John Grue. Evolution equations for strongly nonlinear internal waves. *Physics of Fluids*, 15(10):2934–2948, 2003.

[90] Richard B. Perry and Gerald R. Schimke. Large-amplitude internal waves observed off the northwest coast of Sumatra. *Journal of Geophysical Research*, 70(10):2319–2324, 1965.

[91] Steven R. Ramp, Tswen Yung Tang, Timothy F. Duda, James F. Lynch, Antony K. Liu, Ching-Sang Chiu, Hyoung-Rok Bahr, Frederick L .and Kim, and Y. J. Yang. Internal solitons in the northeastern South China Sea. Part I: Sources and deep water propagation. *IEEE Journal of Oceanic Engineering*, 29(4):1157–1181, 2004.

[92] Richard D. Ray and Gary T. Mitchum. Surface manifestation of internal tides generated near Hawaii. *Geophysical Research Letters*, 23(16):2101–2104, 1996.

[93] Lord Rayleigh. On waves. *Phil. Mag.*, 1:257–259, 1876.

[94] J. S. Russell. Report of the 14th meeting of the British Association for the Advancement of Science, 1845.

[95] Philipp Schlatter, N. A. Adams, and L. Kleiser. A windowing method for periodic inflow/outflow boundary treatment of non-periodic flows. *Journal of computational physics*, 206(2):505–535, 2005.

[96] Kenji Shimizu and Keisuke Nakayama. Effects of topography and Earth's rotation on the oblique interaction of internal solitary-like waves in the Andaman Sea. *Journal of Geophysical Research: Oceans*, 122:7449–7465, 2017.

[97] James N. Shroyer, Emily L .and Moum and Jonathan D. Nash. Mode 2 waves on the continental shelf: Ephemeral components of the nonlinear internal wavefield. *Journal of Geophysical Research: Oceans*, 115(C7), 2010.

[98] Harper Simmons, Ming-Huei Chang, Ya-Ting Chang, Shenn-Yu Chao, Oliver Fringer, Christopher R. Jackson, and Dong Shan Ko. Modeling and prediction of internal waves in the South China Sea. *Oceanography*, 24(4):88–99, 2011.

[99] Justin Small, Zack Hallock, Gary Pavey, and John Scott. Observations of large amplitude internal waves at the Malin shelf edge during SESAME 1995. *Continental Shelf Research*, 19(11):1389–1436, 1999.

[100] M. Stastna, F. J. Poulin, K. L. Rowe, and C. Subich. On fully nonlinear, vertically trapped wave packets in a stratified fluid on the f-plane. *Physics of Fluids*, 21(10):106604, 2009.

[101] L. N. Trefethen. *Spectral Methods in MATLAB*. Society for Industrial and Applied Mathematics (SIAM), 2000.

[102] Hidekazu Tsuji and Masayuki Oikawa. Oblique interaction of solitons in an extended Kadomtsev-Petviashvili equation. *Journal of the Physical Society of Japan*, 76(8):084401, 2007.

[103] Ka-Kit Tung, Tony F. Chan, and Toshi Kubota. Large amplitude internal waves of permanent form. *Studies in Applied Mathematics*, 66(1):1–44, 1982.

[104] V. Vlasenko and N. Stashchuk. Three-dimensional shoaling of large-amplitude internal waves. *Journal of Geophysical Research: Oceans*, 112(C11), 2007. C11018.

[105] V. Vlasenko, N. Stashchuk, C. Guo, and X. Chen. Multimodal structure of baroclinic tides in the South China Sea. *Nonlinear Processes in Geophysics*, 17(5):529 – 543, 2010.

[106] C. Wang and R. Pawlowicz. Propagation speeds of strongly nonlinear near-surface internal waves in the Strait of Georgia. *Journal of Geophysical Research: Oceans*, 116(C10), 2011.

[107] C. Wang and R. Pawlowicz. Oblique wave-wave interactions of nonlinear near-surface internal waves in the Strait of Georgia. *Journal of Geophysical Research: Oceans*, 117(C6), 2012.

[108] A. J Whitfield and E. R. Johnson. Whitham modulation theory for the Ostrovsky equation. *Proc. R. Soc. A*, 473:20160709, 2017.

[109] G. B. Whitham. Non-linear dispersive waves. In *Proceedings of the Royal Society of London A: Mathematical, Physical and Engineering Sciences*, volume 283, pages 238–261. The Royal Society, 1965.

[110] G. B. Whitham. *Linear and nonlinear waves*. John Wiley & Sons, 1974.

[111] Jingshuang Xue, Hans C. Graber, Roland Romeiser, and Bjorn Lund. Understanding internal wave–wave interaction patterns observed in satellite images of the Mid-Atlantic Bight. *IEEE Transactions on Geoscience and Remote Sensing*, 52(6):3211–3219, 2014.

[112] Y. J. Yang, Y. C. Fang, T. Y. Tang, and S. R. Ramp. Convex and concave types of second baroclinic mode internal solitary waves. *Nonlinear Processes in Geophysics*, 17(6):605–614, 2010.

[113] Yiing Jang Yang, Ying Chih Fang, Ming-Huei Chang, Steven R. Ramp, Chih-Chung Kao, and Tswen Yung Tang. Observations of second baroclinic mode internal solitary waves on the continental slope of the northern South China Sea. *Journal of Geophysical Research: Oceans*, 114(C10), 2009.

[114] Harry Yeh and Wenwen Li. Laboratory realization of KP-solitons. *Journal of Physics: Conference Series*, 482(1):012046, 2014.

[115] Harry Yeh, Wenwen Li, and Yuji Kodama. Mach reflection and KP solitons in shallow water. *Eur. Physical J., Special Topics*, 185:97–111, 2010.

[116] C. Yuan, R. Grimshaw, and E. Johnson. The evolution of second mode internal solitary waves over variable topography. *Journal of Fluid Mechanics*, 836:238–259, 2018.

[117] Chunxin Yuan, Roger Grimshaw, and Edward Johnson. The evolution of internal undular bores over a slope in the presence of rotation. *Studies in Applied Mathematics*, 2018.

[118] Chunxin Yuan, Roger Grimshaw, Edward Johnson, and Xueen Chen. The propagation of internal solitary waves over variable topography in a horizontally two-dimensional framework. *Journal of Physical Oceanography*, 48:283–300, 2018.

[119] Norman J. Zabusky and Martin D. Kruskal. Interaction of 'solitons' in a collisionless plasma and the recurrence of initial states. *Physical review letters*, 15(6):240–243, 1965.

[120] V. Zakharov and A. Shabat. Exact theory of two-dimensional self-focusing and one-dimensional self-modulation of waves in nonlinear media. *Soviet physics JETP*, 34(1):62, 1972.

[121] Z. Zhang, O. B. Fringer, and S. R. Ramp. Three-dimensional, nonhydrostatic numerical simulation of nonlinear internal wave generation and propagation in the South China Sea. *Journal of Geophysical Research: Oceans*, 116(C5), 2011. C05022.

[122] Zhongxiang Zhao, Victor Klemas, Quanan Zheng, and Xiao-Hai Yan. Remote sensing evidence for baroclinic tide origin of internal solitary waves in the northeastern South China Sea. *Geophysical Research Letters*, 31(6), 2004.

[123] Q. Zheng, V. Klemas, X.-H. Yan, Z. Wang, and K. Kagleder. Digital orthorectification of space shuttle coastal ocean photographs. *International Journal of Remote Sensing*, 18(1):197–211, 1997.

[124] Xianchi Zhou and Roger Grimshaw. The effect of variable currents on internal solitary waves. *Dynamics of Atmospheres and Oceans*, 14:17–39, 1989.

[125] J. Ziegenbein. Short internal waves in the Strait of Gibraltar. *Deep Sea Research and Oceanographic Abstracts*, 16(5):479 – 487, 1969.

[126] J. Ziegenbein. Spatial observations of short internal waves in the Strait of Gibraltar. In *Deep Sea Research and Oceanographic Abstracts*, volume 17, pages 867–875, 1970.